Solitons in Nonlocal Media

Alessandro Alberucci

Tutor:

Prof. Gaetano Assanto

Coordinator:

Prof. Gennaro Conte

Department of Electronic Engineering

University Roma Tre

A thesis submitted for the degree of

PhilosophiæDoctor (PhD)

2008

Abstract

Optical communications are fundamental in our society based upon information, allowing the sharing of large amounts of data all around the world. A great deal of attention has been devoted to all-optical methods for information processing, as they could improve the available technology. In this context nonlinear optics is a key tool to reach such goal. A lot of attention from the scientific community has been paid to spatial solitons, i.e. shape-preserving nonlinear waves, for their ability to guide signals. In particular, an important role is played by solitons in nonlocal media, because in these materials a soliton can be employed as a waveguide for signals even at longer wavelength, paving the way to the design of reconfigurable communication networks via all-optical methods. Nonlocality also mediates the interaction between spatially separated beams, making new applications feasible. In this thesis I focus on highly nonlocal media, in particular on the nematic liquid crystals (NLC), with a high value and non-resonant behavior of their nonlinearity, allowing solitons formation at a few mW and in a large range of wavelengths. The outline of this thesis is as follows. In the first chapter I briefly introduce spatial solitons and reorientational nonlinearity in NLC. In the second chapter I show experimental and theoretical investigation on single soliton propagation in NLC. In the third chapter I discuss, theoretically and numerically, the interplay between nonlocality and nonlinearity in finite-size samples and their effect on beam trajectory, comparing the results with experiments performed in NLC. In chapter 4 I investigate solitons composed by two beams of different wavelengths. Finally, in chapter 5 I discuss light amplification and solitons in dye-doped NLC.

The results of this thesis enlighten a large number of new approaches for the optical signal processing which can be implemented in nonlocal media, and in particular the main role played by NLC and solitons in this context.

To everybody who has supported me all along this adventure.

Acknowledgements

First, I would like to thank Prof. Gaetano Assanto who gave me the possibility to join into his research group Nooel (Nonlinear Optics and OptoElectronics Lab), a unique opportunity in Italy. He taught (and keeps teaching) me how to make good research and supervised all my work during my PhD course, guiding me towards important goals and providing me with a lot of precious advices. I would like to thank Dr. Marco Peccianti: we closely collaborated during the three years of my PhD; he performed the experiments I address in this thesis in chapters 3 and 4. He taught me experimental techniques and several aspects of liquid crystals, making himself always available for fruitful discussions. Special thanks to Claudio Conti, Andrea Fratalocchi, Alessia Pasquazi and Armando Piccardi, who helped me in various stages in the study of liquid crystals. I would like to thank Dr. Malgosia Kaczmarek and Dr. Andriy Dyadusha from the School of Physics and Astronomy in Southampton and Prof. Cesare Umeton, Antonio De Luca and Giuseppe Coschigano from University of Calabria for providing samples of high quality, essential to carry out good experiments. I also thank the other people who worked in the Nooel throughout the years, both for their friendship and their scientific support; in rigorous alphabetic order Emiliano Alberici, Armando Altieri, Michele Balbi, Mattia Cichocki, Stefano Cozza, Lorenzo Colace, Andrea Del Monte, Andrea Di Falco, Pasquale Ferrara, Giuseppe Leo, GianLorenzo Masini, Valeria Mazzoni, Andrea Natale, Francesco Petullà, Marco Ravaro, Alessio Rocchetti, Usman Sapaev, Vito Sorianello and Salvatore Stivala. I would like to thank all my (other) friends: without their help and support reaching this goal would have been much hard. Thanks to all of you guys. Last, but not least, I would like to thank my family, who provided me all the assistance I needed to complete this important stage of my education.

Contents

List of Figures

1

Introduction

1.1 Solitons in Nonlinear Physics

Nonlinearity has an important role in many disciplines such as physics, economics, chemistry, biology and so on. In fact, most natural phenomena are intrinsically nonlinear, being linear only when small excitations are considered. Up to the twentieth century, scientists focused on linear phenomena, firstly because of the large availability of analytical solutions and secondly, but not less important, because of the possibility to use superimposition principle, which provides the complete knowledge of a system after studying its response to limited sets of excitations. This principle is largely adopted in engineering and physics, for example in harmonic analysis. Einstein's general relativity, one of the most successful physical theories in 1900's, is based on nonlinear equations. With the advent of modern computers in the 50's, the available computation power allowed to study nonlinear problems numerically: among pioneering work I remind the Fermi, Pasta and Ulam paper concerning energy distribution in a nonlinear vibrating string (1; 2) and the Lorenz article about chaos in meteorology (3).

One of the most striking features of nonlinear systems is the formation of waves with an invariant profile along their propagation due to the interplay between linear and nonlinear effects, called solitons. Strictly speaking, solitons are solutions of integrable models[1], which can be solved by the inverse scattering technique (4). In non integrable models, shape-preserving solutions are called *solitary waves* but, as usual in the spe-

[1]In this context integrability means that the differential equations composing the model encompass an infinite set of conserved quantities.

cialized literature (5; 6), I don't make any distinction in this thesis and I will use hereby the term soliton even in the presence of non integrable equations.

The first experimental observation of a soliton was carried out by J.S. Russell in 1834 (7): he observed a shape-invariant wave in a shallow water canal in Scotland, noting also its stability with respect to perturbing factors. This phenomenon remained unexplained until 1895, when the two Dutch mathematicians Korteweg and De Vries provided a theoretical basis by developing an equation (8), now called after them the Korteweg-De Vries (KdV) equation. Ever since, solitons have attracted a lot of attention given their particle-like behavior and their intrinsic nature of *modes* of nonlinear systems. Solitons have been investigated, both experimentally and theoretically, in several branches of physics, including plasma (9; 10), Bose-Einstein Condensate (BEC) (11), solid-state (12) and general relativity (13). Solitons are also studied in electronic oscillators (14).

1.2 Optical Solitons

In optics nonlinear media exhibit an optical response which depends nonlinearly on field strength (15). More specifically, the dipole moment per unit volume is given by $\mathbf{P} = f(\mathbf{E})$, where $\mathbf{E}$ is the electric field and f is a nonlinear function dependent on the material[1]. Nonlinear effects in optics have become accessible after the invention of laser by Mainman in 1960 (16), who made available light intensities strong enough to excite a nonlinear behavior. The first experimental demonstration of nonlinear phenomena in optics was the second harmonic generation by Franken et al. in 1961 (17). Ever since, many different kinds of nonlinearities have been discovered. The simplest nonlinearity is the Kerr one, which entails a nonlinear polarization $\mathbf{P}_{NL}$ given by $\mathbf{P}_{NL} = \chi^{(3)}\mathbf{E}^3$ in isotropic media. Using the latter in the electric field ruling equations, I get a nonlinear change in index Δn given by $\Delta n = n_2 I$, being I the beam intensity and n_2 the Kerr coefficient (15). Therefore, propagating fields modulate their own phase: for spatially finite beams propagating in homogeneous media, if $n_2 > 0 (< 0)$ I have a self-focusing (defocusing) effect (18; 19); for finite pulses propagating in guides (for example fibers) I have a nonlinear chirp in the frequency (20).

Solitons in optics can be divided into two main classes: temporal and spatial solitons

[1]Linear media are featured by the relationship $\mathbf{P} = \chi^{(1)}\mathbf{E}$, with $\chi^{(1)}$ a constant susceptibility

(6), according to the propagation coordinate taken into account[1]. Moreover, a soliton can be a bright spot in a dark background or a light dip in a uniform background; beams of the former kind are named bright solitons, those of second are dark solitons (21).

Optical temporal solitons are pulses which maintain their shape in time in nonlinear guides owing to the balance between broadening, due to the unavoidable dispersion, and nonlinear self-phase modulation. They have been extensively investigated owing to their possible applications in fiber optics, in order to improve the bit-rate (22).

Conversely, spatial solitons are nonlinear waves stationary with respect to time; they do not change their spatial profile as they propagate (5; 23; 24). As it is well known, in linear homogeneous media electromagnetic waves diffract, i.e. their transverse width increases along propagation. In some nonlinear media, as I discussed above referring to the Kerr effect, beams are capable (for large enough input powers) to self-focus, i.e. to form a lens. When this two counter-acting effects are perfectly balanced, a soliton is formed. Because of this formation mechanism, soliton shape and power are strongly dependent on the specific nonlinearity. For example, in Kerr media only solitons in (1+1)D[2], i.e. in slab nonlinear waveguides, are stable; in (2+1)D they are unstable, i.e. solitons are destroyed by beam collapse. To obtain stable solitary propagation in (2+1)D it is necessary to exploit some other kind of nonlinearities, for example saturable or nonlocal ones (6).

Finally, solitons with profiles containing more than a local maximum, known as higher order solitons in analogy with higher-order modes of linear guides, have been demonstrated as well (5).

In this thesis I will focus on bright spatial solitons.

1.3 Nonlocality

Generally speaking, a medium is nonlocal when its response to an excitation is not null even in points where the excitation is zero, i.e. the Green function has a finite

[1]Actually, there is a third kind of soliton called bullet, nonlinearly self-localized in both space and time.

[2]In this notation the first and second number are the transverse and propagation coordinates, respectively.

width[1]. Nonlocality plays an important role in many areas of nonlinear physics, including plasma physics (25), BEC (26; 27), fluid mechanics (28) and optics (29; 30). A spatial nonlocal response can deeply affect the propagation of nonlinear waves, e.g. stabilizing two-dimensional self-guided beams (30; 31; 32), or even more complicated structures (33; 34; 35; 36; 37). The nature and extent of nonlocality substantially depend on materials; in optics I remember thermo-optic media (38; 39; 40), photorefractives (41; 42), soft-matter (43), semiconductor amplifier (44), atomic or molecules diffusion in vapors (45) and liquid crystals (46; 47).
In dielectric nonlinear optics, in general the excitation is the electric field and the response is the nonlinear polarization $\mathbf{P}_{NL}$. Although there are media where the interaction is coherent, i.e. it depends on phase [$\chi^{(2)}$ crystals for example (15; 48)], this thesis will deal with nonlinearities dependent on intensity. More specifically, I will consider the equation governing field propagation in the harmonic regime in isotropic non magnetic[2] media

$$\nabla^2\mathbf{E} + k_0^2 n^2(\mathbf{r}, I)\mathbf{E} = 0 \tag{1.1}$$

where the index profile depends on the spatial coordinates (non homogeneous material) and on the intensity. Considering a linear polarization for $\mathbf{E}$ and, therefore, setting $\mathbf{E} = Ae^{ik_0n_0s}\hat{\boldsymbol{e}}$, with s the propagation coordinate, $k_0 = 2\pi/\lambda$ with λ the vacuum wavelength and n_0 the linear index, by applying the SVEA (Slowly Varying Envelope Approximation)[3], i.e. in the paraxial approximation (15), I get:

$$2ik_0n_0\frac{\partial A}{\partial s} + \nabla_\perp^2 A + k_0^2\left(n^2 - n_0^2\right)A = 0 \tag{1.2}$$

where $\nabla_\perp^2$ is the transverse Laplacian. I note how eq. (1.2) is analogous to a Schröedinger equation (49) with a potential depending on the intensity.
Considering the nonlinear terms as perturbative with respect to the linear ones, I set $\left(n^2 - n_0^2\right) \cong 2n_0\Delta n(\mathbf{r}, I)$, where I defined $\Delta n(\mathbf{r}, I) = [n(\mathbf{r}, I) - n_0]$. If not explicitly

[1] Such width provides also a measure of the nonlocal degree of the medium.
[2] This means $\mu = \mu_0$.
[3] This corresponds to neglecting the term $\partial^2 A/\partial s^2$.

specified, from here on I will consider homogeneous nonlinear media, i.e. with Δn not explicitly dependent on space[1]. Eq. (1.2) becomes

$$2ik_0 n_0 \frac{\partial A}{\partial s} + \nabla_\perp^2 A + k_0^2 2 n_0 \Delta n(I) A = 0 \tag{1.3}$$

This is the nonlinear Schröedinger equation (NLSE) for a generalized nonlinearity, widely used in modeling spatial solitons. Assuming a linear relationship between the intensity I and the index perturbation Δn (for example, thermo-optic media and liquid crystals in limited range of powers), and supposing that Δn on a certain plane normal to s depends on intensity in that plane,[2] I get

$$\Delta n = \int I(\mathbf{r}'_\perp) G(|\mathbf{r}_\perp - \mathbf{r}'_\perp|) dS' \tag{1.4}$$

where dS' and $\mathbf{r}_\perp$ are the infinitesimal area element and position vector on the transverse plane, respectively, and $G(|\mathbf{r}_\perp - \mathbf{r}'_\perp|)$ is the Green function for the material (32). I introduced a Green function depending only on the distance between excitation and effect, that is, an infinitely extended medium. Finite geometries will be discussed in chapter 3.

A nonlinear material which is described by eqs. (1.3) and (1.4) is *nonlocal Kerr*. In local Kerr media I have $\Delta n = n_2 I$ and eq. (1.3) turns into the classical NLSE, which is integrable and supports the fundamental soliton with a sech profile (6).

Different ranges of nonlocality have been discussed in literature: from high (31; 39; 50; 51; 52; 53; 54) to weak (32; 55).

1.3.1 Strong Nonlocality

Let me begin with the highly nonlocal case and, for the sake of simplicity, explore its features in a one dimensional geometry. Expanding $G(x - x')$ in eq. (1.4) in a Taylor series around the point $x = x'$[3], I get:

[1] I note that the nonlinear index perturbation is varying in space due to its dependence on I.

[2] According to the hypothesis, Δn is governed by $L(\Delta n) = I$ with L a certain linear differential operator; in case of solitary propagation I have that all the s derivatives become null due to the invariance in propagation, hence the index perturbation on a plane normal to s depends only on intensity computed on that plane.

[3] I implicitly assume that the Green function is derivable in $x = x'$; this is not always true, as it will be shown in chapter 3.

$$\Delta n(x) = \int I(x') \left[G|_{x=x'} + \left.\frac{dG}{d(x-x')}\right|_{x=x'} (x-x') + \frac{1}{2} \left.\frac{d^2G}{d(x-x')^2}\right|_{x=x'} (x-x')^2 + \dots \right] dx' =$$
$$= G_0 P + G_2 \int I(x') \left(x-x'\right)^2 dx' + \ldots = P \sum_{m=0}^{\infty} G_{2m} \left\langle \left(x-x'\right)^{2m} \right\rangle_{I(x')} \tag{1.5}$$

being $G_m \equiv \frac{1}{m!} \left.\frac{d^m G}{d(x-x')^m}\right|_{x=x'}$, $\langle f(x) \rangle_{I(x)} = \int I(x) f(x) dx / \int I(x) dx$ and $\int I(x) dx = P$, with P the beam power. Furthermore, I assumed that $\int x I(x) dx = 0$, i.e. the point $x = 0$ is the beam center. In deriving eq. (1.5) I used the relationship $G_{2m+1} = 0$, i.e. I supposed that beam peak and the maximum of the Green function overlap. I underline the linear relationship between Δn and the power P, as expected from the initial hypothesis.

Eq. (1.5) is the power series (in space) of the nonlinear index perturbation Δn. In the highly nonlocal case, i.e. when the beam width is negligible with respect to the extension of the response function, taking an even parity for the intensity I get $\Delta n \cong \left(G_0 + G_2 \left\langle x'^2 \right\rangle_{I(x')} \right) P + G_2 P x^2$ (53), i.e. the index perturbation is parabolic in space, with concavity proportional to power through a material dependent parameter G_2; moreover, $G_2 < 0$ ($G_2 > 0$) in focusing (defocusing) media[1]. Substituting into (1.3), I retrieve the Schröedinger equation for a parabolic potential, i.e. the well known quantum harmonic oscillator (49). In essence, I have transformed the nonlinear problem into a well known linear problem, largely studied in quantum mechanics and in optics; given the simple mathematics needed to describe this family of solitons (as compared, for example, to inverse scattering technique) they were named *accessible solitons* (31).

The eigenfunctions corresponding to solitons are Hermite-Gauss functions[2]. Since the eigenfunction width depends on G_2, which is power-dependent, solitons with a certain width exist only for a value of the power. These solitons are stable, i.e. small perturbations do not destroy their nature in propagation.

Accessible solitons have firstly observed in liquid crystals (30; 47; 51) and, later, in lead-glasses with a thermal nonlinearity (39; 57).

[1] If I consider a Dirac function $I = P\delta(x)$ for the intensity profile I get $\Delta n = PG(x)$ which, expanded around $x = 0$, gives the same result because $\int \delta(x) x^2 dx = 0$.

[2] In cartesian coordinates. Other coordinate systems yield different eigenfunctions; for example, a cylindrical system gives Laguerre-Gauss functions [see (56)].

1.3.2 Weak Nonlocality

In eq. (1.4), expanding the intensity profile I centered in $x = 0$ and with even parity in a power series around $x' = x$, I get

$$\Delta n = \sum_{m=0}^{\infty} I_{2m}(x) \left\langle t^{2m} \right\rangle_G \tag{1.6}$$

where $I_{2m}(x) = \frac{1}{(2m)!} \frac{\partial^{2m} I(x)}{\partial x^{2m}}$ and $\left\langle t^{2m} \right\rangle_G = \int t^{2m} G(t) dt$. In the weakly nonlocal case, i.e. when the intensity is wider than the medium response function G, in eq. (1.6) terms corresponding to $m > 2$ can be neglected, providing $\Delta n = I + I_2 \left\langle t^{2m} \right\rangle_G = I + \frac{1}{2}\partial^2 I / \partial x^2 \left\langle t^{2m} \right\rangle_G$: the self-induced waveguide is smoother, stabilizing the soliton in (2+1)D (32).

1.4 Liquid Crystals

In this thesis, in order to investigate the role of nonlocality in nonlinear optical propagation, I examine liquid crystals. In this section I will remind the physical properties which explain nonlocal nonlinear optical propagation in this kind of media.

1.4.1 Liquid Crystal Phases

Three states of matter are the most diffused in nature: solid, liquid and gas. Some organic compounds named *liquid crystals* show intermediate phases between liquid and solid, featured by specific properties[1].

Liquid crystals are characterized by disorder in at least one direction and some degree of anisotropy; for a particle or a specific pattern in a certain position, the probability to find a similar one depends on direction[2] (58). Given the definition above, liquid crystal phases group in three main families, according to the degree of long range positional order exhibited by the molecules:

- *nematic*: the gravity centers of the molecules are totally disordered, but their orientation is correlated;

[1]A rigorous definition refers to *mesomorphic phases*.

[2]This means that the density-density correlation function is anisotropic with respect to some macroscopic axes.

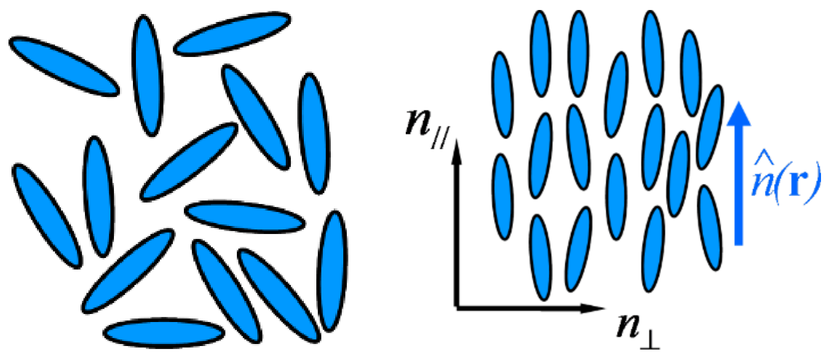

(a) Isotropic phase (b) Nematic phase

Figure 1.1: (a) In the isotropic phase the molecules are positioned without long range order. (b) In nematics the molecules have no positional order, but have an orientational order. The molecular mean axis at each point is expressed by a vectorial field $\hat{\boldsymbol{n}}$ called director.

(a) Dimensions of a 5CB molecule (b) Chemical structure of 5CB

Figure 1.2: Typical dimensions of a 5CB molecule (a) and chemical structure (b).

- *smectics*: the molecules are aligned in a direction and chaotically distributed along the other two;
- *columnar phases*: the molecules are ordered in two dimensions.

Phases and transitions between phases depend on the molecules of the material and on external parameters, such as temperature, chemical composition, voltage, defects and so on.

In this work I focus on the nematic phase. Fig. 1.1 shows a comparison between liquid crystals in isotropic 1.1(a) and nematic phases 1.1(b). In the isotropic phase the material behaves as an isotropic fluid; in the nematic phase the molecules, which do not possess spherical symmetry, acquire orientational order, i.e. their axes point along a common average direction identified by the vector field called *director*. In nematics the direction $\hat{\boldsymbol{n}}$ and $-\hat{\boldsymbol{n}}$ are indistinguishable and, usually, their molecules possess cylindrical symmetry with respect to the director (58). Fig. 1.2 shows a typical nematic molecule along with its chemical structure.

Since, due to thermal agitation, molecules fluctuate around their average direction, it is useful to introduce a single numerical variable -the order parameter S- to quantify such motion (58). Considering a polar reference system with axis z parallel to the director (see fig. 1.3), the molecular directions are statistically described by a distribution function $f(\theta, \phi)$, with $f(\theta, \phi) \sin\theta d\theta d\phi$ the number of molecules with axes aligned into the infinitesimal solid angle given by θ and ϕ. I limit to conventional nematics with cylindrically symmetric molecules: therefore f is independent from ϕ. I define the order parameter S as

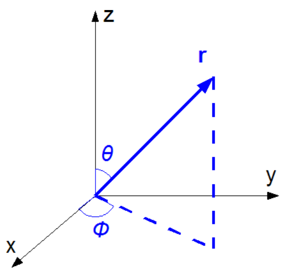

Figure 1.3: Spherical reference system. Axis z is directed as the director $\hat{\boldsymbol{n}}$.

$$S = \int f(\theta) P_2(\cos\theta) d\theta \tag{1.7}$$

being P_2 the second Legendre polynomial. From the definition $S \in [0\ 1]$: $S = 0$ corresponds to full disorder, $S = 1$ to all the molecules parallel to the director $\hat{\boldsymbol{n}}$.

1.4.2 Continuum Theory

The nematic phase can be described by a vectorial field called director. In this section I discuss how to compute $\hat{\boldsymbol{n}}$ knowing the external excitation and the boundary. I am only interested in the stationary regime[1] (see section 1.3).

The continuum theory is developed on a macroscopic scale, based upon director, and gives up a detailed microscopic description of interaction between molecules (58). The approach consists in finding the free energy density F for a specific situation and to minimize its volume integral computed all over the sample, finding the equilibrium distribution for $\hat{\boldsymbol{n}}$. Limiting to electric fields as possible excitations[2], I have $F = F_d + F_E$, where $F_d = \frac{1}{2}\left\{K_1(\nabla\cdot\hat{\boldsymbol{n}})^2 + K_2(\hat{\boldsymbol{n}}\cdot\nabla\times\hat{\boldsymbol{n}})^2 + K_3\left[\hat{\boldsymbol{n}}\times(\nabla\times\hat{\boldsymbol{n}})\right]^2\right\}$ is the distortion energy coming from short-range forces between the molecules, $F_E = -\frac{\epsilon_a}{2}\left(\hat{\boldsymbol{n}}\cdot\mathbf{E}\right)^2$ is the

[1] Typical NLC reorientational response time is milliseconds (58), so at optical frequency the director responds to the average field. This issue will be discussed in more details in sec. 1.4.4.

[2] In this work the excitations are exclusively electric fields, either low, or optical frequencies.

interaction energy with an external electric field **E** due to the medium polarizability (ϵ_a is the dielectric anisotropy), K_i $(i = 1, 2, 3)$ are the (three) Frank elastic constants, associated with splay, twist and bend, respectively (58).
From the minimization of energy I find the Euler-Lagrange equations:

$$\frac{\partial F}{\partial q^j} - \sum_{i=1}^{3} \frac{d}{dx_i} \left(\frac{\partial F}{\partial \frac{dq^j}{dx_i}} \right) = 0 \ (j = 1, 2) \tag{1.8}$$

where $x_1 = x$, $x_2 = y$ and $x_3 = z$ and q^j are two generic angular coordinates which describes the director orientation in the laboratory frame. I assume *hard boundary conditions*, i.e. fixed director values at the edges (59).
The director orientation close to the external walls, i.e. its boundary conditions, can be controlled by treating the surfaces which confine liquid crystals. There are two main possible alignments: *homeotropic*, with director normal to the surface edge, or planar, with molecules parallel to the interfaces (59).

1.4.3 Linear Optical Properties

Macroscopically, nematic liquid crystals (NLC) behave as positive uniaxial crystals with optic axis parallel to the director. The dielectric tensor is given by (60)

$$\epsilon_{ij} = \epsilon_\perp \delta_{ij} + \epsilon_a n_i n_j \tag{1.9}$$

with n_i the director component along the i-th direction, δ_{ij} the Kronecker's delta, $\epsilon_\perp$ and $\epsilon_\parallel$ the dielectric constants perpendicular and parallel to $\hat{\boldsymbol{n}}$, respectively, and $\epsilon_a = \epsilon_\parallel - \epsilon_\perp$ the dielectric anisotropy. Both $\epsilon_\parallel$ and $\epsilon_\perp$ depend on the order parameter S previously defined.
In a homogeneous uniaxial medium, given a certain direction for the wavevector **k**, there are two independent plane eigenwaves: ordinary and extraordinary (61). Ordinary propagation resembles isotropic media with a refractive index $\sqrt{\epsilon_\perp}$. The electric field of the extraordinary wave, conversely, is not parallel to the corresponding displacement field, which implies a Poynting vector **S** non parallel to **k**: in particular, **S** lies in the plane containing the optic axis and **k**, forming with the latter the *walk-off* angle

$\delta = \arctan\left[\frac{\epsilon_a \sin(2\theta)}{\epsilon_a+2\epsilon_\perp+\epsilon_a\cos(2\theta)}\right]$, being θ the angle between $\mathbf{k}$ and $\hat{\boldsymbol{n}}$.[1] The refractive index for the extraordinary plane wave is

$$n_e = \sqrt{\left[\frac{\cos^2\theta}{\epsilon_\perp} + \frac{\sin^2\theta}{\epsilon_\parallel}\right]^{-1}} \tag{1.10}$$

Remarkably, while linear optical propagation in NLC is generally involved due to the lack of homogeneity, in most practical cases a description in terms of ordinary and extraordinary waves holds valid. I will deepen this point in the next chapters.

Another important optical feature of NLC (which allows the experimental observation of optical propagation inside the NLC, as shown later) is their strong Rayleigh scattering[2] (58): in the visible range, light scattered by nematics is larger by a factor 10^6 than in isotropic fluids. In fact in NLC scattering is due to random variations in the dielectric tensor $\boldsymbol{\epsilon}$, caused by fluctuations in density, temperature, etc., or in orientation of $\hat{\boldsymbol{n}}$ (due to thermal agitation). The latter is the dominant effect in the nematic phase, being absent in isotropic fluids.

Let me consider a plane wave with wavevector $\mathbf{k}_{in}$. The light scattered around the solid angle $d\Omega$, centered around the direction of the output wavevector $\mathbf{k}_{out}$, can be evaluated through the scattering differential cross section $d\sigma/d\Omega$ (58)

$$\frac{d\sigma}{d\Omega} = \left(\frac{\epsilon_a k_0^2}{4\pi}\right)\langle|n_\eta(\mathbf{q})|^2\rangle \sum_{\mu=1,2}\left[\left(\hat{\boldsymbol{i}}\cdot\hat{\boldsymbol{a}}_\mu\right)\left(\hat{\boldsymbol{f}}\cdot\hat{\boldsymbol{n}}\right)+\left(\hat{\boldsymbol{i}}\cdot\hat{\boldsymbol{n}}\right)\left(\hat{\boldsymbol{f}}\cdot\hat{\boldsymbol{a}}_\mu\right)\right]^2 \tag{1.11}$$

where $k_0 = 2\pi/\lambda$ is the wavenumber in vacuum, $\mathbf{q}$ is the scattering vector defined by $\mathbf{k}_{out} = \mathbf{k}_{in} + \mathbf{q}$ and I took a single value for all NLC elastic constants; $\hat{\boldsymbol{i}}$ and $\hat{\boldsymbol{f}}$ are two unit vectors parallel to input and scattered fields, respectively; $\hat{\boldsymbol{a}}_1$ and $\hat{\boldsymbol{a}}_2$ are directions which diagonalize the NLC free energy for a fixed $\mathbf{q}$ (58), $\langle\rangle$ stands for thermal average and $|n_\eta(\mathbf{q})|^2$ is the director component due to molecular fluctuations, with η any direction in the plane of $\hat{\boldsymbol{a}}_1$ and $\hat{\boldsymbol{a}}_2$.

From (1.11) it is possible to deduce that scattering is strong for crossed polarizations, i.e., when incident and scattered field are orthogonal to each other, and is particularly strong for low $\mathbf{q}$. Moreover, given that $|n_\eta(\mathbf{q})|^2 \propto \mathbf{q}^{-2}$ and being $|\mathbf{q}| \propto k_0$, the scattered power in NLC shows a trend with the inverse square of incident wavelength (60).

[1] Moreover, $\mathbf{S}$ lies between the optical axis and the wavevector $\mathbf{k}$ in positive uniaxials.

[2] Rayleigh scattering implies no energy exchange between the electromagnetic field and the material, i.e. photons are elastically scattered.

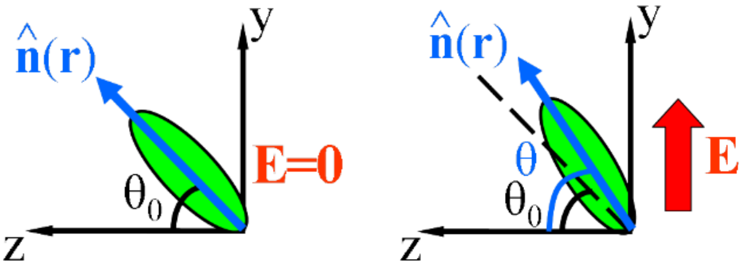

(a) $\mathbf{E} = 0$ (b) $\mathbf{E} \neq 0$

Figure 1.4: (a) In absence of external electric fields the director lies on the plane yz, forming an angle θ_0 with $\hat{\boldsymbol{z}}$. (b) When an electric field is applied parallel to $\hat{\boldsymbol{y}}$, a dipole is induced in the molecules, which rotates towards the electric field in order to minimize their energy. The equilibrium angle θ is reached when the total torque acting on molecules becomes null. I note how rotations take place in a plane defined by the excitation geometry.

1.4.4 Reorientational Nonlinearity

In section 1.4.2 I showed that the interaction energy between the electric field and the NLC is $F_E = -\frac{\epsilon_a}{2}(\hat{\boldsymbol{n}} \cdot \mathbf{E})^2$. This term, inserted into eq. (1.8), gives a torque Γ_E acting on the molecules and equal to $\Gamma_E = 2\mathbf{D} \times \mathbf{E}$, being $\mathbf{D}$ the electric field displacement[1]. Physically, when an external electric field is applied to the NLC, every molecule (excluding those normal to the field) becomes an induced dipole parallel to the long axis. The torque between $\mathbf{E}$ and the induced dipoles tends to rotate the molecules until they are parallel to $\mathbf{E}$ (see figure 1.4). The equilibrium position for $\hat{\boldsymbol{n}}$ corresponds to Γ_E perfectly counterbalanced by the interaction forces between molecules, stemming from F_d (58). When $\mathbf{E}$ and $\hat{\boldsymbol{n}}$ are perpendicular to each other, no reorientation takes place below a threshold in the field: this value is called Freedericskz threshold (58).

Let me now discuss the case of $\mathcal{E}(t)$ varying in time at frequencies larger than the cut-off for a reorientational NLC response. In this case, assuming monochromatic fields [i.e. $\mathcal{E} = \mathbf{E}\sin(\omega t)$], the torque induced by $\mathcal{E}$ is the temporal average of its instantaneous value, $\Gamma_E = 2\left\langle \mathcal{D} \times \mathcal{E} \right\rangle_t = \mathbf{D} \times \mathbf{E}$, with $\left\langle \right\rangle_t$ indicating the temporal average. Although $\mathcal{E}$ varies its sign periodically in time with a sinusoidal behavior, the torque rotates the molecules always in the same direction because when $\mathcal{E}$ changes sign so do the induced dipoles.

Typically, the NLC response time is about $10ms$, well above the optical range.

[1] Equations (1.8) stem from the balance between the torques which act on the molecules (59).

I can now address the reorientational nonlinearity of NLC. For a finite size beam, since the director reorientation in a given point is larger for larger beam intensities, there is a nonlinear refractive index change Δn which depends on excitation. From eq. (1.10), for positive uniaxial NLC, the nonlinearity is self-focusing and the index larger for stronger intensities. Moreover, the perturbation in director distribution is more extended than the beam width due to the nonlocal interactions between the molecules, as modeled in (1.8) by the terms derived from F_d.

1.5 Spatial Solitons in Nematic Liquid Crystals

The nonlinear optical properties of liquid crystals have been extensively studied owing to some unique features. First of all, they possess a nonlinearity which is about eight orders of magnitude larger than in isotropic liquids such as CS_2 (18; 62; 63), allowing the formation of spatial solitons at very low powers ($\approx 1 - 10mW$ for waist of a few microns) with continuous wave lasers. At variance with media exhibiting an electronic response, they are highly nonlinear in a wide wavelength range (15). Moreover, in NLC the optical beam creates a waveguide able to guide other low power signals, even at a different wavelength (64). Their response time, however, is $10 - 100$ms with respect to a few fs in electronic media (60).

First direct observation of self-focusing in NLC was carried out by Braun (65); afterwards self-localization was observed in capillaries (66) with dye doped liquid crystals. Dyes have two effects: they enhance the reorientational nonlinearity by the Janossy effect (67) and induce a temperature increase due to absorption[1]. The same group investigated higher order solitons in capillaries (68) and spatial solitons in the presence of a thermal nonlinearity (69; 70)[2], both in cylindrical and planar cells. Another group focused its attention to planar waveguides (71; 72), demonstrating solitary wave propagation in (1+1)D geometries with undoped NLC.

In 2000, Peccianti et al. demonstrated optical spatial solitons in bulk undoped NLC (46) in a (2+1)D geometry with planar alignment, proving their stability via nonlocality. They overcame the Freedericksz threshold by applying a low frequency electric

[1] Undoped NLC are transparent in the visible and near infrared wavelength ranges.

[2] In this case the soliton is due to the ordinary component, being the thermal nonlinearity focusing for this component.

field: its purpose was to set an initial angle between the director and the beam wavevector[1] (73), helping soliton formation. They demonstrated nonlocal interactions between solitons (74) and the propagation of incoherent solitons (75) (see section 1.4.4). Moreover, they utilized soliton-soliton interactions to demonstrate all-optical logic gates (76). Theoretically, they developed a general model for spatial solitons in liquid crystalline media (30), demonstrating how nonlocality in NLC can be changed by altering some experimental parameter [see also (73; 77)], and proving, both experimentally and theoretically, the existence of accessible solitons (51).
Finally, the steering of spatial solitons was demonstrated by changing the applied voltage in NLC cells where the walk-off is directly observable (47). Such configuration can be used in optical demultiplexers driven by voltage, e.g. reconfigurable all-optical networks. This geometry will be analyzed in more details in the next chapter, as some of its features was studied as part of this thesis.

[1]Nonlinearity maximization corresponds to choose an initial angle equal to $\pi/4$.

2

Scalar Solitons in Nematic Liquid Crystals

2.1 Cell Geometry

Let me consider the NLC planar cell shown in fig. 2.1. Two glass slides, defining the plane yz, are separated by $a = 100\mu m$ by means of mylar spacers, and confine the liquid crystal E7 for capillarity. The internal interfaces are treated to force planar anchoring of the molecules in the yz plane, with a pre-tilt of 2° along x to give a preferential orientation to the NLC molecules, and avoid bulk disclinations (58). To control the director distribution at the discontinuity air-NLC[1] an input interface composed by a third slide was placed parallel to the plane xy, and suitably rubbed. The planar anchoring at the input interface is such that the director $\hat{\boldsymbol{n}}$ belongs to the plane xy and, furthermore, determines the molecular alignment at $\pi/4$ with respect to both x and y. A low-frequency bias V,[2] applied via two transparent Indium Tin Oxide electrodes (fig. 2.1), is used to change the director distribution in the absence of optical excitation, hence varying the medium properties. In the absence of an external bias ($\mathrm{V} = 0$), the NLC director $\hat{\boldsymbol{n}}$ in bulk lies in the plane yz (neglecting the pre-tilt angle which is small) at $\pi/4$ with respect to $\hat{\boldsymbol{z}}$, with $\hat{\boldsymbol{n}} \cdot \hat{\boldsymbol{y}} > 0$ and $\hat{\boldsymbol{n}} \cdot \hat{\boldsymbol{z}} > 0$.

As discussed in detail below, such configuration allows the direct observation of walk-off, at variance with the geometry previously used (see section 1.5).

[1] Without the interface there would be a meniscus.

[2] Frequency is chosen so that the NLC molecules respond only to temporally averaged voltages (see 1.4.4).

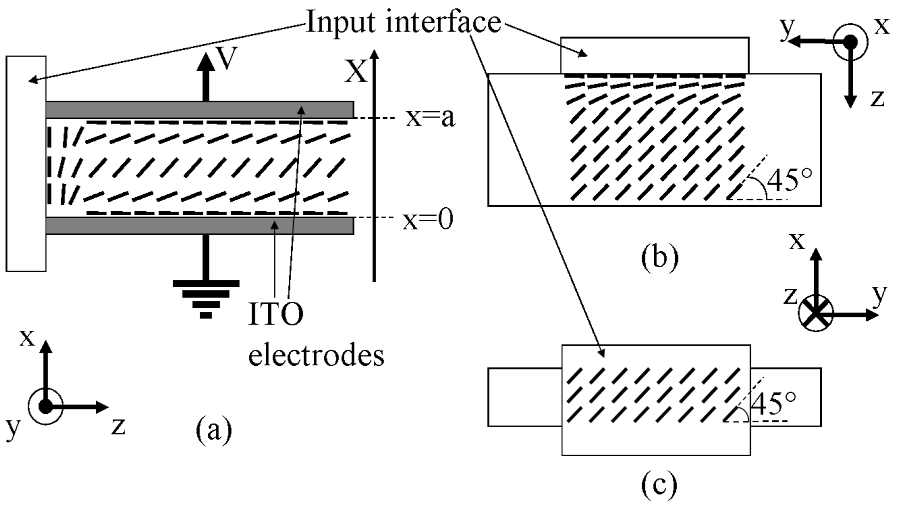

Figure 2.1: Sketch of the NLC sample: (a) side view, (b) top view, (c) front view. Voltage at $1kHz$ is applied along x via two transparent electrodes deposited onto the glass slides that define the yz plane. ITO stands for Indium Tin Oxide.

2.2 Set-Up

Fig. 2.2(a) is a sketch of the set-up employed in the experimental work. A He-Ne laser emitting at $\lambda = 633nm$ is the light source. An optical system, composed by a half-wave plate and a polarizer, is used to control beam power and polarization. Specifically, the polarization at the input interface is always linear: rotating the half-wave plate I can vary angle β, as defined in fig. 2.2(b). The beam passes through an objective lens, so that the input waist is of the order of a few microns. Light impinges normally to the input interface, with its wavevector parallel to $\hat{\boldsymbol{z}}$ and equally far from the two glasses normal to $\hat{\boldsymbol{x}}$. The field inside the sample is analyzed by the light scattered from NLC (see section 1.4.3) and collected by a microscope and a CCD[1] camera.

2.3 Effect of the Input Interface

In this section I will study, both experimentally and theoretically, the manner in which the input interface affects beam coupling in the sample, in particular the field polarization which reaches the bulk NLC.

[1]Charge Coupled Device.

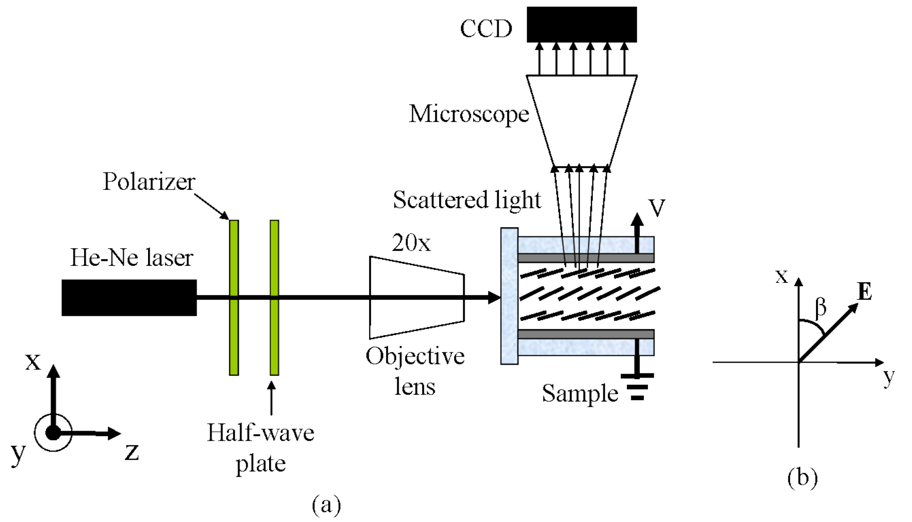

Figure 2.2: (a) Experimental set-up. (b) Input field $\mathbf{E}$ and its polarization in the plane xy at $z = 0$. i.e. at the interface between air and NLC. Sign convention is such that β shown in the figure is positive.

In order to describe the director orientation, I introduce the two angles ξ and γ, as shown in fig. 2.3.

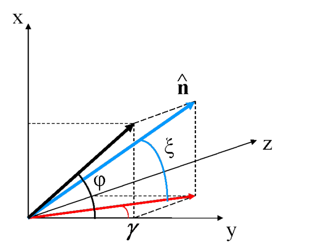

Figure 2.3: Director $\hat{\boldsymbol{n}}$ and the two angles ξ and γ used to describe its orientation in space.

As the bulk NLC is preceded by a transition layer of thickness d following the input interface in $z = 0$, I model this transition layer as an anisotropic structure stratified along z, with optical properties constant in each layer, i.e. with a dielectric tensor which does not depend on transverse coordinates xy[1]. To model finite beam behavior I take the director value in $x = a/2$,[2] given that the experimental beam width is much smaller than the cell thickness a. Under such hypotheses I can apply Berreman's method (78) to describe the propagation of electromagnetic plane waves with $\mathbf{k} = k\hat{\boldsymbol{z}}$, i.e. impinging normally on the sample. I note that the wavevector $\mathbf{k}$ cannot change direction in the transition layer under these hypotheses. Hence I cast Maxwell's equations in the form:

$$\frac{d\Phi}{dz} = i\omega\Delta(z)\Phi \tag{2.1}$$

being ω the optical angular frequency and

[1]This implies neglecting optical reorientation; such approximation will be justified later.

[2]Having neglected the optical reorientation, the profile does not change along y owing to the symmetry.

$$\boldsymbol{\Phi} = \begin{pmatrix} E_x \\ H_y \\ E_y \\ -H_x \end{pmatrix}, \boldsymbol{\Delta} = \begin{bmatrix} 0 & \mu_0 & 0 & 0 \\ \epsilon_{xx} - \frac{\epsilon_{zx}^2}{\epsilon_{zz}} & 0 & \epsilon_{xx} - \frac{\epsilon_{xz}\epsilon_{zy}}{\epsilon_{zz}} & 0 \\ 0 & 0 & 0 & \mu_0 \\ \epsilon_{xx} - \frac{\epsilon_{xz}\epsilon_{zy}}{\epsilon_{zz}} & 0 & \epsilon_{yy} - \frac{\epsilon_{zy}^2}{\epsilon_{zz}} & 0 \end{bmatrix} \tag{2.2}$$

with ϵ_{ij} $(i, j = x, y, z)$ the elements of the dielectric tensor, which depend on z due to the director rotation along the transition layer.

To numerically compute eq. (2.1) I can divide the region $0 < z < d$ into N sections, each of thickness h. In order to get a good approximation, h must be chosen so that dielectric tensor variations in each section are negligible. Hence, the vector $\boldsymbol{\Phi}$ at $z = d$ can be found by solving

$$\boldsymbol{\Phi}(d) = \left[\Pi_{\nu=0}^{N-1}\mathbf{P}_h(\nu h)\right]\boldsymbol{\Phi}(0) = \mathbf{T}_d\boldsymbol{\Phi}(0) \tag{2.3}$$

where I set $\mathbf{P}_h(z) = e^{i\omega h\Delta(z)}$. The matrix $\mathbf{P}_h(z)$ is the transfer function (for the field vector $\boldsymbol{\Phi}$) which models the section limited by z and $z + h$. Therefore $\mathbf{T}_d$ is the transfer function for the whole transition layer.

The next step is to link the dielectric tensor [related to $\boldsymbol{\Delta}$ by means of (2.2)] to the director profile (into the transition layer). To this purpose, I can use eq. (1.9) with $n_y = \cos\xi\cos\gamma$, $n_x = \sin\xi$ and $n_z = \cos\xi\sin\gamma$. Finally, I assume a certain director profile in $0 < z < d$, being $z = 0$ the input interface. Specifically, I take a linear trend for ξ and γ. A direct computation from eq. (2.3) confirms that specific profiles do not affect polarization, which mainly depends on how fast the director angle varies along z, i.e. from 0 to d, if the total variation is constant.

Now I have to establish the director position in $z = 0$ and $z = d$. It is easily seen that, given the boundary conditions at the input interface, $\gamma(x, y, z = 0) = 0$ and $\xi(x, y, z = 0) = \pi/4$, independently from the applied voltage V. At $z \geq d$ the bulk NLC has $\gamma(x, y, z = d) = \gamma_{bulk} = \pi/4$. Conversely, $\xi(x, z = d) = \xi_{bulk}(x)$ changes with V and is found by solving the reorientational equation derived from eq. (1.8) together with the associated electrostatic equation for $z > d$. Therefore, I have to solve the ODE (Ordinary Differential Equation)[1] system (79; 80)

[1]The unknown quantities V and ξ_{bulk} exclusively depend on x.

$$\left(\epsilon_{\parallel} \sin^2 \xi_{bulk} + \epsilon_{\perp} \cos^2 \xi_{bulk}\right) \frac{d^2 V}{dx'^2} + \Delta\epsilon_{LF} \sin(2\xi_{bulk}) \frac{d\xi_{bulk}}{dx'} \frac{dV}{dx'} = 0 \tag{2.4}$$

$$\begin{aligned}\left(K_3 \sin^2 \xi_{bulk} + K_1 \cos^2 \xi_{bulk}\right) \frac{d^2 \xi_{bulk}}{dx'^2} + \frac{K_3 - K_1}{2} \sin(2\xi_{bulk}) \left(\frac{d\xi_{bulk}}{dx'}\right)^2 \\ + \frac{\Delta\epsilon_{LF}}{2} \sin(2\xi_{bulk}) \left(\frac{dV}{dx'}\right)^2 = 0\end{aligned} \tag{2.5}$$

being V the electrostatic potential. I introduced a new reference system $x'y'z'$ defined by $\boldsymbol{\hat{y}'} = \boldsymbol{\hat{n}}(\mathrm{V} = 0)$, $\boldsymbol{\hat{x}'} = \boldsymbol{\hat{x}}$ and $\boldsymbol{\hat{z}'} = \boldsymbol{\hat{x}'} \times \boldsymbol{\hat{y}'}$. In eqs. (2.4)-(2.5) V is the root mean square (RMS) of the voltage, K_1 and K_3 are the Frank's elastic constants for splay and bend, respectively, and $\Delta\epsilon_{LF}$ is the dielectric anisotropy at low frequencies. The boundary conditions are $V(x' = 0) = 0$, $V(x' = a) = \mathrm{V}$ and $\xi_{bulk}(x' = 0) = \xi_{bulk}(x' = a) = 2\pi/180$, the last one stemming from the pre-tilt (see section 2.1). The system composed by eqs. (2.4) and (2.5) has to be solved numerically: results for various V are shown in fig. 2.4.

As stated above, I need to know ξ in $x = a/2$ in bulk NLC. From fig. 2.4(a) this corresponds to the maximum ξ for a fixed V, i.e. $\xi_{max}(\mathrm{V})$.

Taking a linear input polarization at the first slice (see section 2.2), I can split the electric field vector into ordinary (o) and extraordinary (e) components; the latter matches the director orientation in $z = 0$. From eq. (2.3) and taking $d = 20\mu m$, I find that the input e component transfers nearly all its power to the e-wave in the bulk NLC for every V; similarly, o-wave components in $z = 0$ remain o-waves in bulk. This is represented by the two straight horizontal lines in fig. 2.5(b) at $\beta = 45°$ (e input) and $\beta = 135°$ (o input): as the bias increases, for every $z > d$ the director elevation increases as well [see fig. 2.4(c)], and the NLC principal axes rotate. e- and o-wave input components, however, remain decoupled as they evolve through the transition layer. Otherwise stated, if the rotation of the NLC dielectric tensor with z is slow enough that the index change is adiabatic, the e-wave displacement field $\mathbf{D}_e$ rotates with z, remaining parallel to the director projection onto xy (58). It is clear how this result maintains its validity also for larger d; hence, given that transition layers d are about $100\mu m$, the numerical results retain their validity also for the cell in fig. 2.1.

To validate these predictions, I varied V and experimentally studied the input polarization maximizing energy coupling on the e (o) component. For low V, it is easy

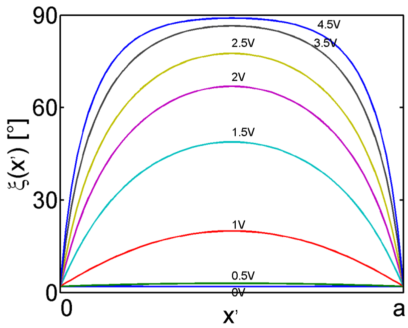

(a) Reorientation angle versus x'

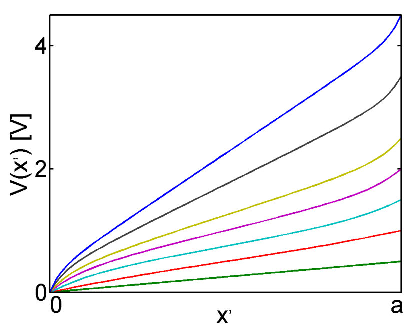

(b) Electrostatic potential versus x'

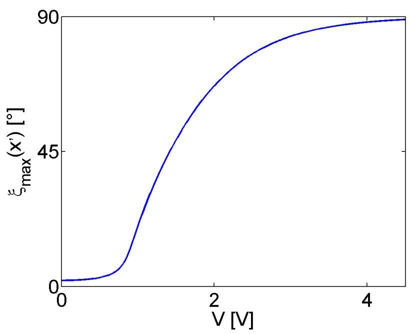

(c) Maximum reorientation angle ξ_{max} versus V

Figure 2.4: Reorientation angle ξ [fig. 2.4(a)] and electrostatic potential V [fig. 2.4(b)] inside the cell for applied voltages ranging from 0 to $4.5V$. In fig. 2.4(c) is plotted the maximum angle ξ, labeled ξ_{max}, versus applied voltage V. From fig. 2.4(a) ξ_{max} is always placed in $x' = a/2$, as predictable given problem symmetry.

to distinguish the two components inside the sample, i.e. in the bulk NLC, because the extraordinary component has a Poynting vector not parallel to $\hat{\boldsymbol{z}}$, due to walk-off[1] [section 1.4.3] [fig. 2.5(a)]. For high V, the two components begin to overlap with each other. In this range, I can use scattering to discriminate them: there is a 100% coupling on the extraordinary component when the scattered power towards the CCD camera is maximum. In fact, for V > $2V$, at certain input power, it is $\frac{P_{se}}{P_{so}} > 9.6$, where P_{se} and P_{so} are the power scattered from the NLC along $\hat{\boldsymbol{x}}$ when all the input power is coupled on e and o components, respectively [for a more detailed discussion about scattering in this configuration see appendix A.1].

[1] Moreover, for high enough input powers, only extraordinary wave is self-focused due to the Freedericksz threshold.

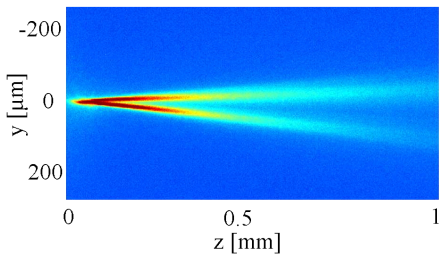

(a) Ordinary and extraordinary wave propagation.

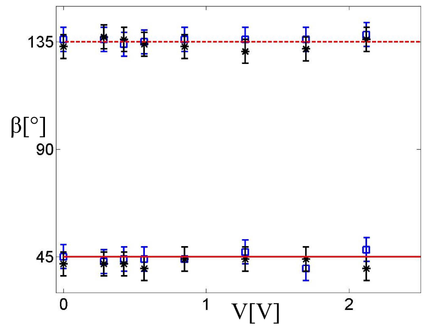

(b) Plots of optimum β.

Figure 2.5: (a) Acquired optical field distribution when input beam excites both e and o components. The Poynting vector of the ordinary wave is parallel to z, while the extraordinary one bends towards larger y due to walk-off. The power is low and the extraordinary wave does not induce any nonlinear effects. (b) Input polarization angle β versus applied voltage V. The solid (dashed) line from the model represents the optimum angle β that allows all the injected power to be transferred to an e (o) wave in bulk NLC ($z > d$). Such an angle remains fixed at 45° (135°) as the bias varies. Symbols are measured data, from linear ($20mW$; squares) to nonlinear ($3mW$; stars) regimes.

I found that the angle β which maximizes power coupling into the extraordinary component does not change with V and corresponds to the director direction at the input interface, as predicted [fig. 2.5(b)]. Furthermore, to couple all the input power to the ordinary it is sufficient to use an input polarization normal to $\hat{\boldsymbol{n}}$ in $z = 0$. Finally, transition layer effects on beam polarization remain unchanged when the power is varied: the phenomenon is linear, justifying the employed hypotheses.

2.4 Soliton Observation

This section concerns the acquisition of beam profiles inside the NLC sample, when varying its input power, polarization and the applied bias. As demonstrated in section 2.3, in order to couple all the input power into e (o) it is sufficient to select an input polarization such that $\beta = 45°(135°)$ (see fig. 2.2).

When an ordinary polarization is used, its energy propagation direction is parallel to z and the beam diffracts in the same way for every input power and bias V; in fact, due to the Freedericksz transition, nonlinearity does not take place at the mW excitations normally employed for solitons. An example is shown in fig. 2.6.

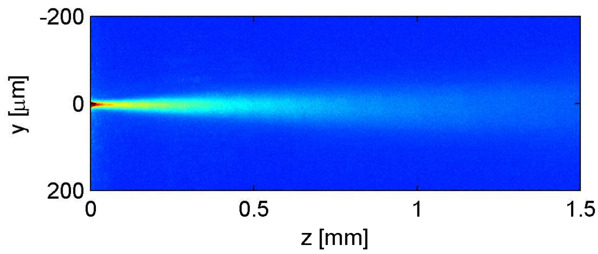

Figure 2.6: Ordinary propagation in the cell.

Instead, when the extraordinary polarization is excited, the Poynting vector $\mathbf{S}_e$ is in general not parallel to z. To a first approximation, in order to find $\mathbf{S}_e$, I can treat the beam as a plane wave[1], which propagates in a homogeneous uniaxial medium with the optical axis given by director in $x = a/2$. Thus, I consider a director as in fig. 2.3, but with $\xi = \xi_{max}$ (which depends on the applied bias, see section 2.3).

The vector $\mathbf{S}_e$, in general, does not lie on plane yz, as in fig. 2.7. Since in the experiments I observe the beam projection on the plane yz, I introduce α as the angle between the axis z and the projection of $\mathbf{S}_e$ on the plane yz (fig. 2.7); I call it apparent walk-off (47), given by (79) $\alpha = \arctan(\tan\delta\cos\varphi)$, where $\varphi = \arctan\left(\frac{\tan\xi_{max}}{\cos\gamma}\right)$ is the angle between $\hat{\boldsymbol{y}}$ and the projection of $\hat{\boldsymbol{n}}$ on the plane xy (see fig. 2.3) and δ is the walk-off defined in section 1.4.3: in this case $\theta = \arctan\left(\frac{1}{\cos\varphi\tan\gamma}\right)$. The relation between V and α (the information obtained from experiments) is shown in fig. 2.8(b). The acquired trajectories of e-beam in the plane yz are almost straight lines. Straight lines interpolations of the acquired trajectories in the observation plane yz are shown in fig. 2.8(a). Note how the beam slightly oscillates around the straight lines, this effect being stronger for intermediate V: this is due to

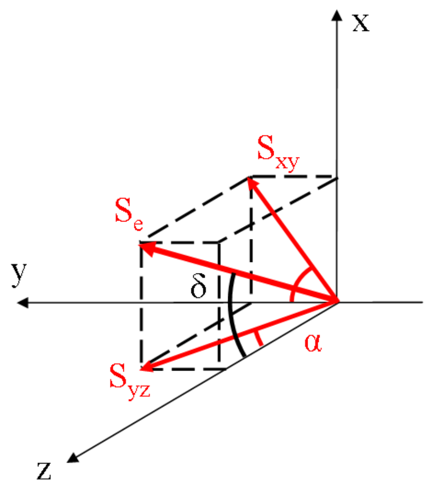

Figure 2.7: Extraordinary Poynting vector $\mathbf{S}_e$.

[1]The validity of such approach for small perturbations is discussed in section 2.5.

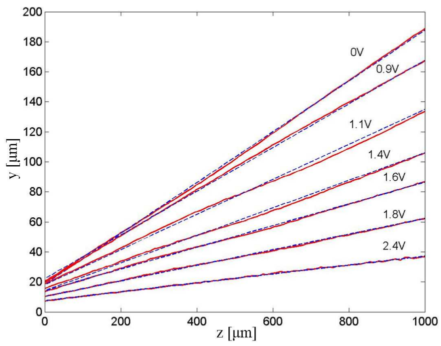

(a) Soliton trajectories in the plane yz for various V.

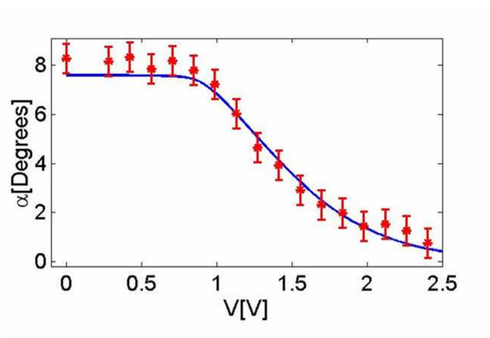

(b) Apparent walk-off angle α versus V.

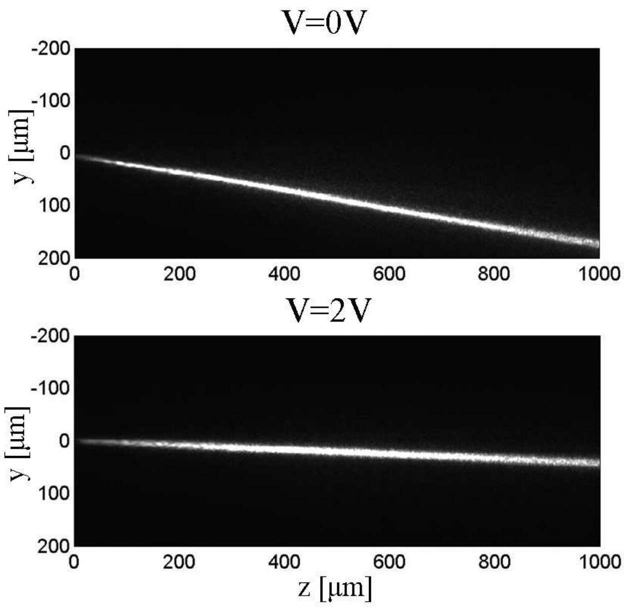

(c) Acquired solitons for V $= 0V$ and V $= 2V$, respectively.

Figure 2.8: (a) Soliton trajectories in the plane yz: dashed and solid lines are interpolating straight lines and actual beam trajectories in the plane yz, respectively. (b) Apparent walk-off α versus applied bias V: error bars are experimental data (from the slopes of the interpolating lines), whereas the solid line is the theoretical prediction. (c) Experimental images of solitons for V $= 0V$ and V $= 2V$. The soliton width is narrower in the first case due to the stronger nonlinearity.

beam oscillations in the plane xz (81), caused by the x component of $\mathbf{S}_e$, which moves the beam away from the mid-plane where α assumes different values, and by the linear index well induced by V, which traps the light around the mid-plane. As V varies, α changes because $\hat{\boldsymbol{n}}$ starts to rotate; its behavior is plotted in fig. 2.8(b). In absence of bias, α is equal to δ and is about 8°; as V increases, $\mathbf{S}_e$ gets monotonically closer to the axis z until, for high V, S_e becomes parallel to $\hat{\boldsymbol{z}}$ as the director is reoriented along $\hat{\boldsymbol{x}}$, i.e. $\delta = 0$. Moreover, $\mathbf{S}_e$ does not change its mean direction versus coupled power (79), proving that optical reorientation is negligible as compared to that induced by the low frequency electric field.

Let me discuss the beam profile inside the NLC cell. At low powers the beam diffracts, analogously to the ordinary case (fig. 2.6). Increasing power, self-focusing effects begin to appear until the optical reorientation creates a self-induced waveguide (section 1.4.4). When self-focusing counterbalances beam spreading due to diffraction, a shape-invariant field, i.e. a soliton [fig. 2.8(c)], forms. Such phenomenon is qualitatively explained in fig. 2.9: the NLC director is more reoriented where the intensity is stronger, inducing a nonlinear index well Δn, wider than the intensity profile I due to the nonlocality.

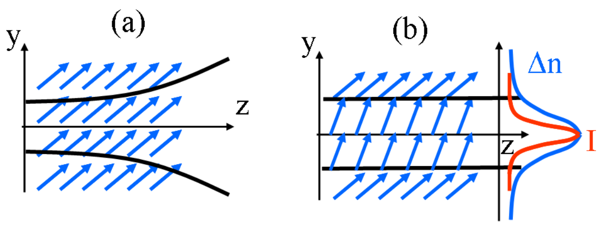

Figure 2.9: (a) Linear diffraction. (b) Soliton propagation. Blue arrows represent the NLC director.

2.5 Theory of Nonlinear Optical Propagation in NLC

2.5.1 Ruling Equation

Let me consider a homogeneous NLC sample and an extraordinary field E_{opt} with spatial spectrum centered around $\mathbf{k} = k\hat{\boldsymbol{z}}$, i.e. $\mathbf{E}_{opt} = E_e e^{ikz}$ with E_e slowly varying along z. I call θ_0 the angle between $\mathbf{k}$ and the unperturbed director and δ the walk-off for a plane wave with the same wavevector[1]. I take $\mathbf{k} = n_e k_0$, being k_0 the vacuum wavenumber and n_e the linear extraordinary index. Moreover, I define a new reference system rts, where $\hat{\boldsymbol{s}}$ and $\hat{\boldsymbol{t}}$ are parallel to the Poynting and the electric fields, respectively, and $\hat{\boldsymbol{r}} = \hat{\boldsymbol{t}} \times \hat{\boldsymbol{s}}$. Starting from Maxwell's equation and considering only extraordinary components, at the first order the field is polarized along t and obeys the equation (a complete derivations is reported in appendix A.2) (47; 52)

$$2ik_0 n_e \cos\delta \frac{\partial E_e}{\partial s} + D_t \frac{\partial^2 E_e}{\partial t^2} + D_r \frac{\partial^2 E_e}{\partial r^2} + k_0^2 \delta\epsilon_{tt} E_e = 0 \tag{2.6}$$

where $\delta\epsilon_{tt} = \hat{\boldsymbol{t}}\cdot\boldsymbol{\epsilon}\cdot\hat{\boldsymbol{t}}$ is the nonlinear index variation, $D_r = 1 + \frac{n_e^2 \sin^2\delta}{\lambda_x}$ and $D_t = \frac{n_e^2 \cos^2\delta}{\lambda_s}$ are diffraction coefficients (section A.2), different each other due to the anisotropy. I stress that eq. (2.6) is a scalar NLSE equation [see eq. (1.2)], written along propagation coordinate s[2]. Therefore, for small perturbations, the nonlinear optical propagation in anisotropic NLC can be described as in isotropic media.

Now I have to apply eq. (2.6) to the cell geometry sketched in fig. 2.1. Eq. (2.6) confirms the hypotheses made in section 2.4 to model the soliton trajectory dependence on the applied bias V, when the soliton was approximated by a plane wave.

Now I have to determine $\delta\epsilon_{tt}$, which depends on director reorientation. When V is not zero, there is a low frequency field parallel to $\hat{\boldsymbol{x}}$ and an optical field directed like $\hat{\boldsymbol{t}}$: I need to use two angles to describe the director distribution.[3] Moreover, in order to get a good approximation, I need to take into account the index well induced by V in the plane xs and, thus, use vectorial equations.

Keeping in mind these considerations, hereafter and for the sake of simplicity, I limit the investigation to V = 0: in this case the director reorientation takes place only in the yz plane, being E_e linearly polarized along $\hat{\boldsymbol{t}}$, and the transformation from xyz to rts is a simple rotation around x by an angle δ. Being $\hat{\boldsymbol{r}} = \hat{\boldsymbol{x}}$ I call the new reference system xts. From section 1.4.2 the director profile is governed by

$$K\nabla_{xt}^2 \theta + \frac{\epsilon_0 \epsilon_a}{4} \sin\left[2(\theta - \delta)\right] |E_e|^2 = 0 \tag{2.7}$$

[1] see section 1.4.3.

[2] Therefore it is written in the paraxial approximation along s.

[3] The two directions coincide for high V when all the molecules are parallel to x, but this case is not interesting because the reorientational nonlinearity goes to zero.

having neglected the derivative along s, as already discussed in section 1.3. The nonlinear index perturbation is

$$\delta\epsilon_{tt} = \epsilon_a \left[\sin^2(\theta - \delta) - \sin^2(\theta_0 - \delta)\right] \tag{2.8}$$

2.5.1.1 The Highly Nonlocal Case

Let me define the nonlinear perturbation of the director angle $\Psi = \theta - \theta_0$. For small Ψ, eq. (2.7) becomes

$$K\nabla^2_{xt}\Psi + \frac{\epsilon_0\epsilon_a}{4}|E_e|^2 \sin\left[2(\theta_0 - \delta)\right] + \frac{\epsilon_0\epsilon_1}{2}|E_e|^2 \cos\left[2(\theta_0 - \delta)\right]\Psi = 0 \tag{2.9}$$

I assume the optical field E_e is cylindrically symmetric, which means Ψ has the same property if asymmetric boundary conditions are neglected (actually, this is true also for asymmetric boundary conditions for the zone close to the beam peak if the beam waist is negligible compared to the cell size: see sections 2.5.2.1 and 2.5.2.2). I can write the field and the perturbation using a Taylor series around $x = a/2,\ t = 0$

$$\Psi = \Psi_0 + \Psi_2\left[(x - a/2)^2 + t^2\right] + o\left[(x - a/2)^2 + t^2\right] \tag{2.10}$$

$$|E_e(x,t)|^2 = f_0 + f_2\left[(x - a/2)^2 + t^2\right] + o\left[(x - a/2)^2 + t^2\right] \tag{2.11}$$

being $\Psi_0 = \Psi|_{x=a/2,t=0}$ and $f_0 = |E_e|^2|_{x=a/2,t=0}$ the maxima of the induced perturbation and the field, respectively, whereas $\Psi_2 = \frac{1}{2}\frac{\partial^2\Psi}{\partial x^2}\Big|_{x=a/2,t=0}$ and $f_2 = \frac{1}{2}\frac{\partial^2|E_e|^2}{\partial x^2}\Big|_{x=a/2,t=0}$. Substituting eqs. (2.10) and (2.11) into (2.9) I get:

$$\begin{aligned}
4K\Psi_2 + o\left[(x - a/2) + t\right] + \\
\frac{\epsilon_0\epsilon_a}{4}\left\{f_0 + f_2\left[(x - a/2)^2 + t^2\right] + o\left[(x - a/2)^2 + t^2\right]\right\}\sin\left[2(\theta_0 - \delta)\right] + \\
\frac{\epsilon_0\epsilon_a}{2}\left\{f_0 + f_2\left[(x - a/2)^2 + t^2\right] + o\left[(x - a/2)^2 + t^2\right]\right\} \\
\left\{\Psi_0 + \Psi_2\left[(x - a/2)^2 + t^2\right] + o\left[(x - a/2)^2 + t^2\right]\right\}\cos\left[2(\theta_0 - \delta)\right] = 0
\end{aligned} \tag{2.12}$$

From eq. (2.12) all the coefficients in front of every power of x or t must be equal to 0. For the zero-th order power this gives

$$4K\Psi_2 + \frac{\epsilon_0\epsilon_a}{4}f_0\sin\left[2(\theta_0 - \delta)\right] + \frac{\epsilon_0\epsilon_a}{2}f_0\Psi_0\cos\left[2(\theta_0 - \delta)\right] = 0 \tag{2.13}$$

From eq. (2.13) it is straightforward to compute the coefficient Ψ_2 (51)

$$\Psi_2 = -\frac{\epsilon_0 \epsilon_a}{8K} f_0 \left\{ \frac{\sin\left[2(\theta_0 - \delta)\right]}{2} + \Psi_0 \cos\left[2(\theta_0 - \delta)\right] \right\} \tag{2.14}$$

It is important to remark that eq. (2.14) is obtained without approximations: it is valid whenever beam and perturbation are radially symmetric. The approximation is given by the use of the parabolic term in the power expansion of the angle distribution, justified in the highly nonlocal case (31; 51). In general, the perturbation peak Ψ_0 depends on every term of the power expansion, including the effects due to the boundary conditions.

For small perturbations eq. (2.8) becomes $\delta\epsilon_{tt} \cong \epsilon_a \sin\left[2(\theta_0 - \delta)\right] \Psi$; hence, finally I get

$$\delta\epsilon_{tt} = \epsilon_a \sin\left[2(\theta_0 - \delta)\right] \left\{ \Psi_0 + \Psi_2 \left[(x - a/2)^2 + t^2 \right] \right\} \tag{2.15}$$

which is the searched parabolic index well.

The term $\epsilon_a \sin\left[2(\theta_0 - \delta)\right] \Psi_0$ represents a rest energy, which depends on beam shape. In general, its value changes as light propagates along s, but it is constant for a solitary wave. Conversely, the term Ψ_2 depends on f_0, i.e. the peak intensity, owing to the high nonlocality. Assuming $D_x = D_t = D$[1], from quantum harmonic oscillator theory (31; 49) it stems that solitons of any order are expressed by Hermite-Gauss modes

$$E_e{}^{mn} = A_0 \sqrt{\frac{\Omega}{\pi}} \frac{1}{\sqrt{2^{m+n} n! m!}} H_m \left[\sqrt{\Omega}(x - a/2) \right] H_n \left(\sqrt{\Omega} t \right) e^{-\frac{\Omega\left[(x-a/2)^2 + t^2\right]}{2}} e^{i\beta_{mn} s} \tag{2.16}$$

where $\Omega = \sqrt{-\frac{k_0^2 \epsilon_a \sin[2(\theta_0 - \delta)] \Psi_2}{D}}$, $\beta_{mn} = (n + m + 1)\frac{\Omega D}{k_0 n_e \cos\delta}$ and H_n is the nth-degree Hermite's polynomial, whereas A_0 is a constant dependent on soliton power. Given that Ω depends on soliton power through Ψ_2,[2], solitons with a fixed width exists only for a certain power.

Considering the $m = n = 0$ case (i.e. the lowest order soliton featuring a Gaussian

[1]Actually, this hypothesis is not necessary if I define the new transverse coordinates $x' = x/\sqrt{D_x}$, $t' = t/\sqrt{D_t}$.

[2]When a specific beam shape is taken as in eq. (2.16) the relationship between f_0 and P is a known linear function depending on parameter Ω.

shape $E_e \propto \exp\left[-\frac{(x-a/2)^2+t^2}{w_S^2}\right]$), I obtain that, given a waist w_S and neglecting the Ψ_0 term in eq. (2.14), the soliton power P_S is

$$P_S = \left(\frac{16\pi K D n_e}{\epsilon_0 \epsilon_a^2 Z_0 k_0^2 \sin^2[2(\theta_0 - \delta)]}\right)\frac{1}{w_s^2} \tag{2.17}$$

in agreement with Refs. (31; 51; 52). Eq. (2.17) provides the existence curve for lowest order solitons (in NLC cell as described in fig. 2.10) under the highly nonlocal approximation.

2.5.2 Numerical Simulations

Resuming former results, the nonlinear optical propagation in the cell depicted in fig. 2.10 and for V = 0 is ruled by the PDE system

$$\begin{aligned} 2ik_0 n_e \cos\delta \frac{\partial E_e}{\partial s} + D_t \frac{\partial^2 E_e}{\partial t^2} + D_x \frac{\partial^2 E_e}{\partial x^2} + k_0^2 \epsilon_a \left[\sin^2(\theta - \delta) - \sin^2(\theta_0 - \delta)\right] E_e = 0 \\ K \nabla_{xt}^2 \theta + \frac{\epsilon_0 \epsilon_a}{4} \sin\left[2(\theta - \delta)\right] |E_e|^2 = 0 \end{aligned} \tag{2.18}$$

The numerical algorithm employed to solve eqs. (2.18) is explained in full details in appendix B. I now discuss the results.

2.5.2.1 Nonlinear Propagation

In the simulations presented in this section I consider a cell of thickness $a = 100\mu m$ and $\theta_0 = \pi/4$ (see figure 2.10), filled up with liquid crystal E7 as in the experiments previously discussed. Thus, in eqs. (2.18) I use E7 parameters: $K = 12 \times 10^{-12} N$ and index dispersion as in fig. 2.11 (79; 82).

I take Gaussian input beam profiles, $E_e(x, t, s = 0) = \sqrt{\frac{4Z_0 P}{\pi n_e w_{in}^2}} e^{-\frac{x^2+t^2}{w_{in}^2}}$, being Z_0 the vacuum impedance, P the power and w_{in} the initial waist. I define the transverse intensity profiles $I_x(x, s) = \int_{-\infty}^{\infty} |E_e|^2 dt$ and $I_t(t, s) = \int_0^a |E_e|^2 dx$. In particular, I_t is proportional to the scattered light experimentally acquired with the set-up shown in fig. 2.2. Numerically, $I_t \approx I_x$ for beam waists less than $10\mu m$: such property will be further detailed in section 2.5.2.2.

Fig. 2.12 shows the simulations for the case $P = 1mW$, $w_{in} = 2.5\mu m$ and $\lambda = 633nm$.

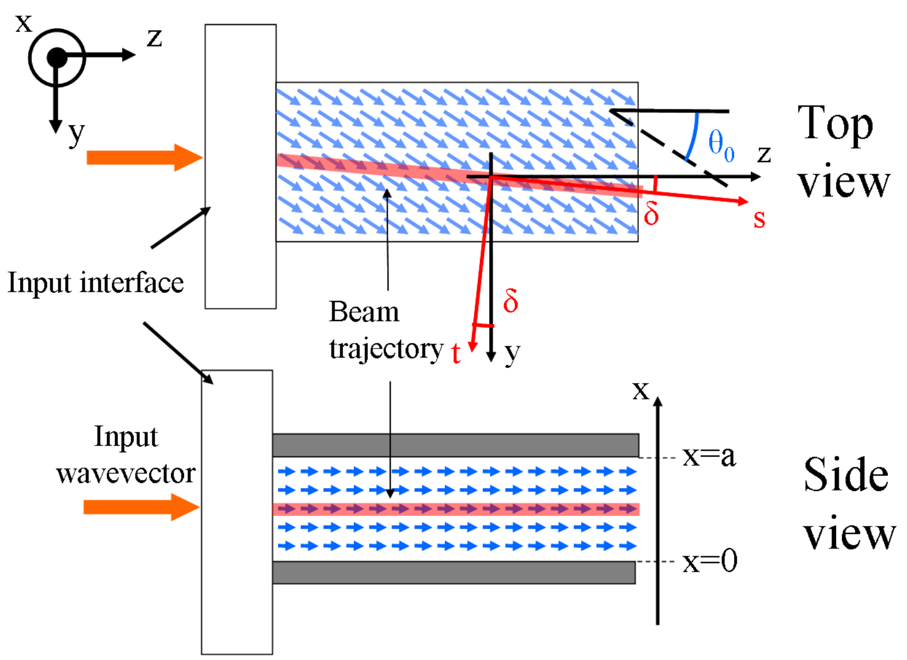

Figure 2.10: Extraordinary-wave propagation in a NLC cell for V = 0: beams are launched in $x = a/2$ and impinge normally to the input interface.

The beam is self-confined, with waist oscillating sinusoidally along s (the so-called *breathing*) as theoretically predicted in the highly nonlocal case (31; 51), making almost three oscillations between $s = 0$ and $s = 2mm$. Moreover, self-localization takes place for $P = 1mW$, in agreement with the experimental observations (section 2.4). The profile θ changes slightly across s, because the variations in beam waist are small.

Next, I discuss what happens to the beam profile when the power is increased, for the same initial waist w_{in}. Results are reported in fig. 2.13: for $P = 0.1mW$ self-focusing is not strong enough to overcome diffraction. For $P = 1$ and $3mW$ the beams are able to self-localize, with breathing period decreasing for larger power, whereas the breathing amplitude decreases.

The waist trend is systematically investigated in fig. 2.14, where the beam waist is plotted versus propagation s and initial value w_{in}, for four powers and two wavelengths $\lambda = 633$ and $1064nm$.

Comparing soliton breathing for different powers and considering the same initial waist w_{in}, the breathing period decreases as power increases. I note how for every power

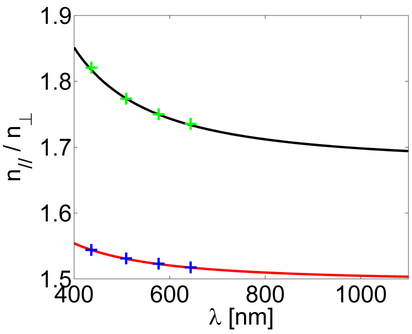

Figure 2.11: NLC E7: refractive indices $n_{\|} = \sqrt{\epsilon_{\|}}$ (black curve) and $n_{\perp} = \sqrt{\epsilon_{\perp}}$ (red curve) versus vacuum wavelength λ. Dots are experimental values, lines are interpolations.

there is a certain initial waist such that the beam width variations in propagation are very small: this corresponds to the soliton condition, and the beam profile changes slightly along s because the actual soliton shape is not perfectly Gaussian (see next section). For w_{in} smaller than the soliton condition, the beams broaden after the input because diffraction overcomes self-focusing. Conversely, for larger w_{in} the beams at the beginning shrink, being the nonlinear lens stronger than diffraction. I also note that the oscillations are periodic close to the soliton condition, but lose their periodicity when input conditions are far from the soliton condition. The reason is that, for large variations in beam waist, the coefficients Ψ_2 and Ψ_0 defined above change strongly along s and the periodic solutions typical of quantum harmonic oscillators are no longer valid. The breathing amplitude is as large as the initial condition is far from the soliton condition.

Finally, I stress that the breathing period increases for longer wavelength (for all the other parameters fixed) owing to the stronger diffraction.

2.5.2.2 Soliton Profile

To derive soliton profile and existence curve, I consider a beam preserving its intensity profile along s, i.e. $E_e = \sqrt{\frac{2Z_0P}{n_e}}u(x,t)e^{i\beta s}$, with u a real function and P the soliton power. Substituting it into eq. (2.18) I get

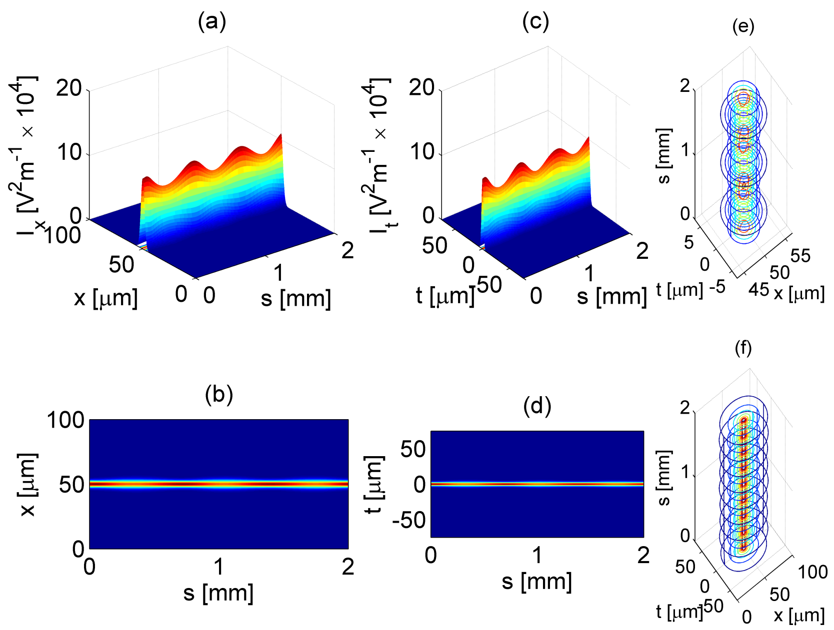

Figure 2.12: Numerical results for a Gaussian input with $P = 1mW$ and initial waist $w_{in} = 2.5\mu m$. (a-b) Intensity I_x in the plane xs. (c-d) Intensity I_t in the plane ts. (e and f) Contour plots of the optical intensity and director angle θ in the 3D space, respectively. Wavelength is equal to $633nm$.

$$D_t\frac{\partial^2 u}{\partial t^2} + D_x\frac{\partial^2 u}{\partial x^2} + \left\{k_0^2\epsilon_a\left[\sin^2(\theta-\delta) - \sin^2(\theta_0-\delta)\right] - 2k_0 n_e\beta\cos\delta\right\}u = 0 \tag{2.19}$$

$$K\nabla_{xt}^2\theta + \frac{\epsilon_0\epsilon_a Z_0 P}{2n_e}\sin\left[2(\theta-\delta)\right]|u|^2 = 0 \tag{2.20}$$

The former system is a nonlinear eigenvalue problem, with β the eigenvalue which gives the soliton phase velocity and u a real function which represents the soliton intensity. I focus my attention to the fundamental soliton, i.e. a soliton with no nodes, consistently with the excitations used in the experiments.

The system composed by eqs. (2.19) and (2.20) was solved numerically, fixing the power carried out by the solitary wave. The implemented algorithm is as follows: I start with a guess on soliton profile, choosing an initial profile with a bell shape[1]; then, I substitute

[1] In particular, as initial guess I use a fundamental Gaussian beam, solution in the highly nonlocal limit, i.e., when taking into account a parabolic index well.

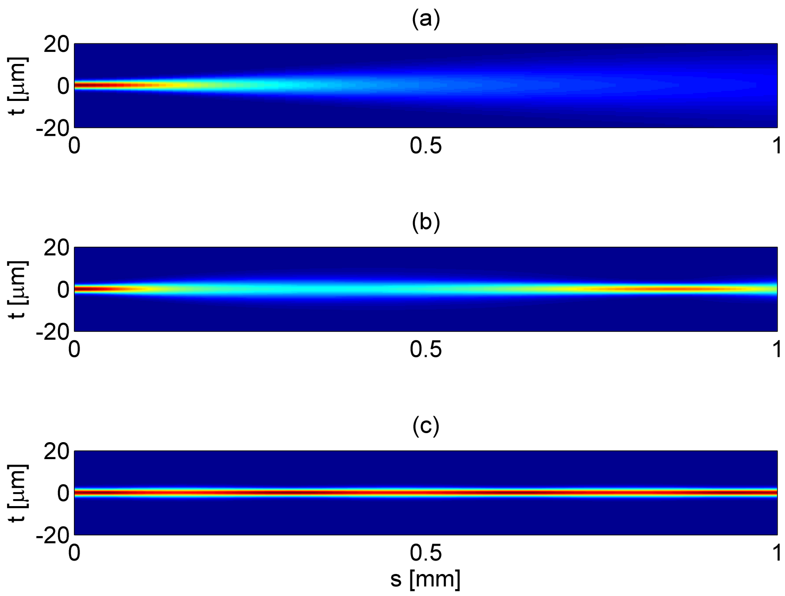

Figure 2.13: Plot of I_t on the plane ts for $w_{in} = 3.5\mu m$ and $P = 0.1$ (a), 1 (b) and $3mW$(c). In the first case beam linearly diffracts, whereas in the other two cases solitary propagation takes place. Wavelength is equal to $633nm$.

the found value into eq. (2.20) and compute the corresponding θ distribution. I iterate the procedure until self-consistency is achieved (34; 83). Higher order solitons can be found out by simply changing the initial guess.

As an example, the computed u for $P = 0.5mW$ at $\lambda = 633nm$ is shown in fig. 2.15(a and c). The angle θ is sketched in fig. 2.15(b and d): profile is asymmetric due to the different boundary conditions along the two transverse dimensions, but close to the cell center, i.e. the intensity peak position, is nearly symmetric. Consequently, the beam is nearly cylindrically symmetric, *perceiving* the same index well in all the transverse plane. Such property will be analytically demonstrated in the next chapter.

In fig. 2.16(a-d) the numerically calculated soliton profiles for four powers are compared with Gaussian best-fits: the actual solitary shapes are almost Gaussian, in agreement with the hypothesis of high nonlocality for the NLC, with slight departures only on the tails. Another consequence of the NLC high nonlocality is that the soliton existence curve on the plane waist-power goes like $P \propto waist^2$ [eq. (2.17) and fig. 2.16(e)]

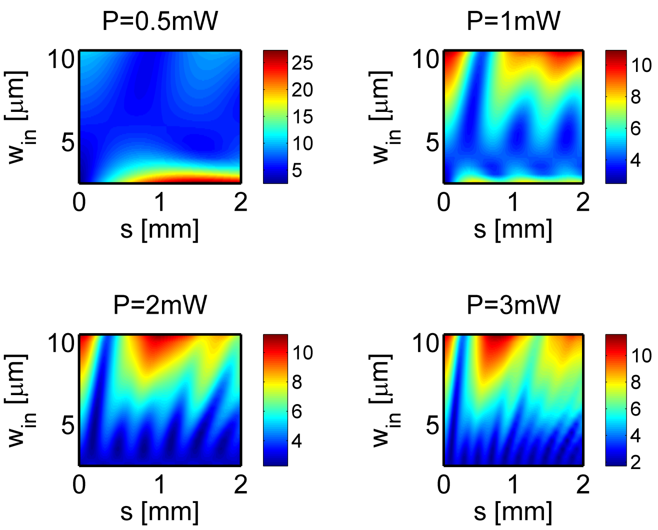

(a) $\lambda = 633nm$.

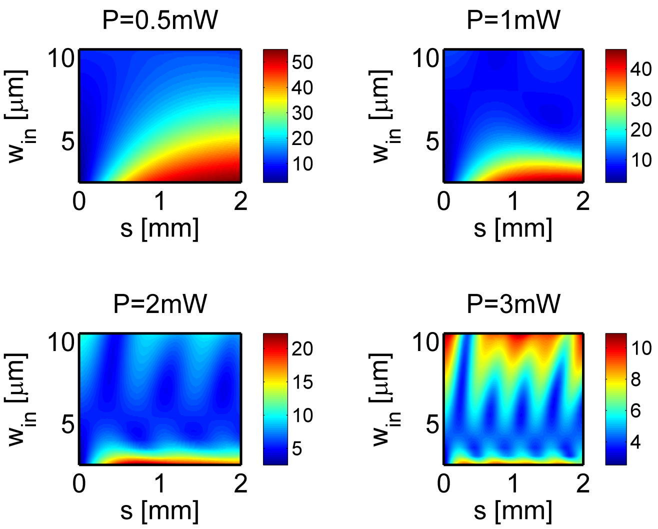

(b) $\lambda = 1064nm$.

Figure 2.14: Plots of beam waist versus input waist w_{in} and propagation coordinate s at $\lambda = 633nm$ (a) and $\lambda = 1064nm$ (b), for four different powers. Values reported in the colorbars are in microns.

(31; 51; 52). Furthermore, given the larger diffraction at longer wavelengths, for a fixed power soliton the waist is larger for infrared beams than for red ones. Fig. 2.16(f-g) plots the maximum of θ and u versus soliton power, respectively. Values corresponding to red are larger due to the smaller waist, for the same power.

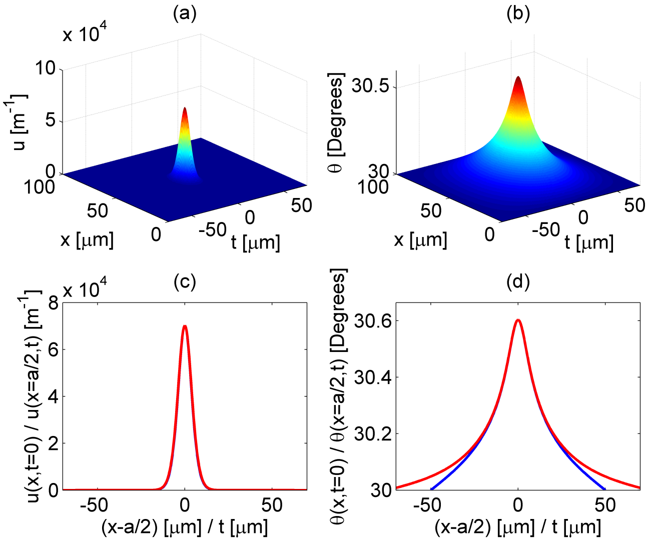

Figure 2.15: Soliton profile u (a) and corresponding θ distribution (b) in the plane xt, for $P = 0.5mW$ and $\theta_0 = \pi/6$. (c) and (d) show the sections in the planes $x = a/2$ (red line) and $t = 0$ (blue line) for u and θ, respectively. The wavelength is $633nm$.

I verified the previous results by computing, via the numerical code described in appendix B, the optical field propagation when the input beam profile is equal to the soliton shape for a given power. I find out that intensity profile and index perturbation do not change in propagation, for any input power. An example is shown in fig. 2.17, where the 3D plot of $|u|^2$ and angle θ is plotted, clearly demonstrating shape invariance in propagation.

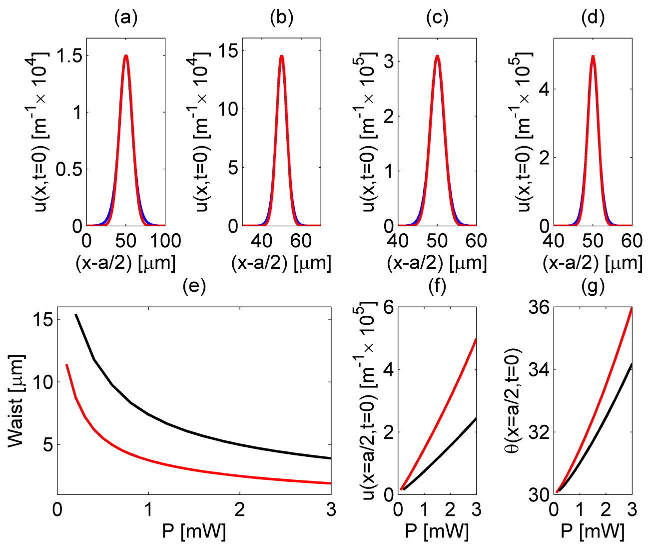

Figure 2.16: Numerically computed soliton profile $u(x, t = 0)$ versus $x - a/2$ (blue line) and corresponding best-fit with a Gaussian (red line) for $P = 0.1$ (a), 1 (b), 2 (c) and $3mW$ (d), at $\lambda = 633nm$. (e) Soliton existence curve in the plane waist-power at $\lambda = 633nm$ (red) and $\lambda = 1064nm$ (black). Waist of the Gaussian which best-fits the actual soliton shape is taken into account. Plot of maximum u (f) and θ (g) versus soliton power; red and black curves correspond to $\lambda = 633$ and $1064nm$, respectively.

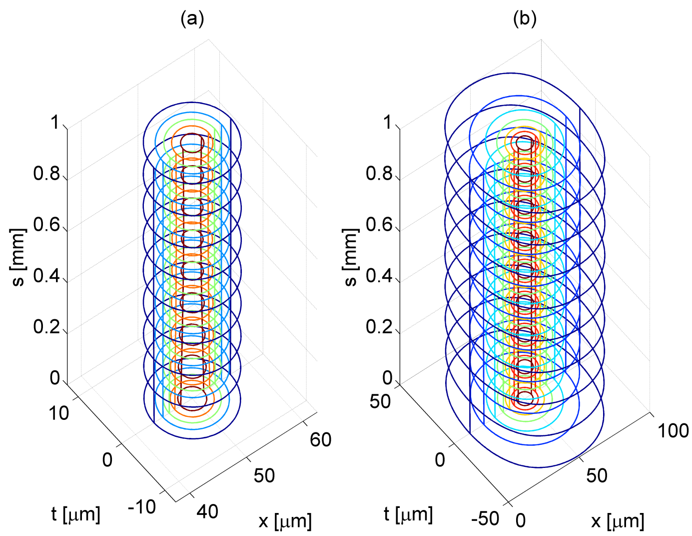

Figure 2.17: Contour plots of numerically computed intensity profile $|u|^2$ (a) and director angle θ (b) in the space xts for $P = 1mW$ and $\lambda = 633nm$, when the input beam is solution of eqs. (2.19)-(2.20).

3

Nonlocality and Soliton Propagation

3.1 Definition

As discussed in chapter 1, nonlinear light-beam propagation in nonlocal media can be described in the paraxial approximation by a nonlocal nonlinear Schröedinger equation (NNLSE) (1.2):

$$2ik_0n_0\frac{\partial A}{\partial s}+\nabla_\perp^2 A+k_0^2\left(n^2-n_0^2\right)A=0 \tag{3.1}$$

where $\Delta n(I) = n(I) - n_0$ is the index variation induced by the nonlinearity, s is the propagation coordinate, $\nabla_\perp^2 = \partial/\partial x^2 + \partial/\partial t^2$ is the transverse Laplacian and $k_0 = 2\pi/\lambda$. Moreover, I assume that, in the absence of optical excitation, the medium is uniform. Hence, I can set

$$n^2-n_0^2 \cong 2n_0\Delta n+(\Delta n)^2 \tag{3.2}$$

Nonlocality relates to the fact that the beam affects some physical variable ρ[1] even at some finite distance from it, such as temperature in thermo-optic media or orientation in NLC, which, in turn, change refractive index, i.e., $n = n(\rho)$. The latter relationship models light-matter interaction.

Behavior of ρ in the nonlinear medium is typically ruled by a partial differential equation (PDE) in the form $F = F(\rho, I) = 0$, where an intensity-dependent ρ is cast in the

[1]If the refractive index depends on more than one quantity, ρ is a vector.

form $\rho = \rho(I = 0) + \Delta\rho(I)$: the first term is the ρ distribution in the absence of electromagnetic radiation and $\Delta\rho$ is the perturbation introduced by the beam. For F linear I obtain $\Delta\rho(cI) = c\Delta\rho(I)$, with c an arbitrary real constant: the optical perturbation is proportional to the total beam power P [e.g. photorefractives (42) and thermo-optic media (39)]; otherwise, powers of P with exponent > 1 need to be included (e.g. unbiased nematic liquid crystals, see chapter 2).

After computing ρ, the nonlinear index perturbation is given by $\Delta n(I) = n[\rho(I)] - n(\rho_0)$ where $\rho_0 = \rho(I = 0)$. The relationship $\Delta n = \Delta n(\rho, \rho_0)$ embraces various dependences, from linear (in thermo-optic media) to nonlinear (e.g. sinusoidal in NLC), which can be Taylor-expanded as[1] $\Delta n = \sum_{m=0}^{\infty} (\Delta n_m/m!)\,(\rho - \rho_0)^m$, being $\Delta n = \partial^m \Delta n/\partial x^m|_{I=0}$. A linear relationship between nonlinear perturbation and field intensity occurs only if $\Delta\rho = \Delta\rho(I)$ is linear and $\Delta n \cong \Delta n_1 \Delta\rho$.

I aim at investigating the role of the boundary conditions on $\Delta\rho$ and use the Green formalism to solve for F in some physically relevant cases. To compute Δn I consider a self-trapped Gaussian light-beam (other profiles could be accounted for through an expansion in Hermite polynomials) exciting the nonlinear response of a finite-size medium. In order to describe/quantify the extent of the nonlocality when it is symmetrically-distributed with respect to the beam axis, I introduce the ratios α_i between full-widths at half-maximum (FWHM) of the soliton and of the perturbation along the i-th transverse coordinate ($i = x, t$):

$$\alpha_i = \frac{FWHM_i^{|A|^2}}{FWHM_i^{\Delta n}} \tag{3.3}$$

with FWHM computed along the section $x/t =$ constant and containing the peak of the function.

From eq. (3.3), small α correspond to a large range of nonlocality (30). It is important to note that this definition is more general than the one based on the comparison between the widths of the Green function and of the intensity (32), being the former not always definable, in particular when the Green function diverges at the excitation point, as it occurs for example if F is the Poisson equation in bidimensional geometries. For a Gaussian profile $|A(x,t)|^2 = A_0 \exp\left[-\left(\frac{(x-x_c)^2}{w_x^2} + \frac{(t-t_c)^2}{w_t^2}\right)\right]$ and $FWHM_{x/t}^{|A|^2} =$

[1] I assume that the refractive index in a given point depends only on the value of ρ calculated at the same point.

$2\sqrt{\ln 2} w_{x/t}$; moreover, if I consider $\Delta n \cong \Delta n_1 \Delta\rho$, it is $FWHM^{\Delta n} = FWHM^{\Delta\rho}$. The general case is investigated in appendix C.1.

If the perturbation is asymmetric with respect to its own maximum, I define four ratios as

$$\alpha_{x/t}^{g/s} = \frac{FWHM_{x/t}^{|A|^2}}{2\sigma_{x/t}^{g/s}} \tag{3.4}$$

where $\sigma_{x/t}^{g/s}$ are the separations (along x/t) between the intensity peak and half-peak values, for x/t greater (g) or smaller (s) than the intensity peak position (see figure 3.1).

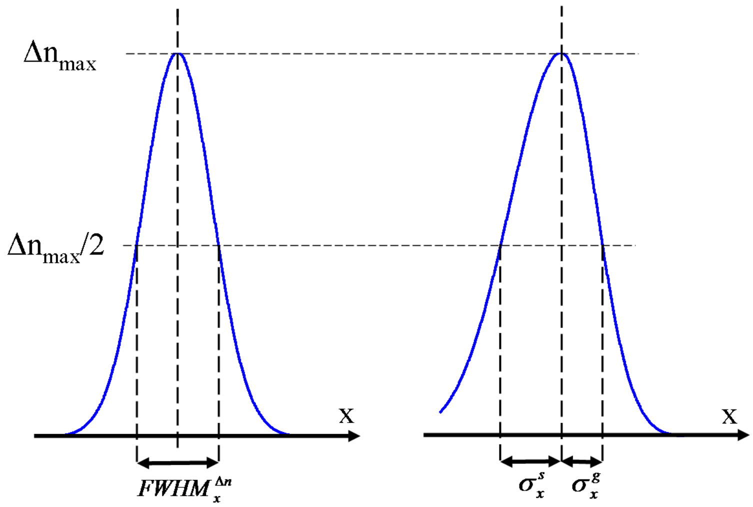

Figure 3.1: Computation of FWHM for the nonlinear index perturbation Δn along x. The blue curves are $\Delta n(x, t = t_{max})$ versus x, where t_{max} is the t coordinate of maximum perturbation. On the left the symmetric case, on the right the asymmetric one. Clearly, superscript g/s depend on the orientation of x axis. The case along t is analogous.

Finally, if F is linear with excitation, the parameters $FWHM_{x/t}^{\Delta\rho}$ and $\sigma_{x/t}^{g/s}$ are power independent. The case when F is nonlinear is addressed in appendix C.1.

3.2 Role of the Boundary Conditions on the Nonlinear Index Perturbation

Hereby I theoretically address four different equations to describe equation F, largely adopted in literature (Poisson equation 1D and 2D, screened Poisson and reorientation equation in NLC in anisotropic configurations), to investigate the effects of the boundary conditions on Δn in rectangular geometries, hence, on the nonlocality perceived by the beam. To perform the computation I use the Green function method (84). The nonlinear index perturbation Δn and $\Delta\rho$ are related as depicted in section 3.1: in the first three cases I consider a linear relationship.

3.2.1 Poisson 1D

First I analyze a 1D problem with F given by the Poisson equation (85; 86):

$$\beta \frac{d^2 \Delta\rho}{dx^2} + |A|^2 = 0 \tag{3.5}$$

with boundary conditions $\Delta\rho(x = 0) = \Delta\rho(x = a) = 0$, being a the sample thickness; I assume that ρ on the sample edges is unchanged by the beam. By defining $\xi = x/a$ and $\kappa = \beta/a^2$, eq. (3.5) takes the normalized form

$$\kappa \frac{d^2 \Delta\rho}{d\xi^2} + |A|^2 = 0 \tag{3.6}$$

with $\Delta\rho(\xi = 0) = \Delta\rho(\xi = 1) = 0$. The corresponding Green function G is given by (84)

$$G(\xi, \zeta) = \frac{\xi}{\kappa}(1 - \zeta)u(\zeta - \xi) + \frac{\zeta}{\kappa}(1 - \xi)u(\xi - \zeta) \tag{3.7}$$

being ζ the application point of a Dirac delta and u the Heaviside function. G depends on ζ because translation invariance is lost due to the boundaries. For an intensity profile $|A(\xi)|^2$, I have $\Delta\rho(\xi) = \int_0^1 |A(\zeta)|^2 G(\xi, \zeta) d\zeta$. If $|A(\xi)|^2 = \exp\left[-\left(\xi - \langle\xi\rangle\right)^2/\omega^2\right]$ (actual waist $w = \omega a$) I get:

$$\begin{cases} \Delta\rho = \dfrac{\omega}{2\kappa}(N_1 + N_2) \\ N_1 = \sqrt{\pi}\left[\mathrm{erf}\left(\dfrac{1-\langle\xi\rangle}{\omega}\right)(1-\langle\xi\rangle)\xi + \mathrm{erf}\left(\dfrac{\xi-\langle\xi\rangle}{\omega}\right)(\langle\xi\rangle - \xi) + \langle\xi\rangle(\xi-1)\mathrm{erf}\left(-\dfrac{\langle\xi\rangle}{\omega}\right)\right] \\ N_2 = \omega\left\{\exp\left(-\dfrac{\langle\xi\rangle^2}{\omega^2}\right) - \exp\left[-\dfrac{(\xi-\langle\xi\rangle)^2}{\omega^2}\right] - \xi\left[\exp\left(-\dfrac{\langle\xi\rangle^2}{\omega^2}\right) - \exp\left[-\dfrac{(1-\langle\xi\rangle)^2}{\omega^2}\right]\right]\right\} \end{cases} \tag{3.8}$$

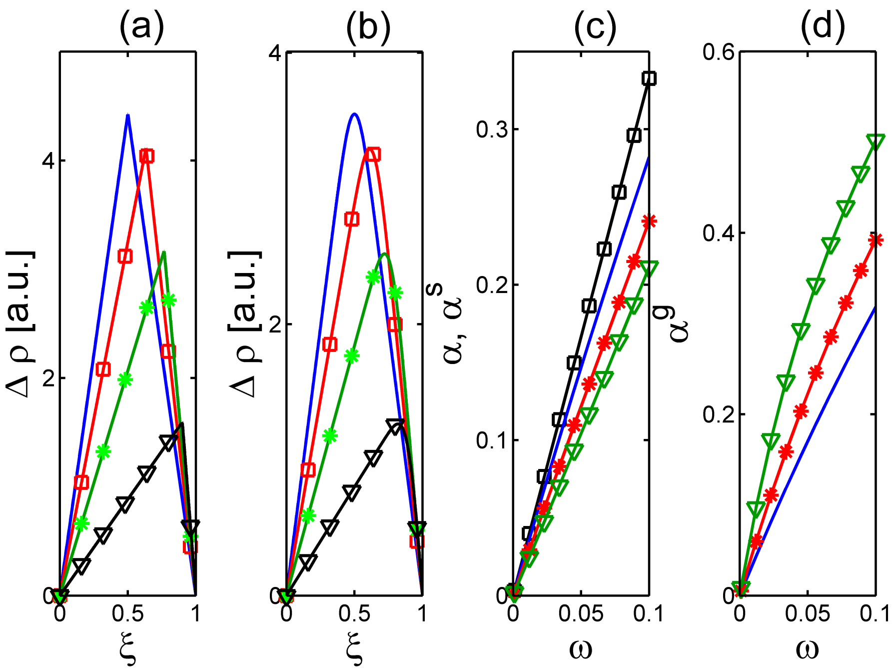

Figure 3.2: (a,b) Perturbation profiles versus ξ for $\langle\xi\rangle = 0.5, 0.63, 0.76$ and 0.9 (solid line, squares, stars and triangles, respectively) for (a) $\omega = 0.001$ and (b) $\omega = 0.09$. The profile in (a) is very similar to the Green function, as the soliton is much narrower than the sample width. (c) Calculated α (squares) and α^s for $\langle\xi\rangle = 0.54$ (no symbols), $\langle\xi\rangle = 0.72$ (stars) and $\langle\xi\rangle = 0.86$ (triangles), respectively, versus normalized waist ω. (d) Calculated α^g for the same set of soliton positions.

Plots of eq. (3.8) are visible in fig. 3.2 for $\beta > 0$ (the latter applies throughout the rest of the chapter). I note that the problem is invariant under the transformation $\xi \to 1 - \xi$. For $\langle\xi\rangle = 0.5$ the perturbation is symmetric with respect to the mid-plane $\xi = 0.5$. In other cases (i.e. beam positions) the perturbation is asymmetric due to the unequal distances between soliton and boundaries: its maximum is shifted relative to the peak of the excitation. Fig. 3.2(c) shows the parameter α_x versus waist ω; the relationship $\alpha^{g/s}[\langle\xi\rangle] = \alpha^{s/g}[1-\langle\xi\rangle]$ holds true, allowing to restrict the analysis to $\langle\xi\rangle > 0.5$. The nonlocality increases as the ratio between beam width and sample thickness decreases. Figs. 3.2(c-d) display $\alpha_x^{g/s}$ versus ω for various beam centers $\langle\xi\rangle$: as the beam moves closer and closer to a boundary, the overall perturbation gets smaller and smaller, with a reduced (increased) extension towards the closest (furthest) edge.

3.2.2 Poisson 2D

I now consider two-dimensional configurations. I start with the Poisson equation in 2D:

$$\beta\nabla^2\Delta\rho(x,t) + |A(x,t)|^2 = 0 \tag{3.9}$$

which is linear with power and governs, for example, nonlinear optical propagation in thermo-optic media (87). I take a sample infinitely wide (thick) along t but finite along x, from 0 to a, with boundary conditions $\Delta\rho(x=0,t) = \Delta\rho(x=a,t) = 0$ and $\lim_{|t|\to\infty}\Delta\rho(x,t) = 0$. By setting $\xi = x/a$, $\upsilon = t/a$ and $\kappa = \beta/a^2$, eq. (3.9) reduces to

$$\kappa\nabla^2_{\xi,\upsilon}\Delta\rho(\xi\upsilon) + |A(\xi,\upsilon)|^2 = 0 \tag{3.10}$$

with the new boundary conditions $\Delta\rho(\xi=0,\upsilon) = \Delta\rho(\xi=1,\upsilon) = 0$ and $\lim_{|\upsilon|\to\infty}\Delta\rho(\xi,\upsilon) = 0$. The solutions for $\Delta\rho$, given a certain intensity profile, is evaluated by

$$\Delta\rho(\xi,\upsilon) = -\int_{-\infty}^{\infty} d\eta \int_0^1 G(\xi,\upsilon,\zeta,\eta)|A(\zeta,\eta)|^2 d\zeta \tag{3.11}$$

where $G(\xi,\upsilon,\zeta,\eta)$ is the Green function for the given geometry, as computed in the next section.

3.2.2.1 Green Function in a Finite Rectangular Geometry

I compute the Green function in a two dimensional geometry infinitely extended along a direction and finite along the other, with Dirichlet boundary conditions. I name ξ and υ the finite and infinite coordinates, respectively, and fix to 1 the cell width along ξ. I have to find the function $G(\xi,\upsilon,\zeta,\eta)$ determined by

$$\nabla^2_{\xi\upsilon} G(\xi, \upsilon, \zeta, \eta) = \delta(\xi - \zeta, \upsilon - \eta) \tag{3.12}$$

$$\begin{cases} G(\xi = 0, \upsilon, \zeta, \eta) = G(\xi = 1, \upsilon, \zeta, \eta) = 0 \\ \lim\limits_{|\upsilon| \to \infty} G(\xi, \upsilon, \zeta, \eta) = 0 \end{cases} \tag{3.13}$$

where $\xi = \zeta$ and $\upsilon = \eta$ are the coordinates of excitation and (3.13) are the boundary conditions. To simplify the computation I introduce a new function F as

$$F = \begin{cases} G(\xi) & \text{if } 0 < \xi < 1, \\ -G(-\xi) & \text{if } -1 < \xi < 0 \end{cases} \tag{3.14}$$

For $|\xi| > 1$ I take $F(\xi) = F(\xi + 2)$; hence, F is a periodic function with period 2 and, from eq. (3.14), F is odd. Developing F in a Fourier series:

$$F(\xi, \upsilon, \zeta, \eta) = \sum_{m=1}^{\infty} b_n(\upsilon, \zeta, \eta) \sin(\pi m \xi) \tag{3.15}$$

The second partial derivatives for F from eq. (3.15) are $\frac{\partial^2 F}{\partial \xi^2} = -\sum_{m=1}^{\infty} b_m (\pi m)^2 \sin(\pi m \xi)$ and $\frac{\partial^2 F}{\partial \upsilon^2} = \sum_{m=1}^{\infty} \frac{\partial^2 b_m}{\partial \upsilon^2} \sin(\pi m \xi)$. Substitution into (3.12) leads to

$$\sum_{m=1}^{\infty} \sin(\pi m \xi) \left[\frac{\partial^2 b_m}{\partial \upsilon^2} - (\pi m)^2 b_m \right] = \delta(\xi - \zeta, \upsilon - \eta) - \delta(\xi + \zeta, \upsilon - \eta) \tag{3.16}$$

where the presence of the second source term is due to the charge image needed to entail the correct boundary conditions on F. Multiplying both sides of eq. (3.16) for $(1/2)\sin(\pi p \xi)$ and integrating over ξ between -1 and 1, for $\forall p \in \mathbb{N}$ I get

$$\frac{\partial^2 b_p}{\partial \upsilon^2} - (\pi p)^2 b_p = 2 \sin(\pi p \zeta) \delta(\upsilon - \eta) \tag{3.17}$$

The solutions are

$$b_p = \begin{cases} A e^{-\pi p(\upsilon - \eta)}, & \upsilon > \eta \\ B e^{\pi p(\upsilon - \eta)}, & \upsilon < \eta \end{cases} \tag{3.18}$$

To find the boundary condition for $\partial b_p / \partial \upsilon$ in $\upsilon = \eta$ I integrate (3.17) over the interval $\eta - \delta < \upsilon < \eta + \delta$, i.e $\int_{\eta-\delta}^{\eta+\delta} \left\{ \frac{\partial^2 b_p}{\partial \upsilon^2} - (\pi p)^2 b_p \right\} d\upsilon = 2 \sin(\pi p \zeta)$. In the limit $\delta \to 0$ and using eq. (3.18), the former relationship becomes $A + B = -\frac{2}{\pi p} \sin(\pi p \zeta)$;

conversely, the continuity of b_p in $\upsilon = \eta$ leads to $A = B$: solving the system I find $A = B = -\frac{1}{\pi p}\sin(\pi p\zeta)$. Putting this result in eq. (3.18) provides $b_p(\upsilon, \zeta, \eta) = -\frac{1}{\pi p}\sin(\pi p\zeta)\, e^{-\pi p|\upsilon-\eta|}$. From eq. (3.15), the sought Green function G is

$$G(\xi, |\upsilon - \eta|, \zeta) = -\sum_{m=1}^{\infty} \frac{1}{\pi m} \sin(\pi m\zeta)\, e^{-(\pi m|\upsilon-\eta|)} \sin(\pi m\xi) \tag{3.19}$$

G depends on $|\upsilon - \eta|$ because of translational symmetry along the υ axis. Furthermore, when $\xi = \zeta$ and $\upsilon = \eta$, i.e. when the response is calculated in the same point of the forcing term, I have $G(\xi = \zeta, 0) = -\sum_{m=1}^{\infty} \frac{1}{\pi m}\sin^2(\pi m\zeta)$, that diverges for $\zeta \neq ha$ $(h = 1, 2, \ldots)$, as espected.

3.2.2.2 Perturbation Profile

As stated above, eq. (3.19) is a diverging harmonic series in $\xi = \zeta, \upsilon = \eta$, and must be inserted into eq. (3.11) to find $\Delta\rho$; to compute the total perturbation from an intensity profile $|A(\zeta, \eta)|^2$, I take the series out of the integral, obtaining:

$$\begin{aligned}\Delta\rho(\xi, \upsilon) &= \int_{-\infty}^{\infty} d\eta \int_0^1 \sum_{m=1}^{\infty} \frac{1}{\pi m} \sin(\pi m\xi)\sin(\pi m\zeta) e^{-\pi m|\upsilon-\eta|}|A(\zeta, \eta)|^2 d\zeta = \\ &= \sum_{m=1}^{\infty} \frac{1}{\pi m} \sin(\pi m\xi) \int_{-\infty}^{\infty} d\eta \int_0^1 \sin(\pi m\zeta) e^{-\pi m|\upsilon-\eta|}|A(\zeta, \eta)|^2 d\zeta\end{aligned} \tag{3.20}$$

Eq. (3.20) is the Fourier series along the axis ξ for the perturbation profile, that is

$$\Delta\rho(\xi, \upsilon) = \sum_{m=1}^{\infty} \frac{1}{\pi m} V_m(\upsilon) \sin(\pi m\xi) \tag{3.21}$$

where the harmonic coefficients $V_m(\upsilon)$ are given by

$$V_m(\upsilon) = \int_{-\infty}^{\infty} d\eta \int_0^1 \sin(\pi m\zeta) e^{-\pi m|\upsilon-\eta|}|A(\zeta, \eta)|^2 d\zeta. \tag{3.22}$$

If the intensity profile is in the form $|A(\xi, \upsilon)|^2 = f_\xi(\xi) f_\upsilon(\upsilon)$ I derive that $V_m(\upsilon) = V_m^\xi V_m^\upsilon(\upsilon)$, being

$$V_m^\xi = \int_0^1 f_\xi(\zeta)\sin(\pi m\zeta) d\zeta \tag{3.23}$$

$$V_m^\upsilon(\upsilon) = \int_{-\infty}^{\infty} f_\upsilon(\eta) e^{-\pi m|\upsilon-\eta|} d\eta \tag{3.24}$$

I note that, if $f_\upsilon(\upsilon)$ has an even parity, V_m^υ and $\Delta\rho$, are even too.
Now I consider an astigmatic Gaussian shape for the intensity with a varying center, i.e. $|A(\xi,\upsilon)|^2 = \exp\left\{-\left[\frac{(\xi-\langle\xi\rangle)^2}{\omega_x^2}+\frac{\upsilon^2}{\omega_t^2}\right]\right\}$, where $\omega_{x/t} = w_{x/t}/a$ and $\langle\xi\rangle$ is the ξ coordinate of the intensity peak[1]. V_m^υ is given by (details are reported in appendix C.2):

$$V_m^\upsilon = \frac{\sqrt{\pi}}{2}\omega_t e^{\left(\frac{\pi m}{2}\right)^2\omega_t^2}\left[\operatorname{erfc}\left(\frac{\upsilon}{\omega_t}+\frac{\pi m}{2}\omega_t\right)e^{\pi m\upsilon}+\operatorname{erfc}\left(-\frac{\upsilon}{\omega_t}+\frac{\pi m}{2}\omega_t\right)e^{-\pi m\upsilon}\right] \quad (3.25)$$

Additionally, if the beam profile is narrow compared to the sample thickness a ($\omega_x << 1$), I obtain (C.3):

$$V_m^\xi(\langle\xi\rangle) \cong \sqrt{\pi}\omega_x \sin(\pi m\langle\xi\rangle)e^{-\pi^2\omega_x^2\left(\frac{m}{2}\right)^2} \quad (3.26)$$

Fig. 3.3(a) displays the results for $V_m^\xi(\langle\xi\rangle)$ for various beam positions and waists (the graph shows the symmetric excitation $\omega_x = \omega_t$, but the generalization is straightforward); it also shows the comparison between numerical results obtained from eq. (3.23) and the formula (3.26). As expected, the index m_{sup}, defined as the value beyond which V_m^ξ become negligible, increases as the beams shrink. Therefore, in order to reach a good approximation, it is necessary to take into account more terms in eq. (3.20).

The calculated nonlocal parameters are graphed in fig. 3.3(b-d), the perturbation profiles are presented in fig. 3.4. Since the symmetry imposes $\alpha_t^g = \alpha_t^s$ and $\alpha_x^g(\langle\xi\rangle) = \alpha_x^s(1-\langle\xi\rangle)$, I limit to the case $\langle\xi\rangle > 0.5$. Due to the boundaries, the nonlocality along t is higher than along x on the beam-side closer to the edge (i.e., $\alpha_t^{g,s} > \alpha_x^g$). As the excitation moves off-axis and the overall perturbation reduces in magnitude, such anisotropy gets larger. Conversely, while for $\langle\xi\rangle = 0.5$ the nonlocality along x is weaker than along t, when $\langle\xi\rangle = 0.68$ and $\langle\xi\rangle = 0.84$ the largest nonlocal perturbation along x exceeds that along t.

3.2.3 Screened Poisson Equation

Another relevant 2D case is the screened Poisson equation:

$$K\nabla^2\Delta\rho + \mu\Delta\rho + |A(x,t)|^2 = 0 \quad (3.27)$$

[1]Given the invariance along t due to the infinite extent, I can consider profiles centered in $\upsilon = 0$ without any loss of generality.

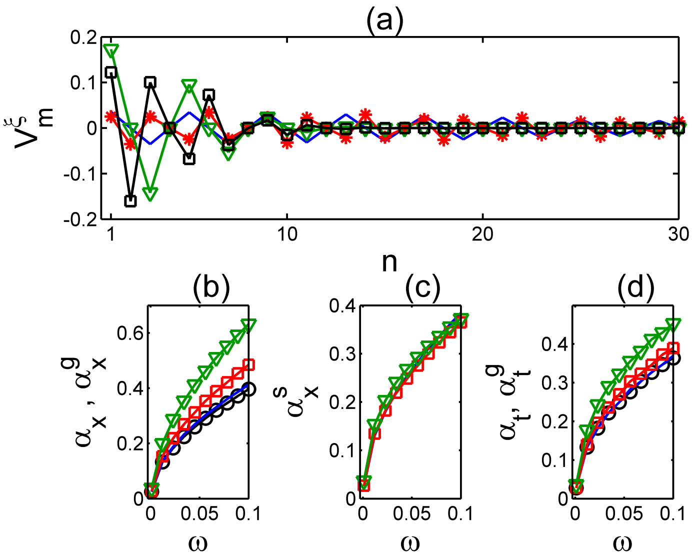

Figure 3.3: Calculated $V_m^\xi(\xi)$ for $\omega = 0.02$ and $\langle\xi\rangle = 0.5$(solid line), $\omega = 0.02$ and $\langle\xi\rangle = 0.75$ (asterisks), $\omega = 0.1$ and $\langle\xi\rangle = 0.5$ (triangles), $\omega = 0.1$ and $\langle\xi\rangle = 0.75$ (squares), respectively. The numerical results are in complete agreement with the theoretical approximation. (b, c) Calculated degree of nonlocality along x and (d) along t for $\langle\xi\rangle = 0.5$ (circles), $\langle\xi\rangle = 0.54$ (solid line), $\langle\xi\rangle = 0.68$ (squares) and $\langle\xi\rangle = 0.81$ (triangles), respectively.

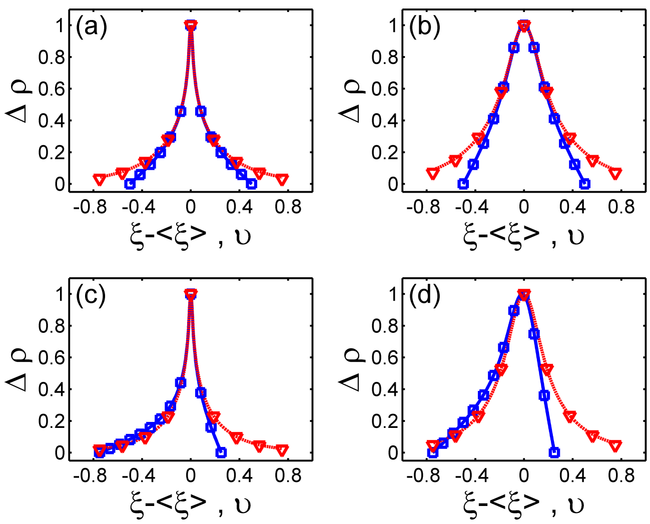

Figure 3.4: Perturbation profiles for (a,c) $\omega = 0.01$ and (b,d) $\omega = 0.1$ for (a,b) $\langle\xi\rangle = 0.5$ and (c,d) $\langle\xi\rangle = 0.75$. The dashed (solid) lines correspond to profiles along $v(\xi - \langle\xi\rangle)$. The profiles are chosen such to contain the perturbation peak. Squares (triangles) are the corresponding values computed with a full numerical approach, which completely agree with the theoretical predictions from eq. (3.20).

with K and $\mu < \frac{K\pi^2}{a^2}$ given constants. Eq. (3.27) governs reorientation in liquid crystals in an isotropic configuration (30) and is largely used as a ruling equation for refractive index in nonlinear nonlocal media (34; 83). I consider the same geometry investigated in section 3.2.2. Using the same normalizations I get

$$\kappa\nabla^2_{\xi\upsilon}\Delta\rho + \mu\Delta\rho + |A(\xi,\upsilon)|^2 = 0 \tag{3.28}$$

In the next section I compute the corresponding Green function, necessary to evaluate the nonlinear perturbation through eq. (3.11).

3.2.3.1 Green Function for the Screened Poisson Equation

To find the Green function G I have to solve

$$\kappa\nabla^2 G + \mu G = \delta(\xi-\zeta,\upsilon-\eta) \tag{3.29}$$

with boundary conditions as in section 3.2.2.1. Developing G in a Fourier series respect to ξ as previously done for the Poisson equation, I can write $\sum_{m=1}^{\infty} b_m(\upsilon,\zeta,\eta)\sin(\pi m\xi)$. Substitution of the latter into eq. (3.31) leads to

$$\sum_{m=1}^{\infty}\left\{\kappa\frac{\partial^2 b_m}{\partial\upsilon^2} + \mu b_m - \kappa b_m\left(\pi m\right)^2\right\}\sin\left(\pi m\xi\right) = \delta(\xi-\zeta,\upsilon-\eta) \tag{3.30}$$

Every coefficient b_m is determined by $\frac{\partial^2 b_m}{\partial\upsilon^2} - \left[(\pi m)^2 - \frac{\mu}{\kappa}\right] b_m = \frac{2}{\kappa}\sin(\pi m\zeta)\delta(\upsilon-\eta)$, which is equal to eq. (3.17) with the transformation $(\pi m)^2 \rightarrow \left[(\pi m)^2 - \frac{\mu}{\kappa}\right]$[1]. From eq. (3.19) it is easy to compute

$$G(\xi,|\upsilon-\eta|,\zeta) = -\sum_{m=1}^{\infty}\frac{1}{\sqrt{(\pi m)^2-\frac{\mu}{\kappa}}}\sin\left(\pi m\zeta\right)e^{-\sqrt{(\pi m)^2-\frac{\mu}{\kappa}}|\upsilon-\eta|}\sin\left(\pi m\xi\right) \tag{3.31}$$

[1]To have a real square root $\forall m$, the relationship $\mu < \frac{K\pi^2}{a^2}$ must hold true, as anticipated in section 3.2.3.

3.2.3.2 Perturbation Profile

Proceeding as already done in section 3.2.2.2 and using the Green function (3.31), for $\Delta\rho$ I get:

$$\Delta\rho(\xi,\upsilon) = \frac{1}{\kappa}\sum_{m=1}^{\infty}\frac{1}{\sqrt{(\pi m)^2-\frac{\mu}{\kappa}}}V_m(\upsilon)\sin(\pi m\xi) \tag{3.32}$$

where

$$V_m(\upsilon) = \int_{-\infty}^{\infty}d\eta\int_0^1 \sin(\pi m\zeta)e^{-\sqrt{(\pi m)^2-\frac{\mu}{\kappa}}|\upsilon-\eta|}|A(\zeta,\eta)|^2 d\zeta \tag{3.33}$$

Setting once again $|A(\xi,\upsilon)|^2 = \exp\left\{-\left[\frac{(\xi-\langle\xi\rangle)^2}{\omega_x^2}+\frac{\upsilon^2}{\omega_t^2}\right]\right\}$, I get $V_m(\upsilon) = V_m^{\xi}V_m^{\upsilon}(\upsilon)$, where V_m^{ξ} is given by (3.26) [(3.23) for other beam shapes], whereas $V_m^{\upsilon}(\upsilon)$ now is

$$V_m^{\upsilon}(\upsilon) = \frac{\sqrt{\pi}}{2}\omega_t e^{\Theta_m\omega_t^2}\left[\operatorname{erfc}\left(\frac{\upsilon}{\omega_t}+\frac{\Theta_m}{2}\omega_t\right)e^{\Theta_m\upsilon}+\operatorname{erfc}\left(-\frac{\upsilon}{\omega_t}+\frac{\Theta_m}{2}\omega_t\right)e^{-\Theta_m\upsilon}\right] \tag{3.34}$$

having defined $\Theta_m = \sqrt{(\pi m)^2-\frac{\mu}{\kappa}}$.

Equation (3.28) has a degree of nonlocality depending on the ratio μ/κ: the nonlocality decreases as μ/κ increases. In fact, for $\mu = 0$ I get the Poisson equation, which is the most nonlocal case, whereas for $\mu/\kappa \to \infty$ it is $\Delta\rho \propto |A|^2$, i.e., the local case. Fig. 3.5 shows the results obtained by substituting eq. (3.31) in eq. (3.11), for $\mu/\kappa = 10^2$ and $\mu/\kappa = 10^4$. Slight differences exists with the Poisson case, as the ratio μ/κ increases up to 1; for large μ/κ, the perturbation becomes radially symmetric, the boundary conditions being the same owing to the large distance from the cell edges.

3.2.4 Reorientational Equation for the NLC in Anisotropic Configuration

I now turn to the NLC in an anisotropic configuration (see chapter 2). As already discussed, in this case F in the reference system xt is:

$$\nabla_{xt}^2\theta + \gamma\sin\left[2(\theta-\delta)\right]|A|^2 = 0 \tag{3.35}$$

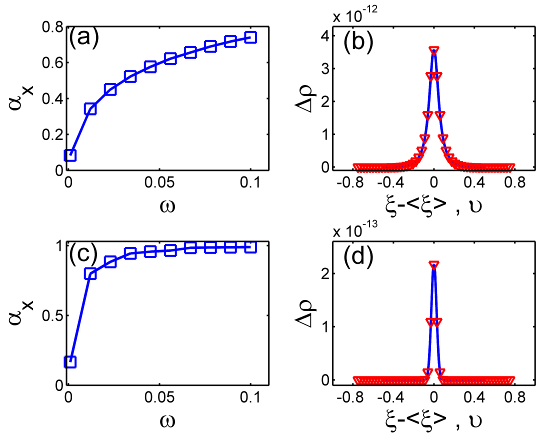

Figure 3.5: Calculated figure of nonlocality α_x for Gaussian intensity profiles (curves for α_t and $\alpha_{x/t}^{g/s}$ are nearly identical) versus ω for $\langle\xi\rangle = 0.5$ and (a,b) $\mu/\kappa = 10^2$ or (c,d) $\mu/\kappa = 10^4$. In this range for μ/κ, the nonlocality does not depend on beam position. When $\alpha_x = 1$, perturbation and excitation have the same profile, i.e. the medium is local. (b) - (d): perturbation profile along υ(symbols) and $\xi - \langle\xi\rangle$(solid line) for $\mu/\kappa = 10^2$ and $\mu/\kappa = 10^4$, respectively, when $\omega = 0.035$ and $\langle\xi\rangle = 0.5$; in both cases the perturbation possesses radial symmetry. In (b) the perturbation is wider due to a higher ratio μ/κ.

where $\gamma = \frac{\epsilon_0\epsilon_a}{4K}$, being K the Frank elastic constant and ϵ_a the optical anisotropy. When no excitation is applied, I suppose that rubbing induces a uniform director distribution, forming an angle θ_0 with respect to the beam wavevector.
The presence of the unknown variable θ into the sine precludes the possibility to use the Green function formalism, being eq. (3.35) nonlinear. However, it is possible to solve eq. (3.35) using a perturbative approach (49), as shown in the next section.

3.2.4.1 Perturbative Approach for the Director Profile Computation

Let me begin by making the positions

$$\begin{cases} |A|^2 = \epsilon V \\ \theta = \theta_0 + \epsilon\theta_1 + \epsilon^2\theta_2 + \ldots = \sum_{n=0}^{\infty} \epsilon^n \theta_n \end{cases} \tag{3.36}$$

where ϵ is a *smallness* parameter which will be set equal to 1 at the end of the derivation.

I define the optical reorientation as

$$\Psi \equiv \theta - \theta_0 = \epsilon\theta_1 + \epsilon^2\theta_2 + \ldots = \sum_{n=1}^{\infty} \epsilon^n \theta_n \tag{3.37}$$

Substituting eq. (3.37) in (3.35) and writing the sine in a power series around $\theta = \theta_0$ provides:

$$\begin{gathered} \nabla^2 \left[\theta_0 + \epsilon\theta_1 + \epsilon^2\theta_2 + o(\epsilon^2)\right] + \gamma \left\{\sin\left[2(\theta_0 - \delta)\right] \right. \\ \left. +2\cos\left[2(\theta_0 - \delta)\right] \left[\epsilon\theta_1 + \epsilon^2\theta_2 + o(\epsilon^2)\right] + o(\Psi^2)\right\} \epsilon V = 0 \end{gathered} \tag{3.38}$$

Equating to zero all the coefficients multiplying the same powers of ϵ in eq. (3.38), I obtain

$$\begin{aligned} &\epsilon^0 : \ \nabla^2\theta_0 = 0 \\ &\epsilon^1 : \ \nabla^2\theta_1 + \gamma \sin\left[2(\theta_0 - \delta)\right] V = 0 \\ &\epsilon^2 : \ \nabla^2\theta_2 + 2\gamma \cos\left[2(\theta_0 - \delta)\right] \theta_1 V = 0 \\ &\vdots \end{aligned} \tag{3.39}$$

All eqs. (3.39) are Poisson-like equation, with forcing terms generally dependent on lower order solutions and excitation V: in other words, the nonlinear equation (3.35) has been transformed in an infinite set of linear Poisson equations, coupled through the respective forcing terms. From the first of (3.39) I get that, at order 0 (i.e. without perturbation)[1], the director distribution does not change. For orders larger than 0, solutions of eq. (3.39) at the cell boundaries must be zero.
Being linear equations, they can be solved by the Green function technique as discussed in the former sections; hence, the solutions of (3.39) are

$$\begin{aligned} \theta_1(x,t) &= -\gamma \sin[2(\theta_0 - \delta)] \iint G(x,t,\zeta,\eta) V(\zeta,\eta) d\zeta d\eta \\ \theta_2(x,t) &= -2\gamma \cos[2(\theta_0 - \delta)] \iint G(x,t,\zeta,\eta) V(\zeta,\eta) \theta_1(\zeta,\eta) d\zeta d\eta \\ &= \gamma^2 \sin[4(\theta_0 - \delta)] \iint G(x,t,\zeta,\eta) V(\zeta,\eta) \left\{ \iint G(\zeta,\eta,\zeta',\eta') V(\zeta',\eta') d\zeta' d\eta' \right\} d\zeta d\eta \\ &\vdots \end{aligned} \tag{3.40}$$

[1]This is not more true if the unperturbed θ takes different values at the boundaries.

Setting $\epsilon = 1$ and considering terms up to the second order I get

$$\begin{aligned}
&\theta_1(x,t) = -\gamma \sin[2(\theta_0 - \delta)] \iint G(x,t,\zeta,\eta)|A(\zeta,\eta)|^2 d\zeta d\eta \\
&\theta_2(x,t) = \gamma^2 \sin[4(\theta_0 - \delta)] \iint G(x,t,\zeta,\eta)|A(\zeta,\eta)|^2 \left\{ \iint G(\zeta,\eta,\zeta',\eta')|A(\zeta',\eta')|^2 d\zeta' d\eta' \right\} d\zeta d\eta \\
&\theta(x,t) \cong \theta_0 + \theta_1 + \theta_2
\end{aligned} \tag{3.41}$$

Defining a normalized intensity profile as $|A|^2 = Pf(x,t)$ being $\frac{1}{2Z} \iint f(x,t)dxdt = 1$, with P the beam power and Z the medium impedance, finally I get for θ

$$\theta = \theta_0 + \gamma P g_1(x,t) + \gamma^2 P^2 g_2(x,t) \tag{3.42}$$

having introduced

$$\begin{cases}
g_1(x,t) = -\sin[2(\theta_0 - \delta)] \iint G(x,t,\zeta,\eta) f(\zeta,\eta) d\zeta d\eta \\
g_2(x,t) = \sin[4(\theta_0 - \delta)] \iint G(x,t,\zeta,\eta) f(\zeta,\eta) \left\{ \iint G(\zeta,\eta,\zeta',\eta') f(\zeta',\eta') d\zeta' d\eta' \right\} d\zeta d\eta
\end{cases} \tag{3.43}$$

Eq. (3.42), combined with eq. (3.43), is the solutions of eq. (3.35) for small powers. As it is obvious from the previous analysis, I can get the expression of θ in a *power series* with respect to beam power P, where for every added term I have to solve an additional Poisson equation. As it will be demonstrated below, for typical powers ($P \leq 5mW$), considering terms up to P^2 as in eq. (3.42) provides a very good approximation in undoped liquid crystals.

3.2.4.2 Solution in a Finite Rectangular Geometry

In the case of the rectangular geometry already studied in sections 3.2.2-3.2.3, eq. (3.35) turns into

$$\nabla^2_{\xi\upsilon}\theta + \gamma_N \sin\left[2(\theta - \delta)\right] |A|^2 = 0 \tag{3.44}$$

with the same coordinate transformations used in the above cited cases and where $\gamma_N = \gamma a^2$. Owing to the adopted geometry, the Green function to be used in eq. (3.43) is given by (3.19). So $g_1 = \sin[2(\theta_0 - \delta)] \sum_{m=1}^{\infty} \frac{1}{\pi m} V_m(\upsilon) \sin(\pi m \xi)$ where for $V_m(\upsilon)$ the equations derived above keep their validity. If the excitation field $|A|^2$ is not the product of two functions, both of them dependent only from one transverse variable, I have to compute $g_2(\xi, \upsilon)$ through the general expressions (3.21) and (3.22), with forcing term $|A|^2\theta_1$ [see eq. (3.43)]. In the opposite case, i.e. when $|A(\xi, \upsilon)|^2 = f_\xi(\xi) f_\upsilon(\upsilon)$, I have

$$|A(\xi, \upsilon)|^2 \theta_1(\xi, \upsilon) = \sum_{l=0}^{\infty} A_l(\xi) B_l(\upsilon) \tag{3.45}$$

being $A_l(\xi) = \frac{1}{\pi l} f_\xi(\xi) V_l^\xi \sin(\pi l \xi)$ and $B_l(\upsilon) = f_\upsilon(\upsilon) V_l^\upsilon(\upsilon)$. It is easy to demonstrate that

$$g_2(\xi, \upsilon) = \sin[4(\theta_0 - \delta)] \sum_{m=0}^{\infty} \frac{1}{\pi m} \sin(\pi m \xi) \sum_{l=0}^{\infty} G_l^m F_l^m(\upsilon) \tag{3.46}$$

having defined

$$F_l^m(\upsilon) = \int_{-\infty}^{\infty} B_l(\eta) e^{-\pi m |(\upsilon - \eta)|} d\eta \tag{3.47}$$

$$G_l^m = \int_0^1 \sin(\pi m \zeta) A_l(\zeta) d\zeta \tag{3.48}$$

Equation (3.48) is formally identical to eq. (3.23) and can be computed by means of eq. (C.13), as demonstrated in C.3. Equation (3.47) has no analytical expression, even in the Gaussian case, so I must evaluate them numerically. Computed g_1 and g_2 for Gaussian profiles with $\langle\xi\rangle = 0.5$ and $\langle\xi\rangle = 0.75$ are shown in fig. 3.6 and fig. 3.7, respectively: the two functions possess the same shape with very good approximation, i.e. $g_2(\xi, \upsilon) \cong c g_1(\xi, \upsilon)$. This means that the reorientation angle in NLC and the solutions of Poisson equation behave nearly the same for $\omega << 1$[1]. As a direct consequence, the amount of nonlocality does not depend on beam power if, to describe θ, I need to use only terms up to P^2 (see appendix C.1). Noteworthy, for $\xi = 0.5$, g_1 is cylindrically symmetric around the cell center in an area wider than the beam.

I now compare the results for Gaussian beams, obtained through eq. (3.42) and a full numerical approach based upon a Gauss-Seidel relaxation scheme: such comparison

[1]Of course this result is valid in a rectangular geometry infinitely extended in one dimension.

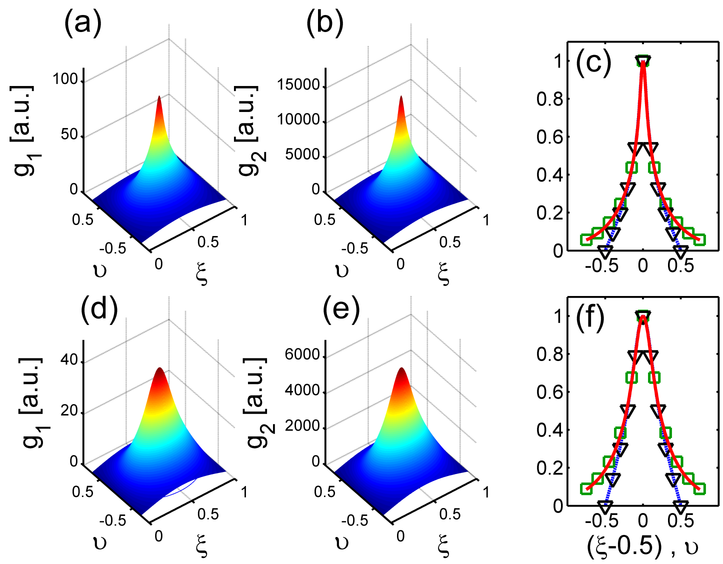

Figure 3.6: Plots of g_1 (a,d) and g_2 (b,e) for $\langle \xi \rangle = 0.5$. The corresponding profiles are plotted in (c) and (f) versus ξ (g_1 solid line, g_2 squares) and υ (g_1 dashed line, g_2 triangles), normalized to one (the cross sections are in $\upsilon = 0$ and $\xi = 0.5$, respectively). Results for g_1 and g_2 perfectly overlap. Excitation waists are $\omega = 0.03$ (a,b,c) and $\omega = 0.1$ (d,e,f), respectively.

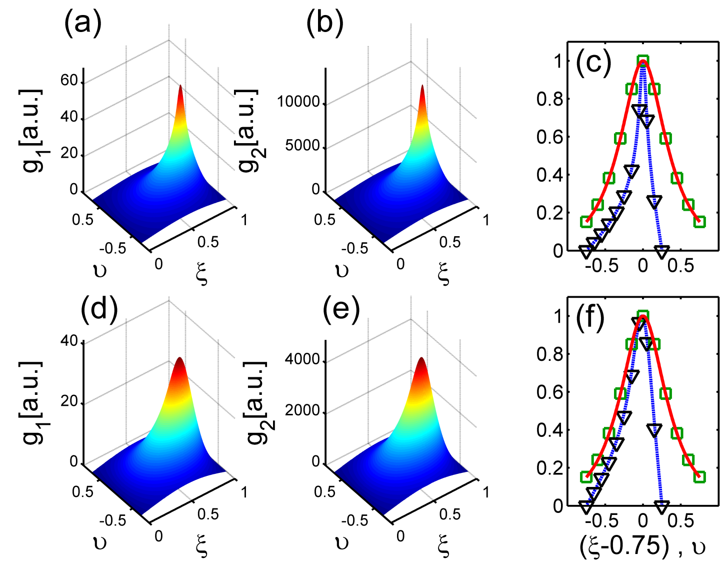

Figure 3.7: As in fig. 3.6, but for $\langle \xi \rangle = 0.75$.

is shown in fig. 3.8. All the simulations are run for a cell width $a = 100\mu m$, an initial director angle $\theta_0 = \pi/6$ and a coefficient γ correspondent to NLC E7. In the numerical algorithm, the boundary conditions along υ are imposed by fixing the perturbation to 0 at a finite distance, chosen such that θ close to the excitation undergoes negligible variations when this distance is increased.

I define θ_{max} as the maximum reorientation angle, fixed an excitation field. Figs. 3.8(a) and 3.8(b) report θ_{max} versus beam power P, for two different beam positions. In both cases a good approximation is reached using only linear term in P up to $P = 2mW$, i.e., a linear relationship between θ and the intensity. For powers up to $4mW$ I need accounting also for the term proportional to P^2. Fig. 3.8(c) shows the behavior of θ_{max} for two different powers, furnishing the magnitude order of the nonlinearly induced perturbation, as the beam is moved across the cell from the center ($\langle\xi\rangle = 0.5$) to the edge ($\langle\xi\rangle = 1$). As predictable, the perturbation diminishes as the beam gets closer to the boundary, the anchoring effects becoming stronger. Finally, fig. 3.8(d) shows the absolute and relative error for $P = 4mW$, defined as $|\theta_{num} - \theta_{theory}|$ and $|\theta_{num} - \theta_{theory}|/|\theta_{num}|$, respectively, where θ_{num} (θ_{theory}) is the distribution angle numerically calculated (theoretically, for terms up to P^2). It is evident that the differences between the two approaches are larger when $|\upsilon|$ is larger, due to the boundary conditions along the infinite dimension in the numerical code. However, the maximum relative error is less than 0.6%, proving a good agreement between the two methods.

3.2.5 Highly Nonlocal Limit for the 2D Case

Let me consider a $\Delta\rho$ given by eq. (3.21) and $V_m(\upsilon)$ by eqs. (3.25) and (3.26). The n-th derivative along ξ is $\frac{\partial^n \Delta\rho}{\partial \xi^n} = \sum_{m=1}^{\infty} \frac{1}{\pi m} V_m^{\xi} V_m(\upsilon) \frac{\partial^n[\sin(\pi m \xi)]}{\partial \xi^n}$. Therefore, for $n = 2$ I get:

$$\frac{\partial^2 \Delta\rho}{\partial \xi^2} = -\sum_{m=1}^{\infty} \pi m V_m^{\xi} V_m^{\upsilon}(\upsilon) \sin(\pi m \xi) \tag{3.49}$$

Similarly, the second derivative along υ is:

$$\frac{\partial^2 \Delta\rho}{\partial \upsilon^2} = \sum_{m=1}^{\infty} \frac{1}{\pi m} V_m^{\xi} \frac{d^2 V_m^{\upsilon}(\upsilon)}{d\upsilon^2} \sin(\pi m \xi) \tag{3.50}$$

In the Poisson 2D case and for a Gaussian shape, eqs. (3.25) holds valid: deriving it I obtain

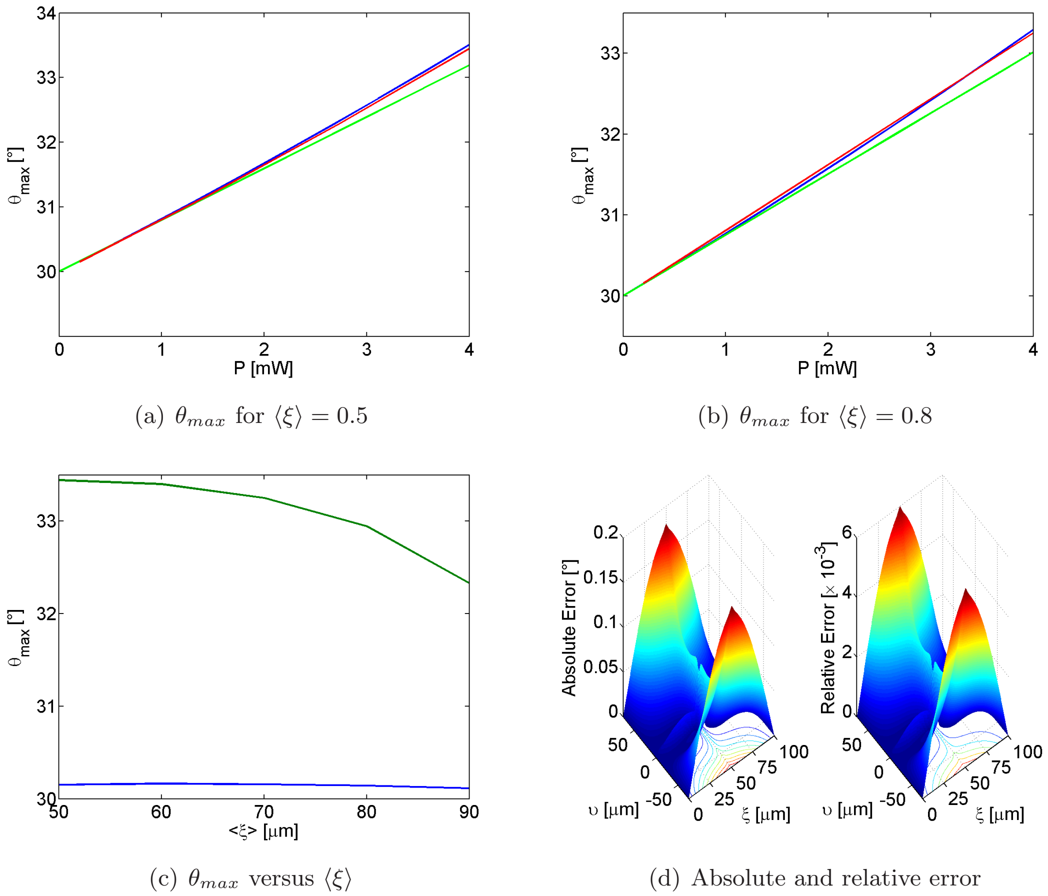

Figure 3.8: Fig. 3.8(a) and 3.8(b) show the maximum reorientation angle θ_{max} versus beam power for $\langle\xi\rangle = 0.5$ and $\langle\xi\rangle = 0.8$, respectively. Green and blue curves represent the solutions taking into account terms up to P and P^2, respectively, whereas the red curve is the full numerical solutions. Fig. 3.8(c) reports θ_{max} versus beam position $\langle\xi\rangle$, for $P = 0.2mW$ (blue line) and $P = 4mW$ (green line). Fig. 3.8(d) shows the absolute (in degrees) and relative errors between theoretical and numerical results, for $P = 4mW$. In all figures $a = 100\mu m$, $w = 2.8\mu m$ and $\theta_0 = \pi/6$.

$$\frac{d^2V_m^\upsilon}{d\upsilon^2}=\frac{\omega_t\sqrt{\pi}}{2}e^{\left(\frac{\pi m}{2}\right)^2\omega_t^2}\left\{e^{\pi m\upsilon}\left[(\pi m)^2\mathrm{erfc}\left(\frac{\upsilon}{\omega_t}+\frac{\pi m}{2}\omega_t\right)+\frac{4}{\sqrt{\pi}\omega_t^2}\left(\frac{\upsilon}{\omega_t}-\frac{\pi m}{2}\omega_t\right)e^{-\left(\frac{\upsilon}{\omega_t}+\frac{\pi m}{2}\omega_t\right)^2}\right]\right.$$
$$\left.+e^{-\pi m\upsilon}\left[(\pi m)^2\mathrm{erfc}\left(-\frac{\upsilon}{\omega_t}+\frac{\pi m}{2}\omega_t\right)-\frac{4}{\sqrt{\pi}\omega_t^2}\left(\frac{\upsilon}{\omega_t}+\frac{\pi m}{2}\omega_t\right)e^{-\left(\frac{\upsilon}{\omega_t}-\frac{\pi m}{2}\omega_t\right)^2}\right]\right\} \tag{3.51}$$

In $\upsilon=0$ I get

$$\frac{d^2V_m^\upsilon}{d\upsilon^2}=\omega_t\sqrt{\pi}e^{\left(\frac{\pi m}{2}\right)^2\omega_t^2}\left[(\pi m)^2\mathrm{erfc}\left(\frac{\pi m}{2}\omega_t\right)-2\frac{\sqrt{\pi}m}{\omega_t}e^{-\left(\frac{\pi m}{2}\right)^2\omega_t^2}\right] \tag{3.52}$$

Substituting eq. (3.52) into (3.50) and setting $\xi=0.5$ I obtain

$$\left.\frac{\partial^2\Delta\rho}{\partial\upsilon^2}\right|_{\xi=0.5,\upsilon=0}=\sum_{m=1}^{\infty}\frac{\omega_t}{\sqrt{\pi}m}V_m^\xi e^{\left(\frac{\pi m}{2}\right)^2\omega_t^2}\left[(\pi m)^2\mathrm{erfc}\left(\frac{\pi m}{2}\omega_t\right)-2\frac{\sqrt{\pi}m}{\omega_t}e^{-\left(\frac{\pi m}{2}\right)^2\omega_t^2}\right]\sin\left(\frac{\pi m}{2}\right) \tag{3.53}$$

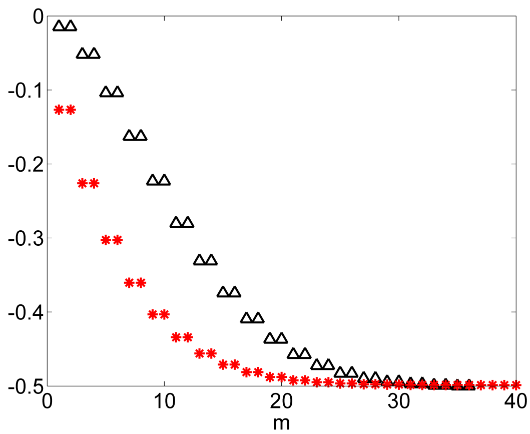

Figure 3.9: Plot of $\frac{\partial^2\Delta\rho}{\partial\xi^2}$ (triangles) and $\frac{\partial^2\Delta\rho}{\partial\upsilon^2}$ (stars), computed in $\xi=0.5,\upsilon=0$ versus integer index m.

Fig. 3.9 shows the results computed from eqs. (3.53) and (3.49), evaluated in $\xi=0.5,\upsilon=0$: the two derivatives are equal, theoretically confirming that the index well perceived by the beams in the highly nonlocal limit is symmetric in the plane $\xi\upsilon$, as previously discussed. Furthermore, the sum of the two series approaches 0.5, as expected from the method in section 2.5.1.1[1].

I demonstrated such property for the simple and screened Poisson equations, but it is easy to understand that this remains valid also for liquid crystals, being $g_1 = g_2$ (see section 3.2.4.2).

[1] Using the same notations it is $\Delta\rho_2 = 0.25$.

3.3 Soliton Trajectory

3.3.1 General Expression for the Equivalent Force

I begin by considering a beam propagation described by a generalized nonlinear Schröedinger equation

$$2ik\frac{\partial A}{\partial s} + \nabla_{\perp}^2 A + 2n_0k_0^2\Delta n(|A|)A = 0 \tag{3.54}$$

To investigate the behavior of the soliton center I can apply the Ehrenfest's theorem to eq. (3.54) (49). I get

$$m\frac{d^2\langle \mathbf{r}\rangle}{ds^2} = m\frac{d^2\left(\iint |\psi|^2\, \mathbf{r} dxdt\right)}{ds^2} = -\iint |\psi|^2\, \nabla V dxdt \tag{3.55}$$

where I set $m = k$, $V = -\left(\frac{k_0^2}{m}\right)n_0\Delta n$ and $\psi = \frac{A}{\sqrt{\iint |A|^2 dxdt}}$ so that $\iint |\psi|^2 dxdt = 1$. If $V(x,t,s) = V_1(x,s) + V_2(t,s)$ from eq. (3.55) I obtain for the x-component of $\mathbf{r}$ (the behavior of t is analogous)

$$k\frac{d^2\langle x\rangle}{ds^2} = -\int \varphi(x)\frac{\partial V_1}{\partial x}dx \tag{3.56}$$

where

$$\varphi(x) = \int |\psi(x,t)|^2 dt \tag{3.57}$$

If I consider a 1D problem, i.e. only one transverse coordinate, eq. (3.56) can be directly obtained from the Ehrenfest's theorem. Eq. (3.56) is valid also if the field, i.e. ψ, is in the form $|\psi|^2 = X(x)T(t)$. It provides

$$\begin{aligned} m\frac{d^2\langle x\rangle}{ds^2} &= -\int dx \int X(x)T(t)\frac{\partial V(x,t,s)}{\partial x}dt = \\ &= -\int X(x)\left\{\int T(t)\frac{\partial V(x,t,s)}{\partial x}dt\right\}dx = \\ &= -\int X(x)\frac{\partial V_{eq}(x,s)}{\partial x}dx \end{aligned} \tag{3.58}$$

where I defined $V_{eq}(x,s,\langle x\rangle) = \int T(t)V(x,t,s)dt$ as a 1D equivalent potential. The last case includes, for example, Gaussian shapes corresponding to soliton profiles in highly nonlocal media (31).

In the rest of the chapter I will refer to V_{eq}, implying that all the results maintain their validity also for V_1. In eq. (3.58) I use $X(x) = \eta_s(x - \langle x \rangle)$ and $F(x, s) = -\partial V_{eq}/\partial x$. The subscript s on η indicates that, in general, the exact form of the beam depends on s (for example breathers). Therefore F is the local force, i.e. the derivative of the potential with inverted sign. It is possible to define a force acting on the beam center and given by

$$F_X^m(\langle x \rangle, s) \equiv \int F(x, s)\eta_s(x - \langle x \rangle)dx \tag{3.59}$$

In the general case the shape of F depends on the value of $\langle x \rangle$, e.g. when the boundary conditions at a finite distance affect the nonlinear response. I can write $F(x, s) = G_s(x - \langle x \rangle, \langle x \rangle)$, where the subscript s indicates the dependence of G from the shape of η. Substituting the latter in eq. (3.59) I obtain $F_X^m(\langle x \rangle, s) = \int G_s(x - \langle x \rangle, \langle x \rangle)\eta_s(x - \langle x \rangle)dx$. If I assume $G_s(x - \langle x \rangle, \langle x \rangle) = G_s(x - \langle x \rangle)$, i.e. the potential shape remains unchanged when the beam center is moved, the only effect is to translate the potential by $\langle x \rangle$; hence, I get $F_X^m(\langle x \rangle, s) = \int G_s(x - \langle x \rangle)\eta_s(x - \langle x \rangle)dx = \int G_s(y)\eta_s(y)dy = F_x^m(s)$: the force does not depend on beam position. The dependence on s is due to the variations in beam profile during propagation (for example a waist varying with s). The beam trajectory can be evaluated by eq. (3.56):

$$\langle x \rangle (s) = \frac{1}{m}\left\{ \int_{s_0}^{s'} \int_{s_0}^{s''} F_X^m(s')ds'ds'' + \left.\frac{d\langle x \rangle}{ds}\right|_{s=s_0} (s - s_0) + \langle x \rangle (s_0) \right\}$$

i.e. a parabolic trajectory for the beam when F_X^m is constant.

If $\eta_s(y)$ is even and $G_s(y)$ is odd, i.e. the potential is even, then $F_X^m = 0$. The beam propagates along a straight line with a slope dependent on its initial velocity, i.e. its initial phase front. If the velocity at the beginning is null, the beam center does not move along the propagation. Physical systems matching these hypotheses are infinitely extended highly nonlocal media featuring $V_1 = k(P)(x - \langle x \rangle)^2$, where Gaussian-shaped solitons exist. Another example is an infinitely extended 1D Kerr medium where $V_1 = k\eta(x - \langle x \rangle)$.

Now I turn back to the general case. Developing G_s in power series around the point

$x = \langle x \rangle$,

$$G_S(x - \langle x \rangle, \langle x \rangle) = W_0(\langle x \rangle) + W_1(\langle x \rangle)(x - \langle x \rangle) + W_2(\langle x \rangle)(x - \langle x \rangle)^2 + \dots = \sum_{n=0}^{\infty} W_n(\langle x \rangle)(x - \langle x \rangle)^n \tag{3.60}$$

where

$$\begin{aligned} W_0 &= G_s|_{x=\langle x \rangle} = - \left.\frac{\partial V_{eq}}{\partial x}\right|_{x=\langle x \rangle} \\ W_n &= \frac{1}{n!} \left.\frac{\partial^n G_s}{\partial (x - \langle x \rangle)^n}\right|_{x=\langle x \rangle} = - \frac{1}{n!} \left.\frac{\partial^{n+1} V_{eq}}{\partial x^{n+1}}\right|_{x=\langle x \rangle}, \quad n = 1, 2, \dots \end{aligned} \tag{3.61}$$

I want to underline how the variables W_i are in general dependent from s in two ways: dependence of $\langle x \rangle$ (i.e. the position of V_{eq}) from s and dependence of V_{eq} shape from the variation in beam profile along s. Force F_X^m is found to be (remembering $\int \eta_s(y)dy = 1$)

$$\begin{aligned} F_X^m &= \int \eta_s(x - \langle x \rangle) \left[W_0(\langle x \rangle) + W_1(\langle x \rangle)(x - \langle x \rangle) + W_2(\langle x \rangle)(x - \langle x \rangle)^2 + \dots \right] dx = \\ &= W_0(\langle x \rangle) + W_1(\langle x \rangle) \int \eta_s(y) y dy + W_2(\langle x \rangle) \int \eta_s(y) y^2 dy + \dots = \\ &= W_0(\langle x \rangle) + \sum_{n=1}^{\infty} W_n(\langle x \rangle) \int \eta_s(y) y^n dy \end{aligned}$$

The final result for F_X^m is

$$F_X^m(s) = \sum_{n=0}^{\infty} W_n(\langle x \rangle) \langle y^n \rangle_\eta \tag{3.62}$$

being $\langle y^n \rangle_\eta = \int y^n \eta(y) dy$.

Eq. (3.62) together with eqs. (3.58) and (3.59) rule the beam trajectory in nonlinear media where the optical propagation is governed by the NNLSE, regardless the specific nonlinear index perturbation $\Delta n(|A|)$. The force F_X^m changes with s due to two reasons: variations in V_{eq} through W_n and variations in intensity through $\langle y^n \rangle$ terms. Interestingly, eq. (3.62) describes the beam motion even in inhomogeneous linear media, i.e. when the index profile Δn does not depend on beam intensity. The term corresponding to $n = 1$ is always zero for the definition of $\langle x \rangle$. Finally, if $\eta(y)$ is even, all the odd terms in eq. (3.62) are zero, being $\left\langle y^{2j+1} \right\rangle = 0\ \forall j \in \mathbb{N}$, independently from V_{eq}, i.e. in every medium.

3.3.2 Power series for the Equivalent Force

In general, $W_n = \sum_{l=0}^{\infty} c_n^l \left(\langle x \rangle - x_0\right)^l$ can be written using a Taylor expansion around $\langle x \rangle = x_0$, where x_0 is the initial beam position, Substituting in eq. (3.62) I get

$$F_X^m(\langle x \rangle) = \sum_{n=0}^{\infty} \sum_{l=0}^{\infty} c_n^l \left(\langle x \rangle - x_0\right)^l \langle y^n \rangle_\eta \tag{3.63}$$

Without loss of generality I can set $x_0 = 0$. If the problem is invariant under the transformation $x \to -x$ (reflection with respect to the plane $x = 0$), the force on the beam must be odd; this implies $c_n^{2l} = 0$ ($l = 0, 1, 2, \ldots$). Inserting the last in eq. (3.63) I get $F_X^m(\langle x \rangle) = \sum_{n=0}^{\infty} \sum_{l=0}^{\infty} c_n^{2l+1} \langle x \rangle^{2l+1} \langle y^n \rangle_\eta$. The beam undergoes an equivalent potential

$$V_X^m(\langle x \rangle, s) = -\int_0^{\langle x \rangle} F_X^m(x', s) dx' = -\sum_{n=0}^{\infty} \sum_{l=0}^{\infty} \frac{1}{(2l+2)} c_n^{2l+1} \langle x \rangle^{2l+2} \langle y^n \rangle_\eta \tag{3.64}$$

For small displacements from $x = 0$ in (3.64), x powers larger than 2 can be neglected; hence, the potential V_X^m takes the form

$$V_X^m(\langle x \rangle, s) = -\frac{1}{2} \left(\sum_{n=0}^{\infty} c_n^1 \langle y^n \rangle_\eta \right) \langle x \rangle^2 \tag{3.65}$$

Eq. (3.65) tells me that for small amplitude motions the beam is subjected to a classical harmonic oscillator potential, with an equivalent *spring constant* $K = \sum_{n=0}^{\infty} c_n^1 \langle y^n \rangle_\eta$ dependent on s. The quantity K depends on beam profile momenta $\langle y \rangle_\eta$, that remain unchanged in soliton propagation: in the latter case K varies with s only through the coefficients c_n^l.

3.3.3 Highly Nonlocal Case

Let me change prospective and consider an infinitely narrow beam, i.e. $\eta(y) = \delta(x - \langle x \rangle)$. From eq. (3.62) I obtain

$$F_X^m = W_0(\langle x \rangle) \tag{3.66}$$

Physically, beams much narrower than the width of the nonlinear response, i.e. in the highly nonlocal regime, are affected only by the derivative of the nonlinear index profile computed on the beam center. I stress how eq. (3.66) keeps its validity whenever W_n terms for $n \geq 2$ are negligible with respect to W_0.
I can apply eq. (3.65) under hypotheses employed for its derivation (see 3.3.2); potential is then given by

$$V_X^m(\langle x \rangle, s) = -\frac{1}{2} c_0^1 \langle x \rangle^2 \tag{3.67}$$

When c_0^1 is constant along s, the potential exerted on the beam does not change with $\langle y \rangle^n$, i.e. the beam width does not affect its trajectory. Thus, the beam moves along a sinusoidal trajectory around $x = 0$, with an amplitude determined by initial conditions and a period $\Lambda = 2\pi\sqrt{\frac{k}{c_0^1}}$.

3.4 Soliton Oscillations in a Finite-Size Geometry

In this section I apply the theory developed in the latter section to investigate beam motion in nonlocal media of finite size. I will focus on the four cases presented in section 3.2, considering Gaussian shapes and their evolution in the presence of an equivalent force given by eq. (3.66) due to the different distance from boundaries. Such results will be confirmed by numerical simulations based on the NNLSE, and by experiments in NLC.

3.4.1 Poisson 1D

Applying eqs. (3.56), (3.66) and (3.61) to the nonlinear index perturbation (3.8) in the normalized transverse unit $\xi = x/a$ and considering $|A|^2 = Ce^{-\xi^2/\omega^2}$ with $C = \frac{k_0^2 2 P_L Z_0}{\sqrt{\pi}\omega a \beta n_0}$

(i.e. a 1D Gaussian beam with power density P_L per unit wavefront), I get:

$$W_0 = C\left\{\left[\mathrm{erf}\left(1-\frac{\langle\xi\rangle}{\omega}\right)+\langle\xi\rangle\left[\mathrm{erf}\left(-\frac{\langle\xi\rangle}{\omega}\right)-\mathrm{erf}\left(1-\frac{\langle\xi\rangle}{\omega}\right)\right]\right]-\frac{\omega}{\sqrt{\pi}}\left[e^{-\frac{\langle\xi\rangle^2}{\omega^2}}-e^{-\frac{(1-\langle\xi\rangle)^2}{\omega^2}}\right]\right\} \tag{3.68}$$

From eq. (3.68) the equivalent force behaves like $1/a$, i.e. increases as the cell thickness decreases. Noteworthy, it is $W_0(0.5-\langle\xi\rangle) = -W_0(0.5+\langle\xi\rangle)$, in agreement with symmetry. Fig. 3.10(a) plots W_0 versus $\langle\xi\rangle$, showing a linear trend for the force and, thus, an effective potential which is harmonic. The propagating soliton undergoes sinusoidal oscillations with period independent from the initial position ($\langle\xi\rangle$ in $s=0$), in agreement with Ref. (85). Moreover, since the force acting on the beam does not depend on its waist, the soliton trajectory is determined by the power but not by the waist [the latter periodically varying along s in the case of breathers (51)]. Finally, since W_0 is linear with P_L, the oscillation period evolves with the square root of the power density [Fig. 3.10(b)]. Numerical (1+1)D simulations of the corresponding NNLSE equation confirm the theoretical findings: the beam trajectories depend only on P_L, but not on beam waist: therefore, all the self-confined waves with equal power feature the same motion in the plane ξs. Fig. 3.10(c-d) shows a typical numerical results for breather excitation, whereas fig. 3.10(b) shows the comparison between numerical and theoretical oscillation period Λ, demonstrating a perfect agreement.

3.4.2 Poisson and Screened Poisson 2D

Let me consider two 2D cases: Poisson and screened Poisson equations. The nonlinear perturbation is ruled by eqs. (3.10) or (3.28), respectively, and the equivalent potential V_{eq} (defined in section 3.3.1) is expressed by:

$$V_{eq}(\langle\xi\rangle) = \sum_{m=1}^{\infty}\frac{1}{\Theta_m}V_m^{\xi}V_m^{\upsilon}\sin(\pi m\xi) \tag{3.69}$$

with $V_m^{\upsilon} = \int_{-\infty}^{\infty} V_m^{\upsilon}(\upsilon)f_{\upsilon}(\upsilon)d\upsilon / \int_{-\infty}^{\infty} f_{\upsilon}(\upsilon)d\upsilon$ [1].

For a Gaussian beam eq. (3.26) holds, whereas from eq. (3.25) V_m^{υ} is (see appendix

[1]The denominator is required to normalize the wavefunction.

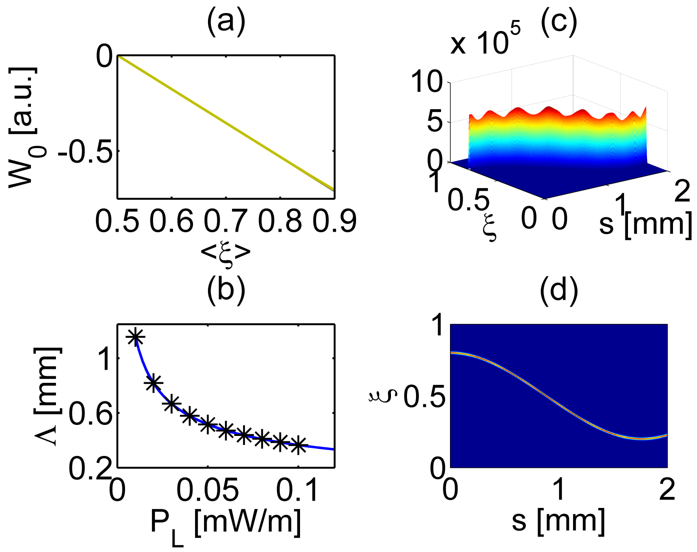

Figure 3.10: (a) Force W_0 acting on soliton versus beam position $\langle\xi\rangle$. Such curve is independent from the beam waist up to $\omega = 0.1$. (b) Oscillation period Λ versus density power P_L computed theoretically (solid line) and numerically (symbols), for $\beta = 10^6$, $a = 100\mu m$ and initial position $\langle\xi\rangle\,(s = 0) = 0.6$ (numerical period for other launching positions differs for less than 1%): such behavior is proportional to $P^{-1/2}$ due to the linear relationship between nonlinear perturbation and field intensity. (c-d) Plot of the field intensity into the plane ξs for $\omega = 0.01$ and $P_L = 0.15mW/m$, for a beam launched in $\langle\xi\rangle = 0.8$ and with null initial velocity. Wavelength is $633nm$ and $n_0 = 1.3$.

C.4 for the detailed computation):

$$V_m^{v} = \frac{1}{\sqrt{\pi}} e^{\left(\frac{\Theta_m}{\sqrt{2}}\omega_t\right)^2} F(\Theta_m \omega_t) \tag{3.70}$$

where F is defined by eq. (C.17) and Θ_m in section 3.2.3: in the Poisson case it is $\Theta_m = \pi m$. Typical profile in the Poisson case are plotted in fig. 3.11(a).
From eq. (3.69) and (3.66) it is easily found that

$$W_0(\langle\xi\rangle) = C \sum_{m=1}^{\infty} V_m^{\xi} V_m^{v} \cos(\pi m \langle\xi\rangle) \tag{3.71}$$

with $C = \frac{2k_0^2 P Z_0}{\pi\omega^2 a^2 \beta n_0}$. At variance with the 1D case, the force decreases with the cell thickness a as a^{-2}, having fixed all the other parameters.
Fig. 3.11(b) plots W_0 for $\mu/\kappa = 0$ (Poisson case) and $\mu/\kappa = 100$ (the plot is limited to $\langle\xi\rangle > 0.5$ due to the odd symmetry around axis $\xi = 0.5$): the force has a nonlinear

behavior (its slope increases in proximity of the boundaries) and is stronger in the Poisson case being the nonlocality higher. Moreover, in the Poisson case the force is almost independent from the beam waist (for $\omega < 0.1$ and $\langle\xi\rangle < 0.9$) as in the 1D case, while in the screened case force it varies with the waist due to the lower nonlocality, the latter stronger for smaller beam widths. Fig. 3.11(c) shows the soliton trajectories in the plane ξs for beams at a fixed power, impinging normally on the cell (i.e. with a null initial velocity) and computed through eq. (3.56): the soliton oscillates sinusoidally, with a period Λ [shown in fig. 3.11(d)] decreasing as the beam is launched closer to a boundary, due to the anharmonicity of the potential V_X^m (see section 3.3.2). Finally, given the linear relationship between the nonlinear index perturbation and the intensity profile, the period decreases with power as $P^{-1/2}$.
W_2 can be computed from [see eqs. (3.69) and (3.61)]:

$$W_2(\langle\xi\rangle) = -C\sum_{m=1}^{\infty}(\pi m)^2 V_m^{\xi} V_m^{\upsilon}\cos(\pi m\langle\xi\rangle) \tag{3.72}$$

Fig. 3.11(e) shows the first two terms of the force F_X^m [see eq. (3.62)], W_0 and $W_2\langle y\rangle^2$, respectively. The first order is dominant, being typically about three magnitude orders larger than the other ones.
Finally, in the highly nonlocal approximation and in the Poisson case, the potential V_X^m is given by (3.67), with [see appendix C.5 for details]:

$$c_0^1 = 2C\sum_{m=1}^{\infty}\pi m V_m^{\upsilon}(-1)^m\int_0^{0.5} e^{-\frac{t^2}{w^2}}\cos(\pi m t)dt \tag{3.73}$$

A comparison between the complete form of W_0 and its linear approximation $c_0^1(\langle\xi\rangle - 0.5)$ is reported in fig. 3.11(e): good accuracy is obtained for beams with oscillation amplitudes less than 0.15.

3.4.3 Liquid Crystals

3.4.3.1 Model

In the case of liquid crystals, where optical propagation is governed by the first of eqs. (2.18), eq. (3.54) is valid with the positions $V = -\left(\frac{k_0^2}{2m}\right)D_x\Delta n$[1] and $\Delta n =$

[1]For the sake of simplicity I assumed $D_x = D_t$.

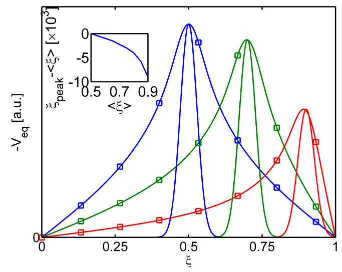

(a) Equivalent potential $V_{eq}(\langle\xi\rangle)$ (inverted in sign) versus ξ.

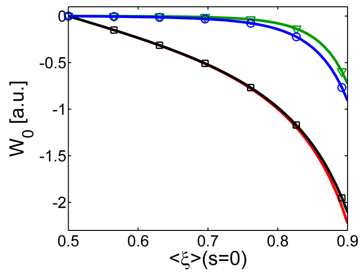

(b) Equivalent force $W_0(\langle\xi\rangle)$ versus $\langle\xi\rangle$.

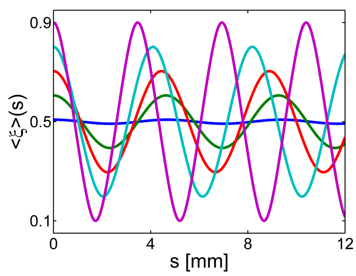

(c) Soliton trajectories for $P = 2mW$.

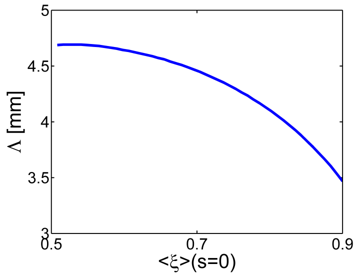

(d) Oscillation period Λ for $P = 2mW$.

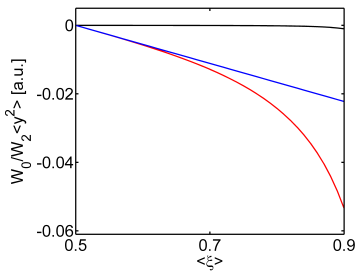

(e) Comparison between W_n terms.

Figure 3.11: (a) Equivalent potential V_{eq} (with inverted sign) versus ξ for $\langle\xi\rangle = 0.5$, 0.7 and 0.9 (solid line with squares) and corresponding intensity profile (solid line). The inset shows the distance among beam peak $\langle\xi\rangle$ and maxima $-V_{eq}$ positions ξ_{peak} versus $\langle\xi\rangle$. (b) Equivalent force W_0 versus beam positions $\langle\xi\rangle$ in the Poisson/screened Poisson case for $\omega = 10\mu m$ (squares/triangles) and $\omega = 2.2\mu m$ (solid line/circles). In the second case I took $\mu/\kappa = 100$. (c) Nonlinear trajectories in the plane ξs in the Poisson case for different initial beam positions and null input velocity, and (d) corresponding oscillation period Λ versus initial beam positions $\langle\xi\rangle$ $(s = 0)$. The beam power is $2mW$, $\beta = 100$, $a = 100\mu m$, $\lambda = 633nm$ and $n_0 = 1.3$. (e) First order force (i.e. W_0) (red line) and second order force (i.e. $W_2 < y^2 >$) (black line) acting on the soliton. Blue straight line represents linear approximation for W_0, stemming from eq. (3.73).

$\epsilon_a\left[\sin^2(\theta-\delta)-\sin^2(\theta_0-\delta)\right]$, with $m=k_0n_e\cos\delta$. In section 3.2.4.2 I demonstrated that, for typical (experimental) powers, only terms up to P^2 must be considered to reach a good approximation; hence, I can set $\Delta n=\epsilon_a\left\{\sin[2(\theta_0-\delta)]\Psi+\cos[2(\theta_0-\delta)]\Psi^2\right\}$ and, from eq. (3.42), perturbation angle is $\Psi=\gamma P g_1+\gamma^2P^2g_2$. Thus, considering only terms up to P^2, I get:

$$\Delta n\cong\epsilon_a\left\{\sin[2(\theta_0-\delta)]\left(\gamma Pg_1+\gamma^2P^2g_2\right)+\cos[2(\theta_0-\delta)]\gamma^2P^2g_1^2\right\} \tag{3.74}$$

Therefore, the equivalent potential V_{eq} (defined in section 3.3.1) is:

$$V_{eq}=V_{eq}^L+V_{eq}^{NL} \tag{3.75}$$

where I defined $\left(|A|^2=Ce^{-\left[\xi^2/\omega_x^2+\upsilon^2/\omega_t^2\right]}\text{ with }C=2Z_0/\left(n_e\pi\omega_x\omega_ta^2\right)\right)$

$$\begin{aligned}V_{eq}^L&=-\frac{\epsilon_ak_0}{2n_e\cos\delta}\sin[2(\theta_0-\delta)]\left(\frac{\gamma P}{\sqrt{\pi\omega_t^2}}\int_{-\infty}^{\infty}e^{-\frac{\upsilon^2}{\omega_t^2}}g_1d\upsilon+\frac{\gamma^2P^2}{\sqrt{\pi\omega_t^2}}\int_{-\infty}^{\infty}e^{-\frac{\upsilon^2}{\omega_t^2}}g_2d\upsilon\right)\\V_{eq}^{NL}&=-\frac{\epsilon_ak_0}{2n_e\cos\delta}\cos[2(\theta_0-\delta)]\frac{\gamma^2P^2}{\sqrt{\pi\omega_t^2}}\int_{-\infty}^{\infty}e^{-\frac{\upsilon^2}{\omega_t^2}}g_1^2d\upsilon\end{aligned} \tag{3.76}$$

The force W_0 acting on the soliton is (section 3.3.1):

$$W_0=W_0^L+W_0^{NL} \tag{3.77}$$

being $W_0^L=\left.\frac{\partial V_{eq}^L}{\partial\xi}\right|_{\xi=\langle\xi\rangle}$ and $W_0^{NL}=\left.\frac{\partial V_{eq}^{NL}}{\partial\xi}\right|_{\xi=\langle\xi\rangle}$ the terms stemming from linear and quadratic parts[1] of Δn, respectively. Substituting definitions of $g_{1/2}$ [see eqs. (3.43)] in (3.76), the two forces W_0^L and W_0^{NL} are:

$$\begin{aligned}W_0^L=\frac{\epsilon_ak_0}{2n_e\cos\delta}\sin[2(\theta_0-\delta)]&\left\{\gamma CP\sin[2(\theta_0-\delta)]\left(\sum_{m=1}^{\infty}V_m^\xi V_m^\upsilon\cos(\pi m\langle\xi\rangle)\right)\right.\\&\left.+\gamma^2C^2P^2\sin[4(\theta_0-\delta)]\left[\sum_{m=1}^{\infty}\cos(\pi m\langle\xi\rangle)\left(\sum_{l=1}^{\infty}G_l^mH_l^m\right)\right]\right\}\end{aligned} \tag{3.78a}$$

[1]With respect to Ψ.

$$W_0^{NL} = \frac{\epsilon_a k_0}{2n_e \cos\delta} \cos[2(\theta_0 - \delta)] \sin^2[2(\theta_0 - \delta)] \gamma^2 C^2 P^2 \sum_{m=1}^{\infty} \sum_{l=1}^{\infty} \frac{1}{ml} \left[m \cos(\pi m \langle\xi\rangle) \sin(\pi l \langle\xi\rangle) \right.$$
$$\left. + \, l \cos(\pi l \langle\xi\rangle) \sin(\pi m \langle\xi\rangle) \right] M_{ml}(\langle\xi\rangle) \quad (3.78b)$$

being $H_l^m = \int_{-\infty}^{\infty} F_l^m(v) e^{-\frac{v^2}{\omega_t^2}} dv$ and $M_{ml}(\langle\xi\rangle) = V_m^\xi V_l^\xi \int_{-\infty}^{\infty} V_m^v(v) V_l^v(v) e^{-\frac{v^2}{\omega_t^2}} dv$.

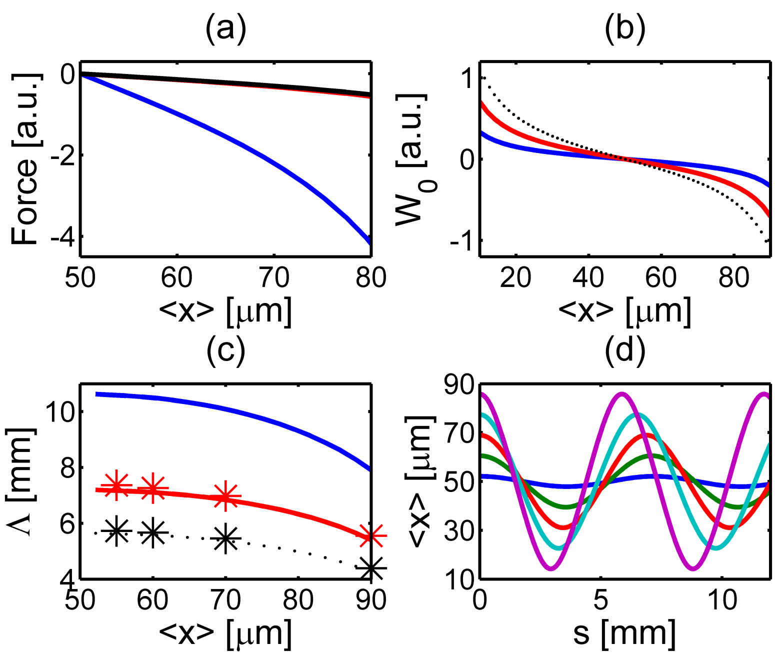

Figure 3.12: (a) Comparison between different components of the total force W_0 versus beam positions: the black line stems from W_0^{NL}, blue and red lines stem from W_0^L, Ψ and Ψ^2 terms, respectively. Power is $1mW$. (b) Boundary force W_0 versus beam position $\langle x\rangle = \langle\xi\rangle\, a$ for $P = 1$ (blue line), 2 (red line) and $3mW$ (black dotted line) in E7 and thickness $a = 100\mu m$. (c) Corresponding oscillation period Λ versus $\langle x\rangle\,(s = 0)$ for zero initial momentum (i.e. beams normal to the input interface) computed from the Ehrenfest's theorem (solid line) and full numerical simulations (stars). Black corresponds to $P = 3mW$, red to $P = 2mW$ and blue to $P = 1mW$. (d) Calculated trajectories of a $2mW$ nematicon versus propagation s for several input positions $\langle x\rangle\,(s = 0)$. Wavelength is $633nm$.

Let me consider a Gaussian beam as in the former cases. Fig. 3.12(a) compares the contributions stemming from the various W_0s, whereas fig. 3.12(b) shows the acting force W_0 for various powers and a fixed cell thickness a (taken equal to $100\mu m$ as in actual samples). Fig. 3.12(c) graphs the soliton oscillation period versus initial

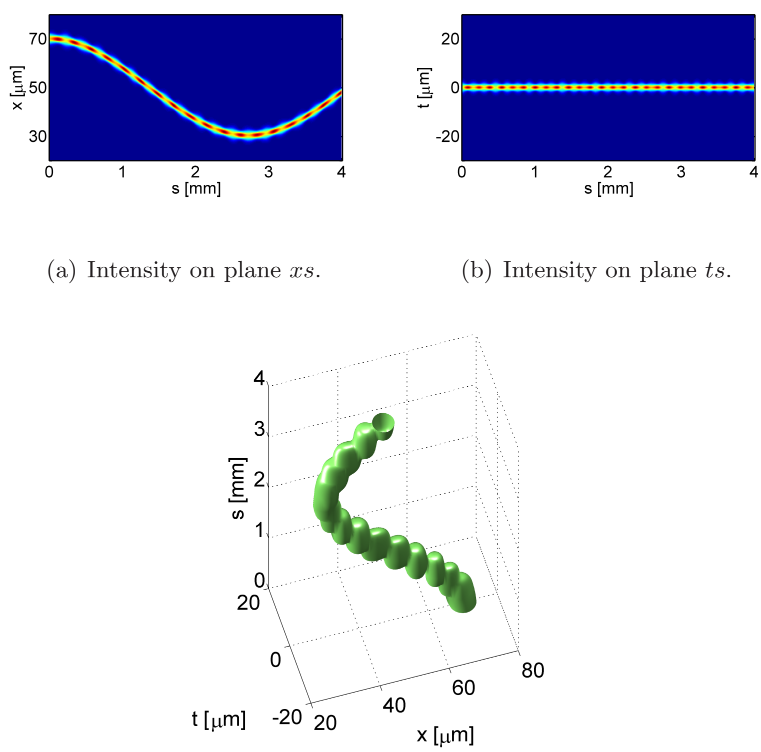

(a) Intensity on plane xs.

(b) Intensity on plane ts.

(c) Intensity isosurface.

Figure 3.13: Soliton intensity profile in the plane xs (a), ts (b) and intensity isosurface (c). The initial beam profile is a Gaussian with waist of $2.8\mu m$, beam center in $x = 70\mu m, t = 0$ and power of $3mW$. The wavevector is normal to the input interface (i.e. null initial velocity) and wavelength is $633nm$. Cell thickness is $100\mu m$.

positions and fig. 3.12(d) the sinusoidal trajectories in the plane xs for a fixed power: the beams impinge normally to the input interface, therefore their initial velocity is null. Fig. 3.12(c) shows results for the oscillation period computed by full-numerical simulations (see appendix B): the agreement is very good. Finally, fig. 3.13 shows the numerically computed soliton profile for a beam with $P = 3mW$, $w_{in} = 2.8\mu m$ and $\langle x \rangle (s = 0) = 70\mu m$, demonstrating its sinusoidal oscillation in the plane xs.

3.4.3.2 Experiments

To verify these findings, a series of experiments was carried out in an $L = 4mm$ long NLC cell of thickness $a = 100\mu m$ and width $> 1cm$, containing the commercial E7.

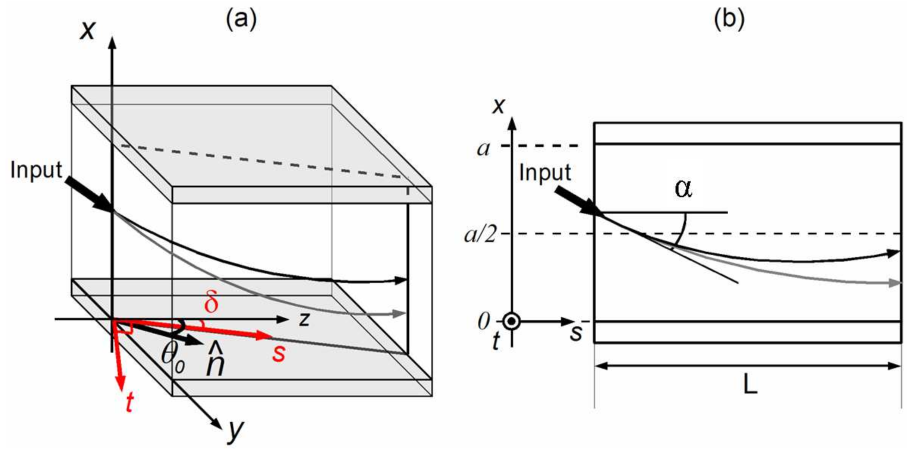

Figure 3.14: (a) 3D sketch of the experimental configuration: the molecular director lies in the cell plane $st \equiv zy$ and the transverse dynamics takes place in xs. (b) Side view: spatial solitons are excited with an input angle α and propagate along s (grey line) in the plane xs; as power increases, so does the repulsive force and the nematicon is pushed away from the (lower) boundary (black line).

The glass interfaces were treated to ensure planar molecular orientation in st with optic axis at $\theta_0 = 30°$ with respect to the normal z to the input interface [fig. 3.14(a)]. In this geometry, the reference systems xts is rotated with respect to xyz by the walk-off $\delta = 7°$ around x, as explained in chapter 2 [see fig. 3.14(a)]. The soliton evolution along st, as well as at the output in xt ($s = L$), were imaged with a microscope and a CCD camera, collecting either the light scattered through the top of the cell (section 2.2) or the transverse profile at the output, respectively. A small offset with respect to $x = a/2$ and an angular tilt α were impressed on the input wavevector to maximize the soliton x-displacement versus power [fig. 3.14(b)]. Nematicons were excited using extraordinarily-polarized beams launched off-center (i.e. $\langle x \rangle \neq a/2$) at the wavelength $1.064\mu m$.

Figure 3.15 compares some of the experimental results with the corresponding predictions from eqs. (3.78), as the input power is varied for a given set of launch conditions. The input angle is modeled as a not null initial velocity, i.e. $\left.\frac{d\langle x \rangle}{ds}\right|_{s=0} = \tan\alpha$. Fig. 3.15(a) shows the calculated trajectories for an input beam in $s = 0$ and $\langle x \rangle\,(s = 0) = 58\mu m$, with input wavevector normal to $\hat{\boldsymbol{y}}$ and forming an angle of $0.6°$ with $\hat{\boldsymbol{z}}$. Clearly, under the given excitation, the soliton is expected to interact with the boundary-driven potential and oscillate for a fraction of the period Λ shifting along x in $z = L$ as the power changes. The acquired photographs of the output in xt are superimposed and shown in fig. 3.15(b) for various powers (from 0.5 to $6mW$), demonstrating the predicted power-dependent repulsion due to the boundary potential. Such nonlinear transverse dynamics along x is in excellent agreement with the results from the integration of eq. (3.58) [using eqs. (3.78) for the force] using the sample parameters, as displayed in fig. 3.15(c).

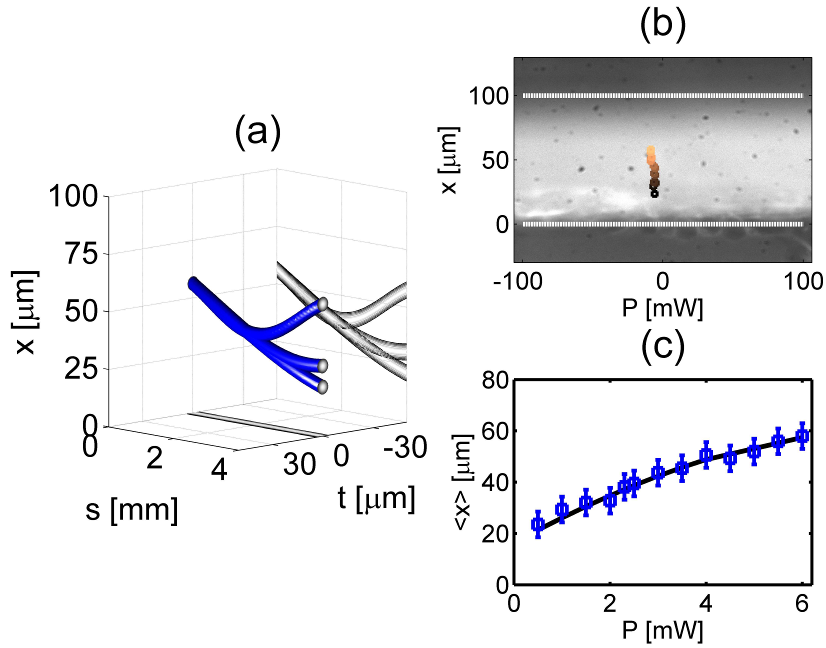

Figure 3.15: (a) Calculated soliton trajectories for the conditions used in the experiments (see text) and input powers $P = 1.5, 3, 6mW$, respectively. (b) Collected and superimposed photographs of spatial soliton profiles at the cell output for various powers; the squares correspond to the symbols in (c). (c) Experimental (squares) and calculated (line) output positions versus input power. To fit the experimental data I assumed a coupling coefficient for the power of 50%.

4

Vector Solitons in Nematic Liquid Crystals

4.1 Vector Solitons: an Introduction

The simplest vector solitons (VS) are shape-preserving self-localized solutions of coupled Schröedinger nonlinear evolution equations (6). Among them, Manakov spatial solitons (88) can be derived by the inverse scattering technique and were first observed in AlGaAs with orthogonally-polarized collinear beams interacting incoherently (89). Two-wavelength vector solitons in Kerr media were predicted by De La Fuente and co-workers (90), whereas VS consisting of bright and dark solitons were reported by Shalaby and Barthelemy (91). Quadratic solitons belong to the class of VS, because they encompass the parametric interaction of waves at different wavelengths (48; 92; 93). The resulting self-guided beams, in general, have energy flows along directions depending on relative powers and birefringence (92). In photorefractives, VS were demonstrated in various forms, ranging from incoherent VS (94) to VS with bright and dark solitary components (95), soliton dipoles (96) and multimode solitons (94; 97). The term molecule soliton was introduced to embrace the rich and complex VS phenomenology (35).

In this chapter I study the propagation of vector solitons in NLC encompassing two beam of two different wavelengths, i.e. a bi-color soliton. I will show how numerical results are in good agreement with experimental observations. The results discussed here were partially published in Ref. (98).

4.2 Cell Geometry and Basic Equations

Let me consider two beams at two different wavelengths, λ_1 and λ_2 respectively, which impinge with arbitrary angles on a cell in an anisotropic configuration, with wavevectors $\mathbf{k}_1$ and $\mathbf{k}_2$ belonging to the plane yz (see fig. 4.1). I define $\theta_j = \theta_{0j} + \Psi$ the angle between the director $\hat{\boldsymbol{n}}$ and the wavevector $\mathbf{k}_j$ $(j = 1, 2)$ [see fig. 4.1(c)], with θ_{0j} the value when the optical reorientation is negligible, i.e. in the linear regime, and Ψ the perturbation induced by light. I get $\theta_{0j} = \theta_0 - \theta_j^{rif}$ (if both wavevectors are parallel to z $\theta_{0i} = \theta_0$)[1], where θ_j^{rif} is the angle between axis z and $\mathbf{k}_j$, and θ_0 the angle between $\hat{\boldsymbol{n}}$ and $\hat{\boldsymbol{z}}$ [fig. 4.1(d)], imposed by the rubbing on the glass slides along yz (fig. 4.1). I assume, without loss of generality, that $\lambda_2 > \lambda_1$, i.e. $\delta_2 < \delta_1$. Furthermore, I define the axis s as the direction in the midst of the individual Poynting vectors[2]. The equations describing soliton propagation are

$$K\nabla_\perp^2\theta + \frac{\epsilon_0\epsilon_{a1}}{4}|A_1|^2 \sin\left[2(\theta_1 - \delta_1)\right] + \frac{\epsilon_0\epsilon_{a2}}{4}|A_2|^2 \sin\left[2(\theta_2 - \delta_2)\right] = 0 \tag{4.1}$$

$$2ik_{0j}n_{ej}\cos\delta_j \frac{\partial A_j}{\partial s_j} + D_{tj}\frac{\partial^2 A_j}{\partial t_j^2} + D_{xj}\frac{\partial^2 A_j}{\partial x_j^2} + k_{0j}^2\delta\epsilon_{ttj}A_j = 0 \quad (j = 1, 2) \tag{4.2}$$

being θ the angle formed by $\hat{\boldsymbol{n}}$ and z.[3] Eq. (4.1) is expressed in the reference system xts as defined above: the second derivative of the director angle distribution along s was neglected[4]. Moreover, in eq. (4.1) terms coming from the interference between the two beams were neglected due to their fast variation in time, with a frequency[5] much larger than the typical cut-off in NLC(58; 60).

Eqs. (4.2) are written respectively in the frameworks $x_j t_j s_j$, obtained by rotating xyz by an angle β_j around $\hat{\boldsymbol{x}}$ [fig. 4.1(d)]; additionally, in eq. (4.2) the relation between nonlinear perturbations on the dielectric tensor $\boldsymbol{\epsilon}$ and angles θ_j is $\delta\epsilon_{ttj} = \epsilon_{aj}\left[\sin^2(\theta_j - \delta_j) - \sin^2(\theta_{0j} - \delta_j)\right]$ $(j = 1, 2)$. For small perturbations, i.e. for low beam

[1] Angles are considered positive (negative) when $y > 0 (y < 0)$, for absolute values below π.

[2] With reference to fig. 4.1(d) the angle β between s and z is given by $(\beta_1 + \beta_2)/2$.

[3] Angles θ, θ_1 and θ_2 differ each other for a constant so their derivatives are equal.

[4] Clearly, this approximation is good as long as the angle between $\mathbf{s}_1$ and $\mathbf{s}_2$ is small.

[5] Obviously this frequency is proportional to the difference $\frac{c}{\lambda_1} - \frac{c}{\lambda_2}$, being c the light-speed in vacuum.

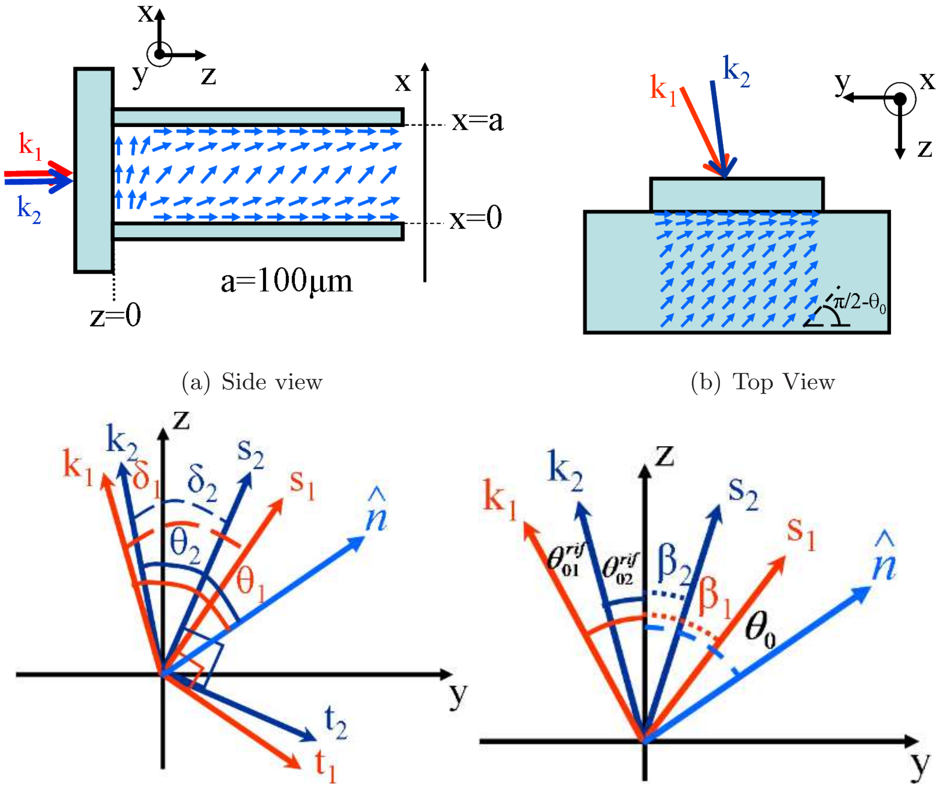

(a) Side view

(b) Top View

(c) Electromagnetic vectors

(d) Angles respect to cell reference system

Figure 4.1: Sketch of the cell and excitation schematic. Fig. 4.1(a) shows the cell side view, i.e. plane xz. Both wavevectors $\mathbf{k}_1$ and $\mathbf{k}_2$ lie in the mid-plane to avoid undesired displacements along x due to boundary effects (see chapter 3). Fig. 4.1(b) shows the plane yz, i.e. the molecular reorientation plane: in absence of excitation, $\hat{\boldsymbol{n}}$ forms an angle θ_0 with $\hat{\boldsymbol{z}}$ owing to rubbing. The two wavevectors, in the most general case, have different directions. In 4.1(c) I plot the relevant vectors for electromagnetic propagation: $\hat{\boldsymbol{n}}$ is the molecular director, $\mathbf{s}_j$ the Poynting vector, $\mathbf{t}_j$ the extraordinary electric field polarization, δ_j the walk-off and θ_j the angle between director and $\mathbf{k}_j$ ($j = 1, 2$). In fig. 4.1(d) I graph the vectors in the cell reference system xyz: θ_{0j}^{rif} and β_j are the angles formed by $\mathbf{k}_j$ and s_j with $\hat{\boldsymbol{z}}$, respectively. All quantities are referred to the single beam propagation, i.e., when the other beam is absent.

powers, I can linearize $\delta\epsilon_{tt}$ and, consequently, eqs. (4.2) turn into

$$2ik_{0j}n_{ej}\cos\delta_j\frac{\partial A_j}{\partial s_j}+D_{tj}\frac{\partial^2 A_j}{\partial t_j^2}+D_{xj}\frac{\partial^2 A_j}{\partial x_j^2}+k_{0j}^2\epsilon_{aj}\sin\left[2(\theta_{0j}-\delta_j)\right](\theta_j-\theta_{0j})A_j=0 \quad (j=1,2) \tag{4.3}$$

4.3 Highly Nonlocal Limit

4.3.1 Reorientation

In full analogy with the analysis of a single beam developed in section 2.5.1.1, linearization of eq. (4.1) gives:

$$\begin{aligned} K\nabla_\perp^2\Psi+\left\{\frac{\epsilon_0\epsilon_{a1}}{2}|A_1|^2\cos\left[2(\theta_0-\delta_1)\right]+\frac{\epsilon_0\epsilon_{a2}}{2}|A_2|^2\cos\left[2(\theta_0-\delta_2)\right]\right\}\Psi \\ +\frac{\epsilon_0\epsilon_{a1}}{4}|A_1|^2\sin\left[2(\theta_0-\delta_1)\right]+\frac{\epsilon_0\epsilon_{a2}}{4}|A_2|^2\sin\left[2(\theta_0-\delta_2)\right]=0 \end{aligned} \tag{4.4}$$

Formally, eq. (4.4) can be written as $L'=\left[L+a'(x,t)+b'(x,t)\right]\Psi=a(x,t)+b(x,t)$ with the boundary condition $\Psi|_C=0$, being C the curve which describes the cell edges. Therefore, L' is a linear operator acting on Ψ, formed respectively by L, the Laplacian, and by the multiplication for the functions a' and b', proportional to the forcing terms a and b, respectively. Given that L' is linear, the general solution has the form $\Psi=\Psi_a+\Psi_b$, where $L'\Psi_a=a(x,t)$ and $L'\Psi_b=b(x,t)$ and where the boundary conditions $\Psi_a|_C=0$ and $\Psi_b|_C=0$ must be applied. The next step is to Taylor-expand both perturbation and fields as for a single field. Problems can arise from the presence of the terms $a'\Psi$ and $b'\Psi$, which destroy the symmetry $t/-t$ with respect to the beam center. To simplify the mathematical description I neglect these terms in eq. (4.4), obtaining

$$K\nabla_\perp^2\Psi+\frac{\epsilon_0\epsilon_{a1}}{4}|A_1|^2\sin\left[2(\theta_0-\delta_1)\right]+\frac{\epsilon_0\epsilon_{a2}}{4}|A_2|^2\sin\left[2(\theta_0-\delta_2)\right]=0 \tag{4.5}$$

Let me focus on the accuracy of the employed approximation. I have to check that

$$\cos\left[2(\theta_0-\delta_j)\right]\Psi_0<<\frac{1}{2}\sin\left[2(\theta_0-\delta_2)\right] \qquad (j=1,2) \tag{4.6}$$

is verified in actual cases. The left hand side of eq. (4.6) is about 0.02 for $\Psi_0\approx 2^\circ$ (according to the full numerical simulations this corresponds to a beam power of about $2mW$), whereas the right hand side is about 0.38: this confirms the validity of the approximation. Therefore, having separated the effects of the two beams, two uncoupled Poisson equations must be solved:

$$K\nabla_{\perp}^2\Psi_j + \frac{\epsilon_0\epsilon_{aj}}{4}|A_j|^2\sin\left[2(\theta_0-\delta_j)\right] = 0 \qquad (j=1,2) \tag{4.7}$$

Noteworthy, eqs. (4.7) possess invariance for translation along t, i.e. if $\Psi(x,t)$ is a solution when $|A|^2 = g(x,t)$, then $\Psi(x,t-t_0)$ is still a solution if $|A|^2 = g(x,t-t_0)$. Finally, the solution for the perturbation angle under all these approximations is

$$\Psi = \Psi_1+\Psi_2 = \Psi_0^{(1)}+\Psi_0^{(2)}+\Psi_2^{(1)}\left[x^2+(t-\langle t_1\rangle(s))^2\right]+\Psi_2^{(2)}\left[x^2+(t-\langle t_2\rangle(s))^2\right] \tag{4.8}$$

having defined

$$\Psi_2^{(j)} = \frac{\epsilon_0\epsilon_{aj}}{16K}|A_j|^2_{x=0,t=0}\sin\left[2(\theta_0-\delta_j)\right] \qquad (j=1,2) \tag{4.9}$$

The functions $\langle t_j\rangle(s)$ depict the transversal coordinate of the j-th beam peak as the latter propagates along s, i.e. its trajectory in the plane ts.

4.3.2 Optical Propagation

In the section 4.3.1 I found an approximate solution for the director distribution in the highly nonlocal limit. Using this result in eq. (4.3) provides

$$\begin{split} 2ik_{01}n_{e1}\cos\delta_1\frac{\partial A_1}{\partial s_1} + D_{t1}\frac{\partial^2 A_1}{\partial t_1^2} + D_{x1}\frac{\partial^2 A_1}{\partial x_1^2} + \\ +k_{01}^2\epsilon_{a1}\sin\left[2(\theta_0-\delta_1)\right]\left\{\Psi_0+\Psi_2^{(1)}\left[x_1^2+(t_1-\langle t_1\rangle)^2\right]+\Psi_2^{(2)}\left[x_1^2+(t_1-\langle t_2\rangle)^2\right]\right\} \end{split} \tag{4.10}$$

$$\begin{split} 2ik_{02}n_{e}\cos\delta_2\frac{\partial A_2}{\partial s_2} + D_{t2}\frac{\partial^2 A_2}{\partial t_2^2} + D_{x2}\frac{\partial^2 A_2}{\partial x_2^2} + \\ +k_{02}^2\epsilon_{a2}\sin\left[2(\theta_0-\delta_2)\right]\left\{\Psi_0+\Psi_2^{(1)}\left[x_2^2+(t_2-\langle t_1\rangle)^2\right]+\Psi_2^{(2)}\left[x_2^2+(t_2-\langle t_2\rangle)^2\right]\right\} \end{split} \tag{4.11}$$

being $\Psi_0 = \Psi_0^{(1)} + \Psi_0^{(2)}$ and with the two reference systems related by the transformations (valid for small $\Delta\beta = (\beta_2 - \beta_1)/2$)

$$\begin{cases} t_{1/2} \cong t \pm s \tan \Delta\beta \\ s_{1/2} \cong s \end{cases} \tag{4.12}$$

It is easy to recognize that eqs. (4.10)-(4.11) are coupled Schröedinger-like equations with a parabolic potential, i.e. two coupled quantum oscillators written in two different frames (coupling takes place by means of $\Psi_2^{(j)}$, which depend on the intensity peak of the j-th beam [see (4.9)]). To complete the analogy, I set $\hbar = 1$, $m_j = (k_{0j} n_{ej} \cos\delta_j)/D_j$, $V_j = -\gamma_j \Psi(x_j, t_j, sj)$ and $\gamma_j = (k_{0j}^2 \epsilon_{aj} \sin[2(\theta_0 - \delta_j)])/(2k_{0j} n_{ej} \cos\delta_j)$. Finally, in my case, time is substituted by the propagation coordinate s.

4.3.3 Soliton Trajectory

In this section I investigate the trajectories as beams propagate inside the cell. To this purpose, I apply the well-known Ehrenfest theorem for the Schröedinger equation (49), relating particles mean velocity to the potential in non-relativistic quantum mechanics. The Ehrenfest theorem provides

$$m_j \frac{d^2 \langle \mathbf{r}_j \rangle}{ds_j^2} = -\iint |\psi_j|^2 \nabla V_j dxdt \quad (j = 1, 2) \tag{4.13}$$

being $\langle \mathbf{r}_j \rangle = \iint \mathbf{r}_j |\psi_j|^2 dxdt$, $\psi_j = A_j / \sqrt{\iint |A_j|^2 dxdt}$, $\boldsymbol{r} = x\hat{x} + t\hat{t}$ and $\nabla = \frac{\partial}{\partial x}\hat{x} + \frac{\partial}{\partial t}\hat{t}$. Writing eq. (4.13) in the reference system xts yields

$$m_j \frac{d^2 \langle x_j \rangle}{ds_j^2} = -\iint |\psi_j|^2 \frac{\partial V_j}{\partial x_j} dxdt \tag{4.14}$$

$$m_j \frac{d^2 \langle t_j \rangle}{ds_j^2} = -\iint |\psi_j|^2 \frac{\partial V_j}{\partial t_j} dxdt \quad (j = 1, 2) \tag{4.15}$$

From section 4.3.2 it is[1] $V_j = -\gamma_j \left\{ \Psi_0 + \Psi_2^{(1)} \left[x_j^2 + (t_j - \langle t_1 \rangle)^2 \right] + \Psi_2^{(2)} \left[x_j^2 + (t_j - \langle t_2 \rangle)^2 \right] \right\}$. Substitution of the integrals in the right hand side of eqs. (4.14)-(4.15) leads to

[1] I note that the next formula for the refractive index profile was computed in the highly nonlocal regime, without any ansatz on beam profile; see section 4.3.1.

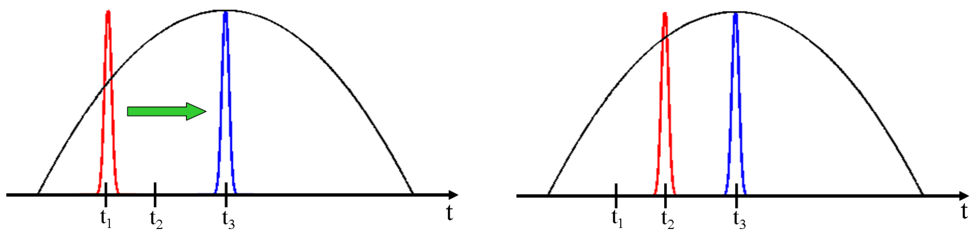

(a) Initial position (b) Motion due to the mutual attraction

Figure 4.2: Reciprocal interaction between two beams (red and blue profiles) due to the nonlocal index perturbation. For the sake of simplicity, one beam (the blue) is fixed in the space; actually, the interaction is mutual and both beams move along t. In 4.2(a) the blue beam induces an index well (black line) which exerts a force (proportional to the slope of black curve) on the red one, consequently moving it from t_1 to t_2 [fig. 4.2(b)].

$$m_j \frac{d^2 \langle x_j \rangle}{ds_j^2} = 2\left(\Psi_2^{(1)} + \Psi_2^{(2)}\right) \langle x_j \rangle \tag{4.16}$$

$$m_j \frac{d^2 \langle t_j \rangle}{ds_j^2} = 2\left[\Psi_2^{(1)} \left(\langle t_j \rangle - \langle t_1 \rangle\right) + \Psi_2^{(2)} \left(\langle t_j \rangle - \langle t_2 \rangle\right)\right] \quad (j = 1, 2) \tag{4.17}$$

Being $\langle x_j \rangle = 0$ for even intensity profiles, eq. (4.16) shows there is no force acting on the beams along x, thereby the beam is undeflected in the xs plane. Conversely, in the xt plane the beams *perceive* a force proportional to the misplacement between the two waves. Specifically, I find

$$m_1 \frac{d^2 \langle t_1 \rangle}{ds_1^2} = 2\Psi_2^{(2)} \left(\langle t_1 \rangle - \langle t_2 \rangle\right) \tag{4.18}$$

$$m_1 \frac{d^2 \langle t_2 \rangle}{ds_2^2} = 2\Psi_2^{(1)} \left(\langle t_2 \rangle - \langle t_1 \rangle\right) \tag{4.19}$$

Solutions of eqs. (4.18)-(4.19) provide the soliton trajectories in plane $t_j s_j$. Note how every beam is affected only by the potential of the other one and the reciprocal attraction [$\Psi_2^{(j)} < 0$ from (2.14)] increases as the distance, which does not depend on the reference system, decreases [see figs. 4.2(a)-4.2(b)]. In general, quantities $\Psi_2^{(j)} (j = 1, 2)$ depend on s_j through the beams' peak intensity variation, as predicted by (2.14). To get a closes form for $\langle t_j \rangle$ I neglect these fluctuations; noteworthy, this condition is fulfilled if the single beams are solitons.

Writing eqs. (4.18)-(4.19) in the system xts, I use (4.12) and, remembering that $s \cong s_1$, I obtain

$$m_1 \frac{d^2 \langle t_1 \rangle}{ds^2} = 2\Psi_2^{(2)} \left(\langle t_1 \rangle - \langle t_2 \rangle \right) \tag{4.20}$$

$$m_1 \frac{d^2 \langle t_2 \rangle}{ds^2} = 2\Psi_2^{(1)} \left(\langle t_2 \rangle - \langle t_1 \rangle \right) \tag{4.21}$$

From eq. (4.21) I derive $\langle t_1 \rangle = \langle t_2 \rangle - \frac{m_2}{2\gamma_2 \Psi_2^{(1)}} \frac{d^2 \langle t_2 \rangle}{ds^2}$; substituting into eq. (4.20) I found a single fourth order equation:

$$D \frac{d^4 \langle t_2 \rangle}{ds^4} + C \frac{d^2 \langle t_2 \rangle}{ds^2} = 0 \tag{4.22}$$

with $C = m_1 + m_2 \frac{\gamma_1 \Psi_2^2}{\gamma_2 \Psi_2^{(1)}}$ and $D = -\frac{m_1 m_2}{2\gamma_2 \Psi_2^1}$. Setting $\alpha = \sqrt{C/D}$ the general integral of eq. (4.22) is:

$$\begin{cases} \langle t_1 \rangle = -\left(\dfrac{1}{\alpha^2} + \dfrac{m_2}{2\gamma_2 \Psi_2^{(1)}} \right) \left[k_1 \cos(\alpha s) + k_2 \sin(\alpha s) \right] + k_3 s + k_4 \\ \langle t_2 \rangle = -\dfrac{1}{\alpha^2} \left[k_1 \cos(\alpha s) + k_2 \sin(\alpha s) \right] + k_3 s + k_4 \end{cases} \tag{4.23}$$

Let me briefly discuss the main properties of (4.23); a qualitative sketch of the resulting trajectories is in fig. 4.3. The terms linear in s represent a common mean direction of propagation for the two beam energies, i.e. the propagation of a multi-color vector soliton, determined by the balance between the beam powers and, in general, distinct from the case of a single beam. Conversely, the sinusoidal terms are related to single beam oscillations around the mean propagation direction, as shown in fig. 4.3, and the two beams oscillate in phase opposition. Eventually, the oscillation period becomes independent from the initial conditions but is a function of the power balance.

4.3.4 Solution for Initially Overlapping Beams

To get a solution for a specific set of launch conditions, I have to impose the corresponding boundary conditions to establish the constants k_1, k_2, k_3 and k_4. For example, let me consider two beams of different wavelengths launched normally to the cell input interface, i.e. with both wavevectors parallel to z or $\beta_1 = \delta_1$, $\beta_2 = \delta_2$ and $\beta = (\delta_2 + \delta_1)/2$ and at the same point; thus $\langle t_1 \rangle (s=0) = \langle t_2 \rangle (s=0) = 0$, $\left. \frac{d\langle t_1 \rangle}{ds} \right|_{s=0} = -\tan \Delta\beta$ and

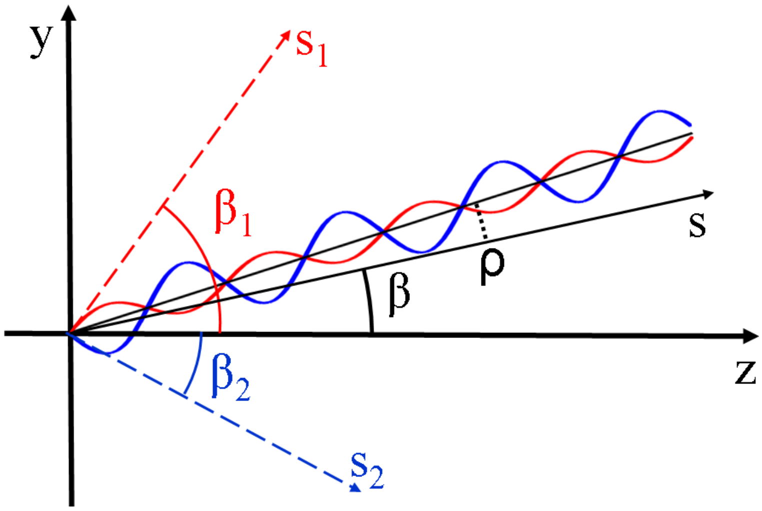

Figure 4.3: Plot of vector soliton trajectory. Angle between vector soliton direction and z is given by $\beta+\rho$, where β is the angle between axis s and z (see note 2) and $\rho = \arctan k_3$ from eq. (4.23). Single solitons oscillate sinusoidally around this direction, keeping a phase shift equal to π. s_1 and s_2 represent single beam energy direction when other beam is lacking. In this plot beams are launched at the same point, i.e. their positions are identical in $z=0$.

$\left.\frac{d\langle t_2\rangle}{ds}\right|_{s=0} = \tan\Delta\beta$, where $\Delta\beta = \frac{\delta_2-\delta_1}{2}$ [1] (I suppose that for each beam the derivative in $s=0$ is unchanged with respect to the single beam case). After some simple algebra I find $k_1 = k_4 = 0$, $k_3 = \tan\Delta\beta\left(1+\frac{4\gamma_2\Psi_2^{(1)}}{\alpha^2 m_2}\right)$ and $k_2 = \tan\Delta\beta\frac{4\gamma_2\Psi_2^{(1)}}{\alpha m_2}$. Replacing these in eq. (4.23) the beams trajectories are

$$\begin{cases} \langle t_1\rangle = -\left(\frac{1}{\alpha^2}+\frac{m_2}{2\gamma_2\Psi_2^{(1)}}\right)\tan\Delta\beta\frac{4\gamma_2\Psi_2^{(1)}}{\alpha m_2}\sin(\alpha s)+\tan\Delta\beta\left(1+\frac{4\gamma_2\Psi_2^{(1)}}{\alpha^2 m_2}\right)s \\ \langle t_2\rangle = -\frac{1}{\alpha^2}\tan\Delta\beta\frac{4\gamma_2\Psi_2^{(1)}}{\alpha m_2}\sin(\alpha s)+\tan\Delta\beta\left(1+\frac{4\gamma_2\Psi_2^{(1)}}{\alpha^2 m_2}\right)s \end{cases} \tag{4.24}$$

Therefore, the vector soliton propagates along a direction at an angle Δ with z, given by:

$$\Delta = \beta+\rho = \beta+\arctan\left[\tan\Delta\beta\left(1-\frac{2m_1\gamma_2\Psi_2^{(1)}}{m_1\gamma_2\Psi_2^{(1)}+m_2\gamma_1\Psi_2^{(2)}}\right)\right] \tag{4.25}$$

[1] In my case $\Delta\beta > 0$ because I have $\lambda_1 > \lambda_2$.

If beam 1 is not present, I have $\Psi_2^{(1)} = 0$, i.e. $\Delta = \delta_2$; if beam 2 is absent, I have $\Psi_2^{(2)} = \delta_1$, i.e. $\Delta = \delta_1$; in both cases the oscillation amplitudes go to zero and the period to infinity, as expected. The results obtained for $\theta_0 = \pi/6$, $\lambda_1 = 1064nm$ and $\lambda_2 = 633nm$ from eqs. (4.24) and (4.25) are shown in fig. 4.4: every vector soliton property is established by the balance between individual beam powers. Let me discuss the results for the oscillation amplitudes. For $I_{red} > 89Wmm^{-2}$ the absolute value of the amplitudes increases monotonically with I_{IR}; physically, at low I_{IR} the red attraction is dominant and the infrared beam collapses into red without oscillations, whereas for higher I_{IR} infrared force begins to contrast the red attraction and the oscillation amplitude increases. This process continues until the infrared beam becomes stronger than the red: at this point, the amplitude decreases as I_{IR} is grows. This behavior is visible in the range displayed in figs. [4.4(a)]-[4.4(b)] for $I_{red} = 7$ and $48Wmm^{-2}$. Moreover, the amplitudes are in phase opposition having the sign inverted: in particular, the red (infrared) oscillation amplitude is positive (negative) being its energy direction above (below) Δ. To conclude the discussion about oscillation amplitudes, it is important to note that their size is a few microns, making their observation very hard due to the blur caused by scattered photons.

The oscillation period is graphed in fig. 4.4(c): for a given I_{red} the period diminishes as I_{IR} increases, and vice versa, owing to the larger attractive force between the beams. Fig. 4.4(d) plots the vector soliton propagation angle Δ: when the infrared is negligible I have $\Delta = \delta_1$, i.e. propagation along the red walk-off ($\Delta \to \delta_2$), when the red is negligible with respect to the infrared, the propagation is along the infrared walk-off ($\Delta \to \delta_1$). Comparing, for example, blue and green curves it is easy to see that the transition between these two limits is as sharp as the parameter I_{red} is low, being the red strength weaker.

The red oscillations and the infrared beam act asymmetrically on the interaction, being the refractive index well (induced at a fixed power) larger for red wavelengths than for infrared due to the larger coupling between the optical field and the NLC at higher frequencies.

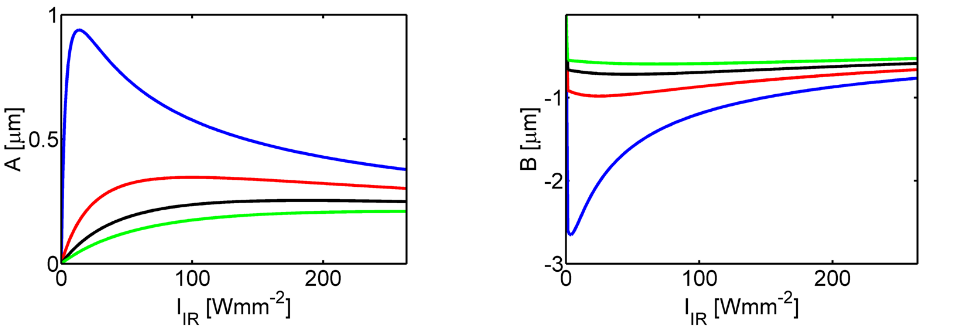

(a) Oscillation amplitude for beam at $\lambda_2 = 633nm$

(b) Oscillation amplitude for beam at $\lambda_1 = 1064nm$

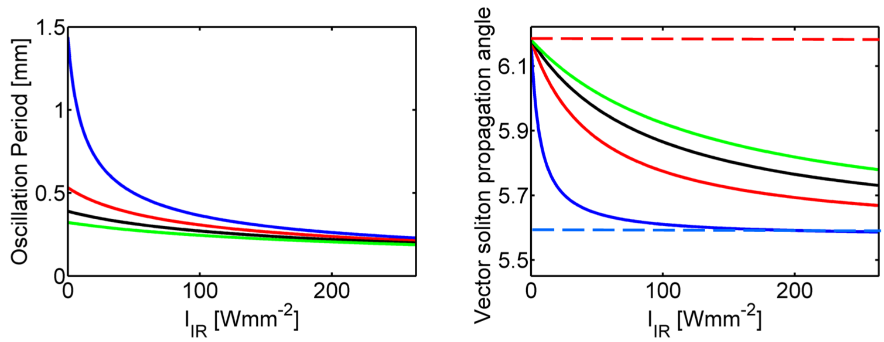

(c) Oscillation period

(d) Vector soliton propagation angle Δ

Figure 4.4: [Fig. 4.4(a)] plots the oscillation amplitude $B = -\frac{1}{\alpha^2}\tan\Delta\beta\frac{4\gamma_2\Psi_2^{(1)}}{\alpha m_2}$ for the beam at $\lambda = 633nm$ versus the peak infrared intensity I_{IR}. Each curve corresponds to a different red intensity peak I_{red}: $7Wmm^{-2}$(blue), $48Wmm^{-2}$(red), $89Wmm^{-2}$(black) and $130Wmm^{-2}$(green), this correspondence being valid for all the other subfigures. Fig. [4.4(a)] plots the infrared oscillation amplitude $A = -\left(\frac{1}{\alpha^2} + \frac{m_2}{2\gamma_2\Psi_2^{(1)}}\right)\tan\Delta\beta\frac{4\gamma_2\Psi_2^{(1)}}{\alpha m_2}$. Fig. [4.4(c)] reports the oscillation period $(2\pi/\alpha)$ versus the two intensity peaks. Finally, fig. [4.4(d)] shows the propagation angle (in degrees) of the vector soliton with respect to z, versus the two intensity peaks; dashed straight lines indicate the single beam walk-off for red (red line) and infrared beams (blue line), respectively. Intensities used in these plots correspond to a few milliwatts for waists of $2 \div 10\mu m$, typical values in actual experiments.

4.4 Breathing

4.4.1 Coupling Geometry

To explore the breathing behavior I focus on the case of two collinear Poynting vectors, i.e. $\mathbf{S}_1 = \mathbf{S}_2$. In such way the two different reference frames $x_1t_1s_1$ and $x_2t_2s_2$ coincide; hence, the propagation equations for the two components at different wavelengths can be written in the same coordinate system xts (see section 4.2). In practice, it is possible to achieve this condition by tilting one wavevector with respect to the other. In simulations and experiments reported hereafter, I assume $\mathbf{k}_1$ normal to the input interface, i.e. parallel to $\hat{\boldsymbol{z}}$ [fig. 4.1(a)-4.1(b)], and $\mathbf{k}_2$ rotated until $\hat{\boldsymbol{s}}_2 = \hat{\boldsymbol{s}}_1$ (see fig. 4.5).

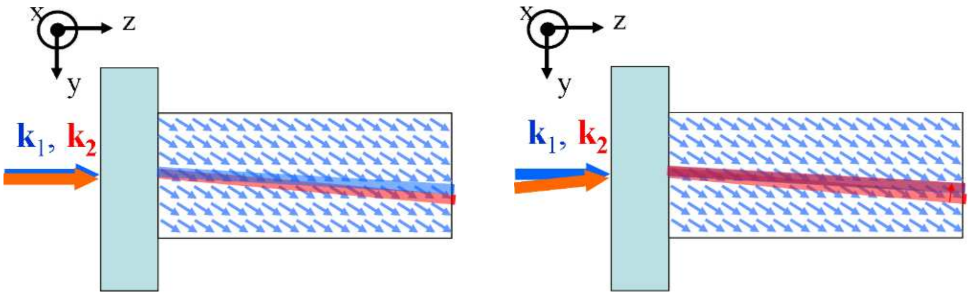

(a) Different Poynting vectors directions

(b) Collinear Poynting vectors

Figure 4.5: Fig. 4.5(a) shows beam profiles when both wavevectors $\mathbf{k}_1$ and $\mathbf{k}_2$ are normal to the input interface. Fig. 4.5(b) shows the case of collinear energy propagation directions for the two beams, having kept $\mathbf{k}_1$ fixed and having rotated $\mathbf{k}_2$.

To enlighten the most important physical properties I assumed $\theta_0 = \pi/6$ (a different rubbing produces only quantitative differences).

4.4.2 Comparison Between Numerical Simulations and Experimental Observations

In this section I discuss the results of numerical simulations of eqs. (4.1)-(4.2) (employed code is described in section B.1) and their comparison with experiments. For the experimental work a NLC cell was employed as in fig. 4.1, with $\theta_0 = \pi/6$ with respect to axis z. The cell is of thickness $a = 100\mu m$ and is filled with E7. Two extraordinarily polarized Gaussian beams at wavelengths 633 (red) and 1064nm (IR) are launched as explained in section 4.4.1, and the propagation is investigated by acquiring the scattered light through the cell top by means of a microscope and a CCD camera. The light behavior at both wavelengths is monitored but, in order to prevent chromatic distortions due to the microscope, the infrared component is filtered out; for this reason I present only images of the visible component at $633nm$. Additional optics are arranged such that both beams have equal Rayleigh lengths of $60\mu m$, so that diffraction lengths are similar. The corresponding minimum waists are 2.8 and $3.7\mu m$ for red and IR, respectively. The soliton propagation distance is nearly twenty times the diffraction length.

Firstly, the linear behavior is investigated, i.e., when each beam diffracts either in the absence of the second one or in the presence of negligible XPM; then both components are launched to exploit XPM and generate a VS thanks to the combined effect. I report the experimental photographs in fig. 4.6 in the plane ts. In the first plot of fig. 4.6 a 1.2 mW IR beam is launched , together with a low-power red beam (a power of $0.1mW$, i.e. a negligible contribution to reorientation dynamics) is used as a probe to scan the index well induced by the IR[1]. The IR beam is unable to self-localize, as the red probe diffracts. The second panel of fig. 4.6 displays the case of a $0.4mW$ red beam launched alone: self-focusing does not occur and beam diffracts. Instead, when $1.2mW$ IR and $0.4mW$ red beams are injected together, as in the last panel of fig. 4.6, the nonlinear response is enhanced through incoherent XPM and supports a self-localized wave, i.e., a *two-color vector soliton*.

The white contour lines in fig. 4.6 are the simulation results. Owing to the actual experimental limitations (that include the use of a non-achromatic lens, wavelength dependent Fresnel reflections and scattering, the presence of a inhomogeneous NLC transition layer in $0 < z < 100\mu m$), in the simulations I implement a phase-front curvature for the input beams and assume unequal coupling coefficient at the two wavelengths. To investigate the breathing of these multicomponent beams, both red and IR input powers P_{red} and P_{IR} are varied, respectively, while keeping the launch conditions (Rayleigh length, tilt, polarization) fixed. Figure 4.7 (left column) shows the

[1] I remind that shorter wavelengths are better confined than longer ones: this means that, assuming that both beams undergo the same index profile, red diffraction implies IR diffraction as well. In fact, given the better coupling with NLC molecules, the red index well is even deeper than the IR one for a given director distribution.

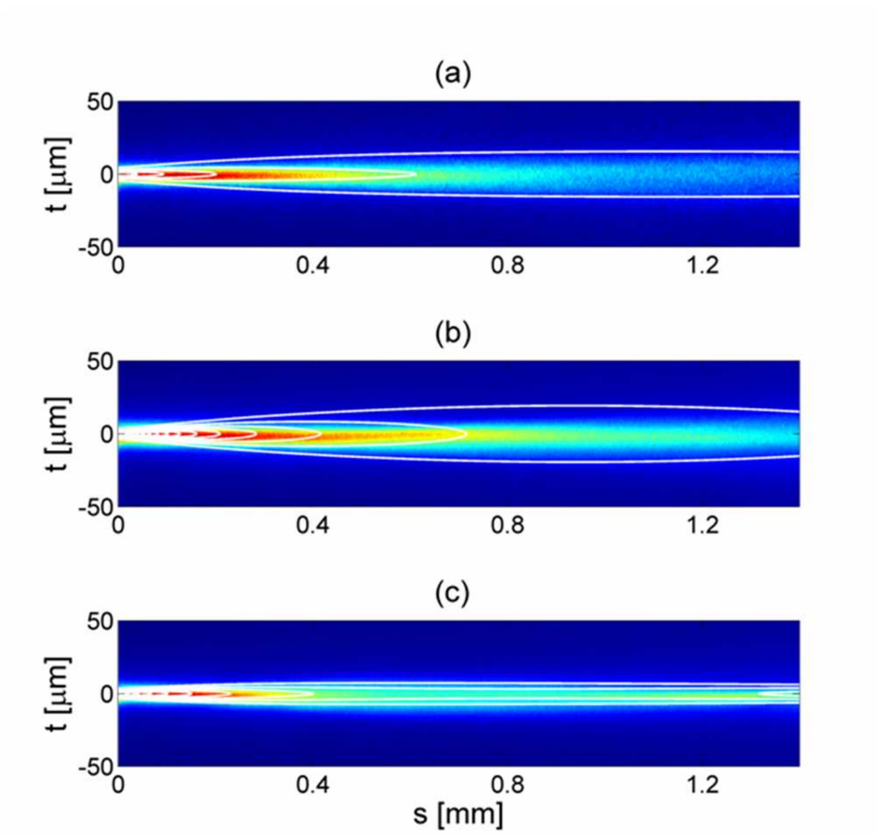

Figure 4.6: Color-coded acquired intensity profiles for red light in the plane ts (i.e. after a rotation by δ). Contour maps of the calculated intensity distributions are superimposed (white lines) to the experimental data. (a) A weak $0.1mW$ red beam is co-launched with a $1.2mW$ IR beam; (b) a $0.4mW$ red beam is injected in the absence of IR; (c) $0.4mW$ red and $1.2mW$ IR beams are co-launched and generate a vector soliton. The simulations were carried out taking effective input coupling efficiency of 40% and 50% for red and IR and initial beam curvatures of radius -130 m (waist in $z = -40\mu m$), respectively.

experimental yz evolution of a red beam with fixed power as the IR power is increased; clearly, the red beam becomes more confined as IR power increases due to a deeper index well, as expectable on the basis of XPM [see eq. (4.1)]. The right column shows the predicted behavior of the red component in the plane ts, demonstrating an excellent agreement with measurements.

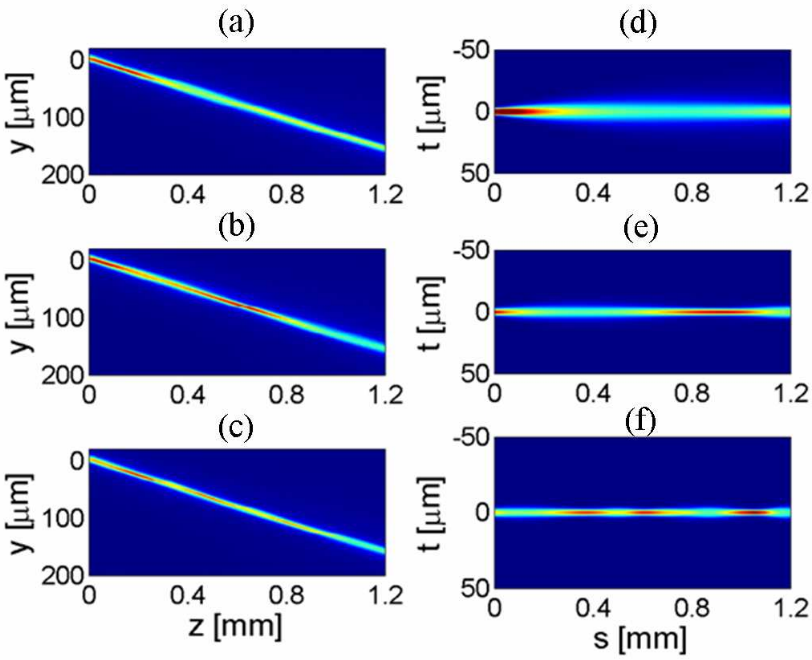

Figure 4.7: Left column: acquired intensities profiles at $633nm$ in the plane yz. Intensity levels are normalized to scattering losses along s. Right column: corresponding numerically computed intensities in the plane st. Input power P_{red} at $633nm$ is $1.6mW$, while IR powers are P_{IR}= 0 (a, b), 0.7 (c, d) and $2.4mW$ (e, f), respectively. In-coupling parameters are as in fig. 4.6.

Finally, the left column of fig. 4.8 shows color-coded maps of the measured peak intensity (normalized to scattering losses) of the red component versus s (horizontal axis) and the total optical power $P = P_{red} + P_{IR}$ (vertical axis) for a fixed input P_{red} at $633nm$. The characteristic breathing of the nonlocal vector soliton is non periodic and changes with total excitation, being more sensitive to the red (i.e., a similar behavior occurs at lower total powers if P_{red} is higher). This is primarily due to the larger anisotropy at $633nm$, i.e., a greater amount of energy coupled with the medium through reorientation, and a deeper refractive well for a given director distribution. The simulations, plotted in the right column for the peak intensity after integration across thickness x and normalization to input power at $633nm$, display the same trend: for a fixed total power P, a larger P_{red} makes the soliton more confined and the breathing periods versus s decreases, in good agreement with the experimental results. The departure between acquired and calculated maps are due to scattering losses as well as beam aberrations caused by a distorted director distribution at the input interface, both effects neglected in the simulations.

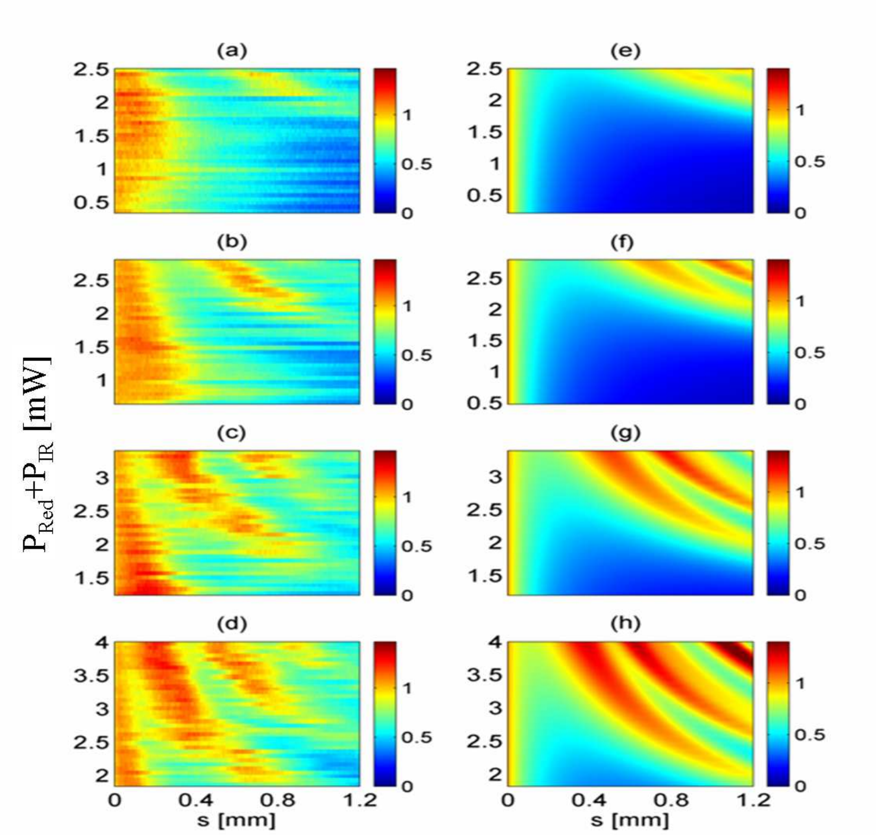

Figure 4.8: Normalized red peak intensity I_{red} in the observation plane st (right axes) versus s and total excitation $P_{red} + P_{IR}$ (left axes) for a fixed P_{red}. (a) thru (d): measured data, (e) thru (h): calculated data (after integration along x) assuming coupling parameters as in fig. 4.6. P_{red} is 0.1 (a, e), 0.4 (b, f), 1.0 (c, g) and $1.6mW$ (d, h), respectively. Both experimental and numerical data are normalized to the value in $s = 0$.

5

Dissipative Self-Confined Optical Beams in Doped Nematic Liquid Crystals

5.1 Gain and Solitary Waves Propagation

Since losses are a detrimental factor in the propagation and use of spatial solitons, the investigation of solitary waves in the presence of dissipative terms, e.g. gain or absorption, was carried out mostly within the context of the complex Ginzburg Landau equation, (99; 100) with attention to the potential applications in lasers (101). In previous chapters I discussed nonlinear optical propagation in undoped nematic liquid crystals; in this chapter I study nonlinear wave propagation when a luminescent dye is added to the NLC, inducing an optical gain. To model dye effects in NLC I will use various models, beginning with the simplest case: a gain dependent neither from signal intensity (gain saturation) nor space coordinates (for example, pump spatial profile). Interestingly, a negative gain can be used to describe the scattering losses, that play an important role in the nematic phase due to the orientational order [see chapter 1 and references (58; 60)]. I will later consider a gain dependent on intensity, i.e. gain saturation, and a gain dependent on pump profile, i.e. varying in space. In every case the optical pump propagates along the x axis [see 5.1(a)]; eventually, I will consider a pump co-propagating with the signal beam; then, I will study the interaction of two solitons at two different wavelengths, i.e. a vectorial soliton (see chapter 4), with power

exchange between them induced by the dye.
I will assume a suitable concentration of dopants in order to obtain the desired gain. Gain and luminescence have been reported in several dye-doped liquid crystals, including nematics (102; 103; 104) cholesterics (105; 106; 107; 108) and blue phases (109) in planar and cylindrical geometries. Results, although referred to a particular class of highly nonlocal nonlinear media such as NLC, are qualitatively valid in all highly nonlocal media where spatial solitons can be generated [see (31) and chapter 3].

5.2 Light Self-Confinement in Dye Doped Nematic Liquid Crystals: Model

I refer to a nematic liquid crystalline cell as sketched in fig. 5.1. Two glass slides sandwich a liquid crystal layer [fig. 5.1(a)] of thickness $d = 100$ μm. I take that, in the absence of an external excitation, the molecular director $\hat{n}$ (i.e., the optic axis) is homogeneously distributed in the sample and lies on the yz plane at an angle θ_0 with the longitudinal z-axis [fig. 5.1(b)]. For the sake of simplicity, I limit my investigation to the case of zero voltage applied across the cell, in order to avoid beam-shift in the xs plane due to birefringent walk-off (47; 81). The latter would require the wave propagation to be treated vectorially. Figure 5.1(c) shows the reference system xts after rotating xyz by the walk-off angle δ around the x-axis. In this way, the versor $\hat{\boldsymbol{s}}$ corresponds to the direction of the Poynting vector. The propagation of extraordinary polarized light in the paraxial approximation along s is governed by a nonlocal nonlinear Schröedinger equation (NNLSE) (see chapter 1)

$$2ik\frac{\partial A}{\partial s} + \nabla_{\perp}^2 A + k_0^2 \Delta n(|A|)A - 2ik_0 n_e \gamma A = 0 \tag{5.1}$$

where A is the slowly-varying envelope of the electric field, n_e the (linear) extraordinary refractive index, k_0 the vacuum wavenumber, $D_{x/t}$ the anisotropic diffraction coefficients, $\gamma \in \mathbb{R}$ the amplitude gain (loss) coefficient and $\delta\epsilon_{tt}$ the nonlinear optical perturbation induced on the dielectric tensor $\boldsymbol{\epsilon}$ via reorientation. The last term takes into account the power exchange between the light beam and the external environment. Clearly, no soliton propagation is admitted by eq. (5.1) due to the lack of a loss (gain) term balancing the gain (loss). Hereafter, I take $\delta\epsilon_{tt} = \epsilon_a \left[\sin^2(\theta - \delta) - \sin^2(\theta_0 - \delta)\right]$, with ϵ_a the optical anisotropy, δ the walk-off angle and θ the angle between the

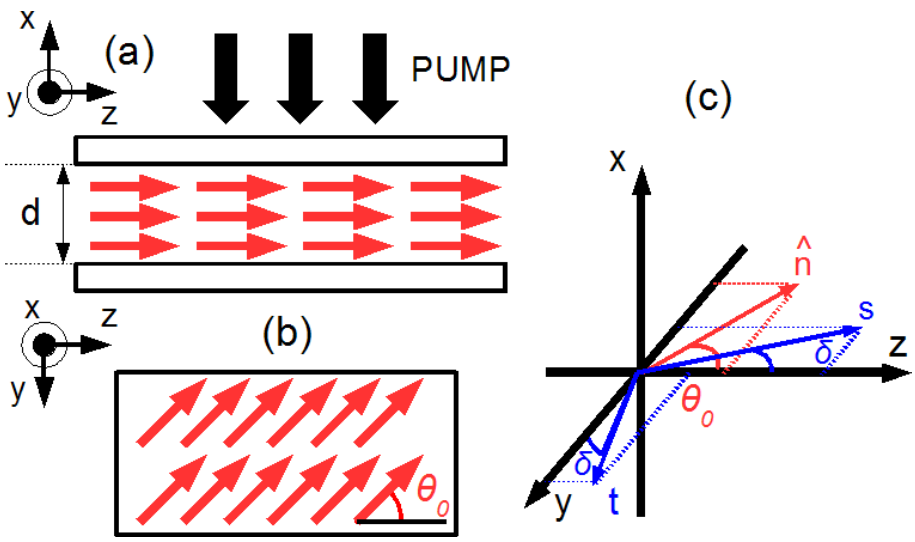

Figure 5.1: Sketch of the un-biased NLC cell geometry: (a) lateral view, (b) top view. The arrows represent the mean molecular direction (NLC *director*). (c) Reference systems xyz and xts: the latter is a rotation of the former around x by the walk-off angle δ; s is the direction of energy flow. In (a) is shown pump direction.

wavevector $\mathbf{k}$ and the director $\hat{n}$ in the presence of an electromagnetic perturbation. This means I neglect other possible nonlinearities, such as the thermo-optic effect (69) and cis-trans transformations (110). Therefore, the reorientational profile of the angle θ is ruled by the Euler-Lagrange equation (chapter 1),

$$K\nabla_{\perp}^{2}\theta + \frac{\epsilon_0\epsilon_{a1}}{4}|A_1|^2 \sin\left[2(\theta - \delta_1)\right] = 0 \tag{5.2}$$

being K the (intermolecular) elastic coefficient in the single constant approximation. While in un-doped NLC γ is mainly determined by scattering losses (absorption being usually negligible in the optical spectrum) and it is negative, if a suitable dye is present and the sample is illuminated by a pump (laser), γ can become positive and introduce amplification. I simulate beam evolution at wavelengths $\lambda = 633$ and $1064nm$ using a nonlinear beam propagator (BPM) (see appendix B for details), using a Gaussian input profile with waist $w = 2.8\mu m$ and assuming $\theta_0 = \pi/6$ (kept constant hereafter). Throughout this chapter, I refer to the physical parameters of the commercial liquid crystal E7 ($K = 12 \times 10^{-12}$N, $n_e = 1.5646$ and $\epsilon_a = 0.7093$ for $\lambda = 633nm$, $n_e = 1.5456$ and $\epsilon_a = 0.6130$ for $\lambda = 1064nm$) and assume a dye-concentration able to activate the NLC at the wavelength of the launched beam.

5.3 Constant Optical Amplification

In the simplest case, γ can be approximated by a constant, i.e., independent from both the spatial coordinates (the spatial distribution of the pump) and the intensity $I \propto |A|^2$ (i.e., no gain saturation). Fig. 5.2 shows a comparison between soliton propagation in undoped NLC [fig. 5.2(a)] and dye-doped NLC [fig. 5.2(a)]: in the latter case the power increases with s; moreover, breathing features are affected by the incremented power. In this example, for $\gamma = 100m^{-1}$ there are four maxima in intensity along s, whereas for zero γ the maxima are only three. To better address this issue (i.e., the breathing behavior versus gain), fig. 5.3 displays the results at $\lambda = 633nm$ for initial beam powers of 0.5, 1.0, 1.5 and $2.0mW$, respectively, plotting the beam waist across t versus propagation s, $w_t(s) = 2\sqrt{\frac{\int I_t(t,s)t^2dt}{\int I_t(t,s)dt}}$, with $I_t(t,s) = \int_0^d |A|^2 dx$ the intensity averaged along x. The quantity w_t is well suited to describe beam (soliton) breathing during amplification (or attenuation if $\gamma < 0$) along s. From the numerical simulations I find that $w_t(s) \cong w_x(s)$ when $w_{x/t}$ are much smaller than d, w_x being the waist across x (fig. 5.3). As predicted for highly nonlocal solitons in undoped media ($\gamma = 0$) (31; 51), the breathing period decreases as the initial power P_{in} increases. Therefore, for a fixed $\gamma \neq 0$, the propagation distance between two waist minima reduces (increases) owing to amplification (attenuation). A finite γ affects the mean beam waist, which reduces (grows) with s for $\gamma > 0$ ($\gamma < 0$). I repeated the calculations at $\lambda = 1064nm$; fig. 5.4 shows the computed waist $w_t(s)$ for $P_{in} = 0.5$ and $2.0mW$: self-confinement is obtained only when the power is large enough to induce self-focusing. Moreover, since diffraction is stronger than in the red (for the same powers), waist oscillation periods are larger than in fig. 5.3 (see chapter 2 for details).

Figure 5.5 shows the beam profile for $\lambda = 633nm$ at $s = 1.5mm$ with $P_{in} = 0.25mW$ and $\gamma = 0$ or $\gamma = 1000m^{-1}$, respectively. In the second case, the gain suffices to enhance the nonlinear confinement and overcome diffraction: indeed, there is a region where the waist begins to decrease. Afterwards, beam width oscillates due to the interplay of nonlinear self-focusing and diffractive spreading.

After the investigation on beam breathing, I discuss the amplification and its relationship with the propagation coordinate s. To this extent, I can define the beam power amplification at a fixed s as $G(s) = P(s)/P_{in}$, i.e. the ratio between the power in s and in $s = 0$. I find that $G(s) = \exp(2\gamma s)$ if the self-induced waveguide has

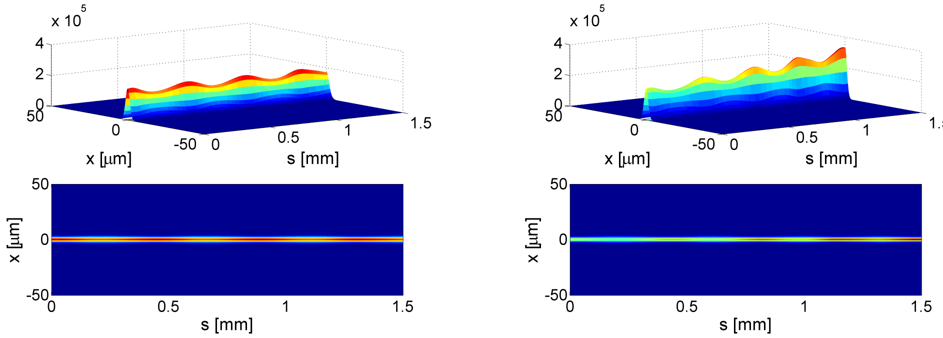

(a) (b)

Figure 5.2: Numerically simulated beam propagation in the cell of fig. 5.1, in the presence of a constant gain γ. Fig. 5.2(a) and 5.2(b) show the results for $\gamma = 0m^{-1}$ (passive medium) and $\gamma = 100m^{-1}$ (active medium), respectively. The input profile is Gaussian with a waist equal to $2.8\mu m$. Wavelength is $633nm$.

a numerical aperture large enough to confine all the input light and prevent losses due to the coupling to the radiation modes. Therefore, at low input powers only part of the excitation gets trapped and G is reduced by a constant factor (i.e. I can write $G(s)|_{P_{in}} = \eta_{coupling}(P_{in}) \exp(2\gamma s)$ with $\eta_{coupling}$ the initial coupling to modes of the self-induced guide, which clearly depends on the initial beam power), whereas above threshold (dependent on wavelength through diffraction), the power amplification reaches a maximum and saturates (i.e. $\eta_{coupling}$ saturates to 1) for large enough P_{in}. Figure 5.6 shows the calculated G versus γ for various input powers at two different wavelengths: the gain is higher and saturates above $P_{in} = 0.5mW$ at $\lambda = 633nm$ [fig. 5.6(a)], while at $\lambda = 1064nm$ it keeps increasing with power [fig. 5.6(b)] until $P_{in} = 3.0mW$ due to the stronger diffraction.

5.4 Role of Gain Saturation

5.4.1 Mechanism for Dye Luminescence: a Simple Model

The simplest way to model optical gain in the interaction between signal, pump and luminescent dye is to consider the dye as a three level system (four level systems are similar but more involved to compute), as in laser theory (111).

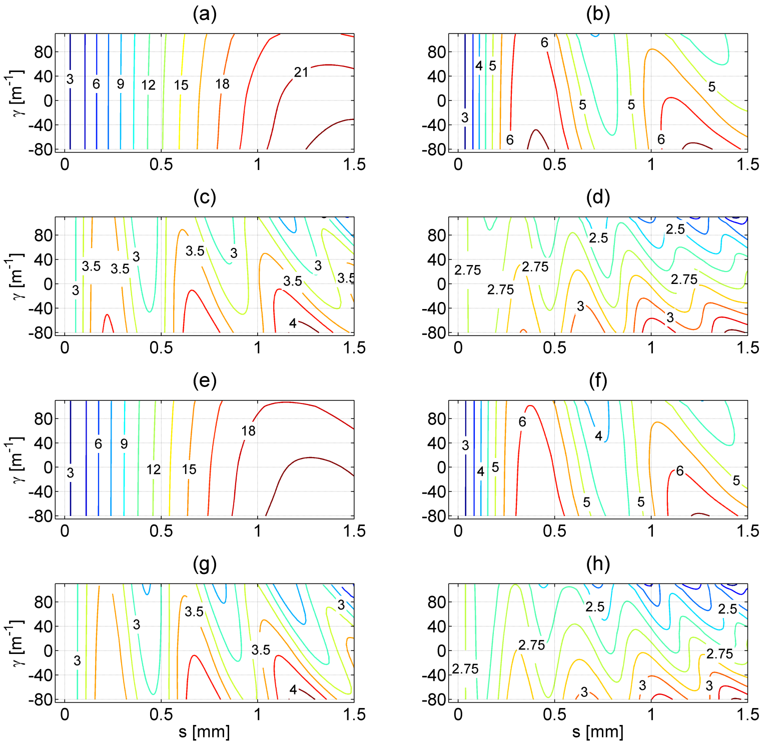

Figure 5.3: Calculated w_t [first and second row, (a)(d)] and w_x [third and fourth row, (e)(h)] versus propagation s and gain or loss γ for $\lambda = 633$nm. The input beam waist is always $2.8\mu m$. Input powers P_{in} are 0.5 (a), (e); 1 (b), (f); 1.5 (c), (g); and 2mW (d), (h), respectively. The resulting self-confined beam is nearly cylindrically symmetric.

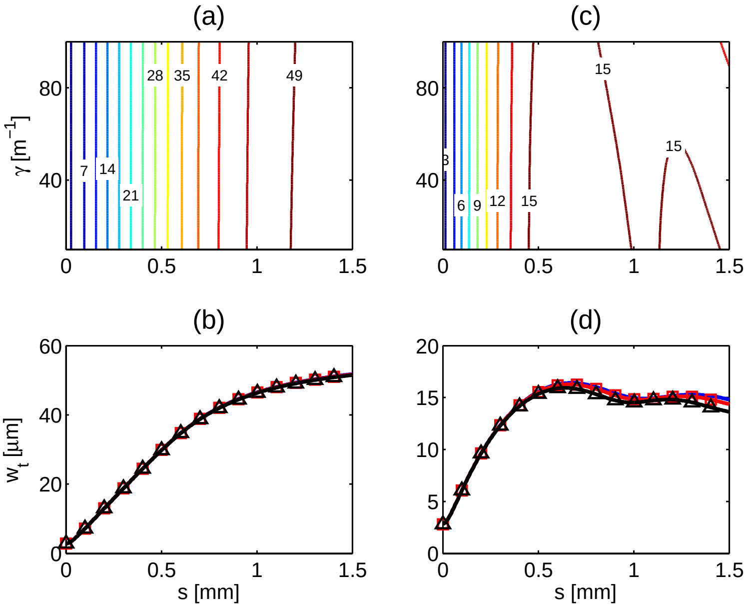

Figure 5.4: Calculated w_t at $\lambda = 1064nm$ for an initial waist of $2.8\mu m$. (a) w_t versus s and gain γ, (b) w_t versus s for $\gamma = 0m^{-1}$ (solid line), $\gamma = 40m^{-1}$ (squares) and $\gamma = 80m^{-1}$ (triangles); the input power P_{in} is $0.5mW$. (c) and (d) Same as in (a) and (b) but for $P_{in} = 2mW$. The waist is larger than at 633nm (fig. 5.3) due to stronger diffraction.

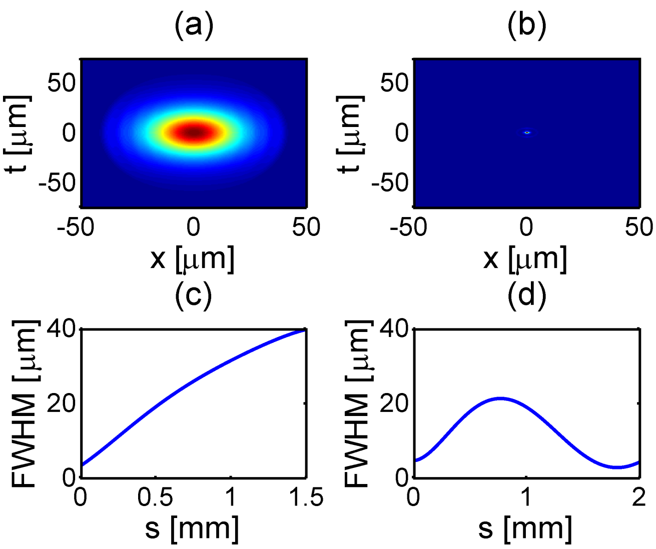

Figure 5.5: Beam profiles at $s = 1.5mm$ for (a) $\gamma = 0m^{-1}$ and (b) $\gamma = 0m^{-1}$ at $\lambda = 633nm$. The input power is 0.25mW, and the input waist is $2.8\mu m$. Beam FWHM versus s for (c) $\gamma = 0m^{-1}$ and (d) $\gamma = 1000m^{-1}$. For zero gain, the beam diffracts (c), while it self-confines (and breathes) in the presence of amplification.

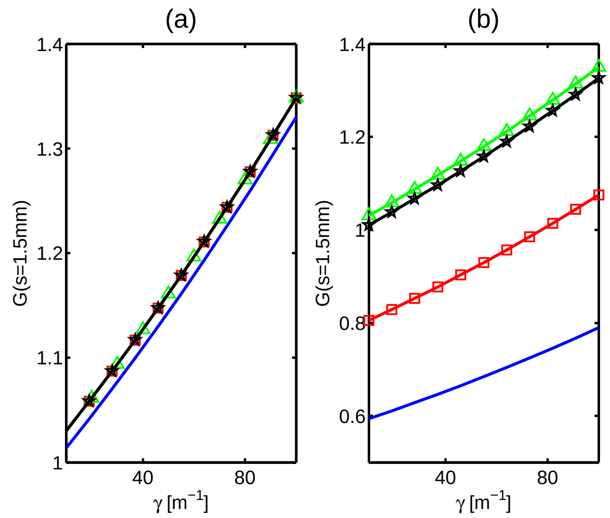

Figure 5.6: Amplification $G(s)$ versus γ in $s = 1.5mm$. Results for (a) $\lambda = 633nm$, (b) $\lambda = 1064nm$. Input powers are 0.5 (solid line), 1.0 (squares), 2.0 (stars) and $4.0mW$ (triangles), respectively.

A diagram of dye energy levels is in fig. 5.7: pump photons allow the molecules to jump from level 1 to 3, followed by a non radiative decay to level 2. Finally, a radiative decay from level 2 to 1 provides photon emission stimulated by the signal. Therefore the signal beam is amplified, if dye is pumped at the appropriate wavelength. From the balance in level population (111) I get

$$n_d \equiv n_2 - n_1 = \frac{A(R) - B}{C(R)I_s + D(R)} N \qquad (5.3)$$

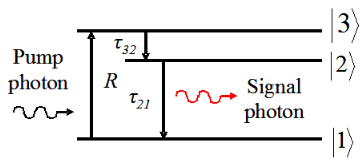

Figure 5.7: Energy diagram of optical gain in a three level system.

n_1 and n_2 being the density populations per unit volume in level 1 and 2, respectively, N the dye density per unit volume, I_s the signal intensity and R the pumping rate $R = \alpha_p I_P$, where I_P and α_P are the pump intensity and its cross-section, respectively. In eq. (5.3) I defined $A(R) \equiv X(R)/\tau_{32}$, $B \equiv 1/\tau_{21}$, $C(R) \equiv \alpha_s[2+X(R)]$, $D(R) \equiv X(R)/\tau_{32} + [1+X(R)]/\tau_{21}$, with $X(R) \equiv R/[R+1/\tau_{32}]$; α_s is the cross-section for the signal. The optical gain γ is related to the population difference n_d by α_s (111), i.e. $\gamma = \alpha_s n_d$. I can rewrite the gain as

$$\gamma = \frac{K(R, N)}{I_s + I_0(R)} \qquad (5.4)$$

having defined $G_0(R,N) = N[A(R){-}B]/C(R)$, $I_0(R) = D(R)/I(R)$ and $K(R,N) = G_0 I_0$. The parameter I_0 depends on the dye density, while K depends also on the

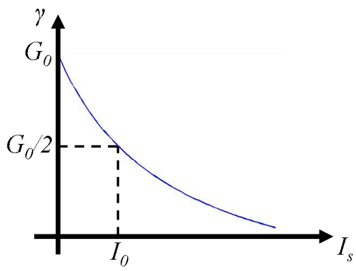

Figure 5.8: Optical gain γ versus signal beam intensity I_s.

pumping rate R. Physically, G_0 represents the optical gain at low intensity, i.e. without saturation, whereas I_0 is the saturation intensity, defined as the value which halves the gain (see fig. 5.8). Finally, I stress that both N and R are design parameters, to be chosen according to the required features.

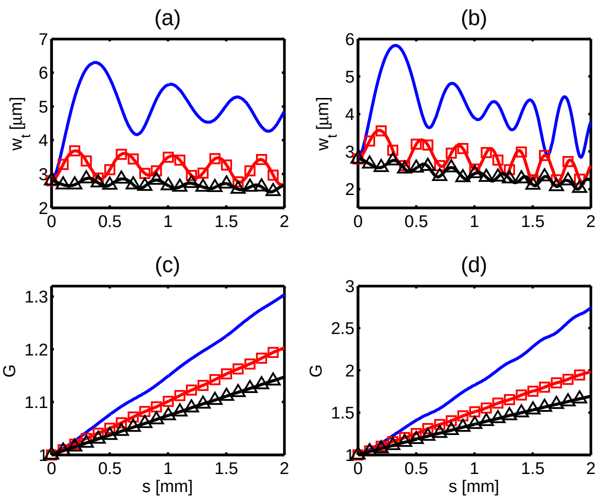

Figure 5.9: Beam waist w_t versus s in the presence of saturable gain for (a) $\gamma_0 = 100$ and (b) $500m^{-1}$ for $P_{in} = 1.0$ (solid line), 1.5 (squares) and $2.0mW$ (triangles). (c) and (d) Amplification G versus s for (c) $\gamma_0 = 100$ and (d) $500m^{-1}$ (correspondence between lines and powers as above). In all cases $I_0 = 1.8 \times 10^{10} W m^{-2}$.

5.4.2 Gain Saturation: Numerical Analysis

I numerically investigate the effects of a gain γ dependent on the intensity I by assuming $\gamma = \gamma_0/(1 + I/I_0)$ [eq. (5.4)], the latter being able to model saturation in a three or four level system [such as NLC doped with luminescent dyes, where both γ_0 and I_0 are related to pumping rate and dye concentration (102; 103; 104)(section 5.4.1)]. Figure 5.9 shows the calculated w_t for $\gamma_0 = 100$ and $500m^{-1}$, for three values of P_{in} (1.0, 1.5 and $2.0mW$) and I_0 fixed at $1.8 \times 10^{10}W/m^2$. Similar to the case of a constant γ, for a given input power the soliton oscillation period and mean waist decrease as γ_0 becomes larger. Note that, as $w_x(w_t)$ departs from the soliton existence curve $w = w(P, w_{in})$, the beam oscillates aperiodically. The amplification G has an exponential behavior versus s if powers are very low (no saturation, not shown), but shows a quasi-linear trend at high powers [figs. 5.9(c) and 5.9(d)], with slopes getting lower and lower as P_{in} increases, due to the saturation.

Figure 5.10 plots amplification G computed at $s = 2mm$ versus P_{in} for two different I_0, γ_0 being fixed at $100m^{-1}$. The curves have a maximum due to the interplay between diffraction (stronger at lower power) and gain with saturation: at low power the gain raises owing to a better guidance in the self-induced index well (fig. 5.6), whereas for higher powers a gain reduction due to the saturation sets the amplification behavior. The maximum G, occurring at the balance of the two described effects, rises and shifts towards high powers for larger I_0, as predictable; eventually, amplification is stronger for larger I_0, keeping fixed γ_0.

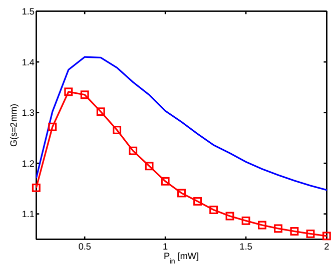

Figure 5.10: Soliton amplification G at $s = 2mm$ versus input power P_{in} for $\gamma_0 = 100m^{-1}$ and $I_0 = 1.8 \times 10^{10}Wm^{-2}$ (solid line) or $I_0 = 3.6 \times 10^9Wm^{-2}$ (squares).

5.5 Role of the Pump Profile

Now I consider the effect of a space-dependent gain γ due to a spatial dependence of the dye density N or of the pumping rate R; the last case, for example, can be determined by the pump profile, being $R = \alpha_p I_p$ (section 5.4.1). I take a Gaussian pump [e.g. illuminating the cell from above with a laser beam, see fig. 5.1(a)] of the form $\gamma = \gamma_0 \exp\left\{-\left[(t/w_{Pt})^2 + (s-s_P)^2/w_{Ps}^2\right]\right\}$. As characteristic of highly nonlocal systems, the propagating beam remains nearly Gaussian (31; 112) but the amplification $G(s)$ depends on the spatial superposition between pump and soliton, i.e., $G(s) = \exp(2\eta\gamma_0 s)$, with $\eta < 1$ being an overlap integral. As a consequence, $G(s)$ can exhibit small deviations from the exponential form, owing to the soliton breathing, i.e., a varying η. For instance, fig. 5.11(a) shows the case of an infinitely extended pump along s, i.e., $w_{Ps} \to \infty$, and $w_{Pt} = 2\mu m$: the differential amplification dG/ds depends on the overlap between signal and pump. Note that the maxima in dG/ds and the pump are slightly offset due to the overall amplification, i.e. by varying the beam power with s the overlap integral has an additional dependence from the amplitude of the signal. Figure 5.11(b) shows the results for $s_P = 0.75mm$ and $w_{Ps} = 500\mu m$: the differential gain is determined by both the pump profile and the overlap dependence on signal breathing.

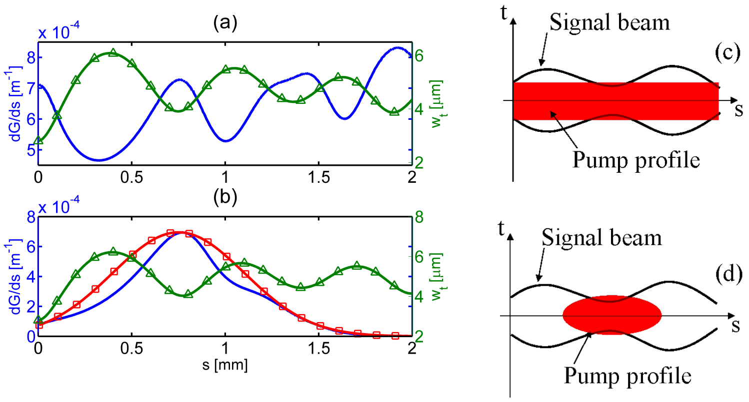

Figure 5.11: Differential gain dG/ds for (a) $P_{in} = 1mW$, $\lambda = 633nm$, $w_{Ps} \to \infty$, $w_{Pt} = 2\mu m$ and $\gamma_0 = 100m^{-1}$ (solid line with no symbols) and beam waist w_t (line with triangles) versus s. (b) As in (a) but for $w_{Ps} = 500\mu m$ and a pump centered in $s = 0.75mm$. The pump profile is shown for comparison (line with squares). In (c) and (d) are shown the schematic for the pump profile (in red) and for the signal beam (black curves) corresponding to (a) and (b), respectively.

5.6 Co-Propagating Pump

In this last section I analyze the behavior of a dye doped NLC when two beams of different wavelengths are launched inside the medium, supposing that the two frequencies are such that the shortest wavelength acts as a pump for the other, i.e. a co-propagating pump (see section 5.1). From chapter 4 and eq. (5.1), the optical propagation is modeled by

$$\begin{aligned} 2ik_{01}n_{e1}\cos\delta_1\frac{\partial A_1}{\partial s}+D_{t1}\frac{\partial^2 A_1}{\partial t^2}+D_{x1}\frac{\partial^2 A_1}{\partial x^2}+k_{01}^2\delta\epsilon_{tt1}A_1-2ik_{01}n_{e1}\gamma_1 A_1=0\\ 2ik_{02}n_{e2}\cos\delta_2\frac{\partial A_2}{\partial s}+D_{t2}\frac{\partial^2 A_2}{\partial t^2}+D_{x2}\frac{\partial^2 A_2}{\partial x^2}+k_{02}^2\delta\epsilon_{tt2}A_2-2ik_{02}n_{e2}\gamma_2 A_2=0 \end{aligned} \tag{5.5}$$

where I took two collinear Poynting vectors for the two waves (see chapter 4) and suffix 1(2) indicates the shorter (larger) wavelength, i.e., beam 1 is the pump. Invoking photon number conservation in the infinitesimal volume dV centered in $\mathbf{r}$ and considering a stationary condition (no change in time), I can write $d\Phi_1/ds + d\Phi_2/ds = 0$, where Φ_1 and Φ_2 are fluxes of photons in dV for pump and signal fields, respectively; therefore, $d\Phi_1$ ($d\Phi_2$) are the pump (signal) photons absorbed (emitted) between s and $s + ds$, having assumed that every absorbed pump photon produces a signal photon, i.e. a unitary efficiency through the mechanism illustrated in section 5.4.1. According to (5.5) it is $dI_j/ds = 2\gamma_j I_j$ ($j = 1, 2$), thus I obtain

$$\gamma_2 = -\frac{I_1}{I_2}\frac{f_2}{f_1}\gamma_1 \tag{5.6}$$

where f_j ($j = 1, 2$) are the beam frequencies and I used $I \propto \Phi$. I take γ_1 constant for the sake of simplicity. From eq. (5.6) the signal gain is proportional to the pump absorption γ_2 and depends on the ratio between pump and signal intensities, respectively; thus, the signal undergoes an amplification variable in space, similarly to section 5.5, but with a gain variation in the transverse plane xt, as well. A multiplicative coefficient, given by ratio between the two electromagnetic frequencies, limits the available gain.

Fig. 5.12 shows typical numerical results: power is transferred from pump to signal by means of the dye. This process ends when the pump intensity becomes too low to allow population inversion in the dye molecules.

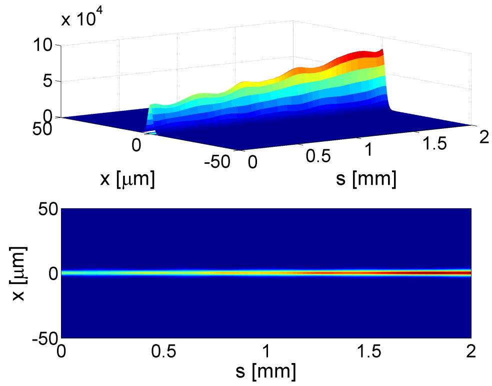

(a) $\lambda = 633nm$

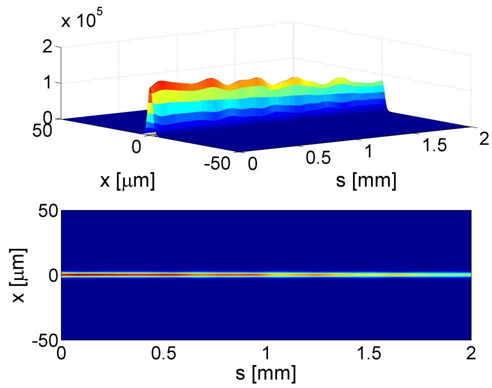

(b) $\lambda = 532nm$

Figure 5.12: Example of co-propagating pumping. In 5.12(a)[5.12(b)] is reported the behavior of signal(pump) field at $633nm$($532nm$) on the plane xs. Initial waist is $2.8\mu m$ for both beams and power is $0.3mW$ and $1mW$ for $\lambda = 633nm$ and $\lambda = 1064nm$, respectively.

6

Conclusions

In this thesis I have analyzed several aspects of nonlinear light propagation in nonlocal media, with particular reference to NLC. I studied nonlinear optical propagation of single beams in NLC, showing experimentally solitons and their readdressibility with applied bias for a fixed input polarization using a new geometry for the input interface. I theoretically investigated nonlinear light propagation in NLC, focusing on soliton profiles and breathing. The results are qualitatively valid in all highly nonlocal media. I addressed the role of boundaries in soliton propagation in nonlocal media, demonstrating that, in finite size sample, a force due to the nonlinear index well is exerted on the beam, with a related motion depending on power. Two-color solitons in NLC have been demonstrated for the first time, addressing the interaction between the two components and reaching an excellent agreement between experiments and theory. Such results are relevant to the study of the properties of optically-written guides in any kind of nonlocal media. I also studied dye-doped NLC and the effects of light amplification on soliton propagation, being these results useful for the future design of lasers based on light self-confinement, a very intriguing issue due to the peculiar properties of the material and its unique tunability.
All of these results are useful in the design of devices for the all-optical signal processing, from all-optical switching to demultiplexing and routing.

Appendix A

Optical Properties of NLC

A.1 Scattering in a NLC Cell

From eq. (1.11), when a plane wave polarized along $\hat{\boldsymbol{i}}$ propagates inside a liquid crystalline medium, the differential cross section for the scattered light around $\hat{\boldsymbol{k}}_{out}$ is given by

$$\frac{d\sigma}{d\Omega} = \left(\frac{\epsilon_a k_0^2}{4\pi}\right) \langle |n_\eta(\mathbf{q})|^2 \rangle \sum_{\mu=1,2} \left[\left(\hat{\boldsymbol{i}} \cdot \hat{\boldsymbol{a}}_\mu\right) \left(\hat{\boldsymbol{f}} \cdot \hat{\boldsymbol{n}}\right) + \left(\hat{\boldsymbol{i}} \cdot \hat{\boldsymbol{n}}\right) \left(\hat{\boldsymbol{f}} \cdot \hat{\boldsymbol{a}}_\mu\right) \right]^2 \tag{A.1}$$

being $\mathbf{k}_{out}$ the scattered field wavevector.

My objective is to compute the optical power scattered by the NLC along $\hat{\boldsymbol{x}}$ (i.e. $\hat{\boldsymbol{k}}_{out} = k_0 \hat{\boldsymbol{x}}$) for the cell sketched in fig. 2.1, in order to understand the scattering behavior for different applied biases, when ordinary or extraordinary waves are launched.

Assuming equal moduli for incident and scattered wavevectors (i.e., neglecting the index differences due to anisotropy), I have $\mathbf{q} \approx k_0 \frac{\sqrt{2}}{2}(\hat{\boldsymbol{x}} + \hat{\boldsymbol{z}})$. Electric field polarizations for o and e components are $\hat{\boldsymbol{e}}_o$ and $\hat{\boldsymbol{e}}_e$, respectively. From section 2.4

$$\hat{\boldsymbol{e}}_0(\mathrm{V}) = \cos\left[\varphi(\mathrm{V})\right] \hat{\boldsymbol{x}} - \sin\left[\varphi(\mathrm{V})\right] \hat{\boldsymbol{y}} \tag{A.2}$$

$$\hat{\boldsymbol{e}}_e(\mathrm{V}) = \frac{\epsilon^{-1} \cdot \boldsymbol{d_e}\hat{(}\mathrm{V})}{|\epsilon^{-1} \cdot \hat{\boldsymbol{d}}_e(\mathrm{V})|} \tag{A.3}$$

where $\varphi(V) = \arctan[\tan(\xi_{max})/\cos(\theta_0)]$ (see section 2.3 for the definition of ξ_{max}) and $\hat{\boldsymbol{d}}_e(\mathrm{V}) = \sin\left[\varphi(\mathrm{V})\right] \hat{\boldsymbol{x}} + \cos\left[\varphi(\mathrm{V})\right] \hat{\boldsymbol{y}}$ is the polarization of the extraordinary electric displacement field (see figure 2.3 for the definition of φ). The dielectric tensor ϵ is evaluated using the director direction in the cell mid-plane, which depends on V as well.

To assess the power scattered parallel to $\hat{\boldsymbol{x}}$, I have to integrate (A.1) over all the possible polarizations for the scattered field, i.e. to take into account the contributions stemming from every $\hat{\boldsymbol{f}}$ lying in the plane yz. Furthermore, I have to substitute the versor $\hat{\boldsymbol{\imath}}$ with $\hat{\boldsymbol{e}}_e$ ($\hat{\boldsymbol{e}}_o$) when I compute the power scattered from the extraordinary (ordinary) component.

Results are shown in fig. A.1 for a wavevector and $\hat{\boldsymbol{n}}$ forming an angle equal to $\pi/4$ at V $= 0$. In absence of an applied bias, the scattered powers are equal, whereas when V is increased, extraordinary scattering is enhanced and the ordinary one reduced, becoming null for V $> 3V$. In practice, at high V the scattering from the ordinary polarization is mainly due to the multiple scattering.

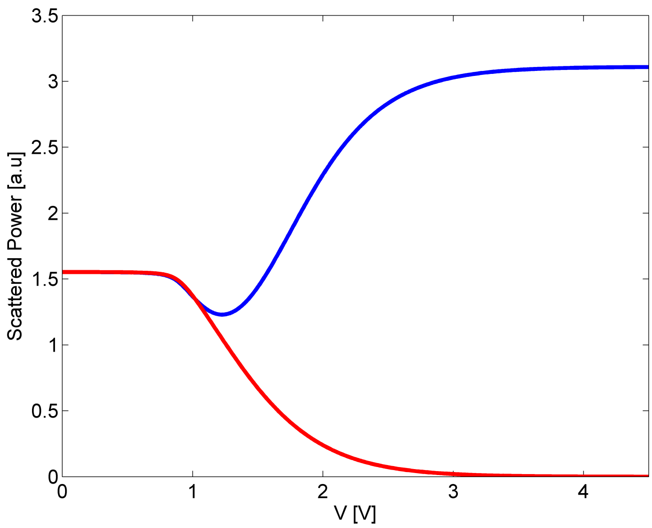

Figure A.1: Scattered power versus applied bias V when all the input power is coupled into ordinary (red line) or extraordinary (blue line) polarizations.

A.2 Derivation of the Electromagnetic Ruling Equation in NLC

In a generic non magnetic anisotropic uniaxial medium, the electric field obeys the equation

$$\nabla \times [\nabla \times \mathbf{E}] = \nabla(\nabla \cdot \boldsymbol{E}) - \nabla^2 \boldsymbol{E} = k_0^2 \boldsymbol{\epsilon}(\boldsymbol{r}) \cdot \boldsymbol{E} \quad (A.4)$$

where the dielectric tensor components for a liquid crystal are given by (58; 60) $\epsilon_{ij} = \epsilon_\perp \delta_{ij} + \epsilon_a n_i n_j$, with δ the Kronecker delta, n_j the j-th component of the director $\hat{\boldsymbol{n}}$, $\epsilon_\perp$ and $\epsilon_\parallel$ the dielectric constant values normal and parallel to the optic axis, respectively, and $\epsilon_a = \epsilon_\parallel - \epsilon_\perp$ the dielectric anisotropy.

I consider the wavevector along z by writing $E = Ae^{ik_0 n_e z}$; if A is a constant the solution is a plane wave and I can define the tensorial operator $\mathbf{L}(n_e)$ as

$$\mathbf{L}(n_e) \cdot \mathbf{A} \equiv \left[n_e^2 (\hat{\boldsymbol{z}}\hat{\boldsymbol{z}} - \mathbf{I}) + \boldsymbol{\epsilon} \right] \cdot \mathbf{A} = 0 \quad (A.5)$$

where the last equivalence stems from eq. (A.4) and $\mathbf{I}$ is the identity matrix. As well known, in uniaxial media, given a certain propagation direction, there are two plane wave eigensolutions, ordinary and extraordinary waves. Being the ordinary polarization normal to the optic axis, it is subjected to the Freedericksz transition and, for low enough powers, cannot induce reorientation and related nonlinearities. For this reason hereafter I take into account only the extraordinary component. The effect of reorientation is to perturb the dielectric tensor such way that $\boldsymbol{\epsilon} = \boldsymbol{\epsilon_0} + \eta^2 \delta\boldsymbol{\epsilon}$, where $\boldsymbol{\epsilon_0}$ is the unperturbed dielectric tensor taken uniform in absence of an electromagnetic field, and $\delta\boldsymbol{\epsilon}$ is its nonlinear variation. η is a *smallness* parameter, set to unity at the end of the derivation. I write the electric field in the reference system xts as

$$\mathbf{E} = \left[\hat{\boldsymbol{t}} E_e + \eta \mathbf{F_e} + \eta^2 \mathbf{G_e} + o(\eta^3) \right] e^{ik_0 n_e z_0} \quad (A.6)$$

where E_e, $\mathbf{F_e}$ and $\mathbf{G_e}$ depend on multiple slow scales defined by $\mathbf{r} = \mathbf{r}_0 + \eta \mathbf{r_1} + \ldots + \eta^n \mathbf{r}_n$, being $\mathbf{r} = x\hat{\boldsymbol{x}} + t\hat{\boldsymbol{t}} + s\hat{\boldsymbol{s}}$. Moreover, from the former expansion for the position vector I get $\nabla = \nabla_0 + \eta\nabla_1 + \ldots + \eta^n\nabla_n$. Substituting into eq. (A.4) I have

$$(\nabla_0 + \eta\nabla_1 + \ldots) \times \left\{(\nabla_0 + \eta\nabla_1 + \ldots) \times \left[\left(\hat{\boldsymbol{t}}E_e + \eta\mathbf{F_e} + \eta^2\mathbf{G_e} + \ldots\right) e^{ik_0 n_e z_0}\right]\right\} = k_0^2 \left(\boldsymbol{\epsilon_0} + \eta^2\delta\boldsymbol{\epsilon}\right) \left(\hat{\boldsymbol{t}}E_e + \eta\mathbf{F_e} + \eta^2\mathbf{G_e} + \ldots\right) e^{ik_0 n_e z_0} \tag{A.7}$$

At order $o(\eta)$ I have the relationship

$$\left(\nabla_0 \times \nabla_0 - k_0^2\boldsymbol{\epsilon}\right) \mathbf{F_e} e^{ik_0 n_e z_0} + \nabla_0 \times \left[\nabla_1 \times \left(\hat{\boldsymbol{t}}E_e e^{ik_0 n_e z_0}\right)\right] + \nabla_1 \times \left[\nabla_0 \times \left(\hat{\boldsymbol{t}}E_e e^{ik_0 n_e z_0}\right)\right] = 0 \tag{A.8}$$

E_e does not depend on the *slowly varying scale* x_0, t_0, s_0, because in the limit $\eta \to 0$ the solution must dovetail to the plane wave of the linear case. Furthermore, F_e does not depend on x_0, t_0, s_0 because at the slower scale the electric field has to remain unchanged. Eq. (A.8) becomes

$$k_0^2\mathbf{L}(n_e) \cdot \mathbf{F_e} = ik_0 n_e \left\{\hat{\boldsymbol{z}} \times \left[\nabla_1 \times \left(\hat{\boldsymbol{t}}E_e\right)\right] + \nabla_1 \times \left[\hat{\boldsymbol{z}} \times \left(\hat{\boldsymbol{t}}E_e\right)\right]\right\} \tag{A.9}$$

Remembering $\hat{\boldsymbol{z}} = s\cos\delta + t\sin\delta$ eq. (A.9) yields

$$k_0^2\mathbf{L}(n_e) \cdot \mathbf{F_e} = ik_0 n_e \left[-2\cos\delta\frac{\partial E_e}{\partial s_1}\hat{\boldsymbol{t}} + \sin\delta\frac{\partial E_e}{\partial x_1}\hat{\boldsymbol{x}} + \left(\cos\delta\frac{\partial E_e}{\partial t_1} - \sin\delta\frac{\partial E_e}{\partial s_1}\right)\hat{\boldsymbol{s}}\right] \tag{A.10}$$

From its definition versor $\hat{\boldsymbol{t}}$ is an eigenvalue of operator $\mathbf{L}(n_e)$ with eigenvalue zero, thus the solvability condition for eq. (A.10) is $k_0^2\hat{\boldsymbol{t}} \cdot [\mathbf{L}(n_e) \cdot \mathbf{F}_e] = 0$ that, by means of (A.10), becomes

$$\frac{\partial E_e}{\partial s_1} = 0 \tag{A.11}$$

At order $o(\eta^2)$ I get

$$\nabla_0 \times \left[\nabla_0 \times \left(\mathbf{G_e} e^{ik_0 n_e z_0}\right)\right] + \nabla_0 \times \left[\nabla_1 \times \left(\mathbf{F_e} e^{ik_0 n_e z_0}\right)\right] + \nabla_1 \times \left[\nabla_0 \times \left(\mathbf{F_e} e^{ik_0 n_e z_0}\right)\right] + \\ + \nabla_0 \times \left[\nabla_2 \times \left(\hat{\boldsymbol{t}}E_e e^{ik_0 n_e z_0}\right)\right] + \nabla_2 \times \left[\nabla_0 \times \left(\hat{\boldsymbol{t}}E_e e^{ik_0 n_e z_0}\right)\right] = \\ k_0^2\boldsymbol{\epsilon} \cdot \mathbf{G_e} e^{ik_0 n_e z_0} + k_0^2\delta\boldsymbol{\epsilon} \cdot \left(\hat{\boldsymbol{t}}E_e\right) e^{ik_0 n_e z_0} - \nabla_1 \times \left[\nabla_1 \times \left(\hat{\boldsymbol{t}}E_e e^{ik_0 n_e z_0}\right)\right] \tag{A.12}$$

Being G_e independent from $\mathbf{r}_0$, (A.12) turns into

$$k_0^2\mathbf{L}(n_e)\cdot\mathbf{G_e} = -k_0^2\delta\boldsymbol{\epsilon}\cdot\left(\hat{\boldsymbol{t}}E_e\right) + ik_0n_e\left\{\hat{\boldsymbol{z}}\times\left[\nabla_1\times\mathbf{F}_e\right]+\nabla_1\times\left[\hat{\boldsymbol{z}}\times\mathbf{F}_e\right]\right\}+ \\ \nabla_1\times\left[\nabla_1\times\left(\hat{\boldsymbol{t}}E_e\right)\right]+ik_0n_e\left\{\nabla_2\times\left[\hat{\boldsymbol{z}}\times\left(\hat{\boldsymbol{t}}E_e\right)\right]+\hat{\boldsymbol{z}}\times\left[\nabla_2\times\left(\hat{\boldsymbol{t}}E_e\right)\right]\right\} \tag{A.13}$$

Then, the solvability condition is

$$k_0^2\hat{\boldsymbol{t}}\cdot\left[\mathbf{L}(n_e)\cdot\mathbf{G}_e\right]=0 \tag{A.14}$$

Substituting eq. (A.13) into eq. (A.14) I derive

$$-k_0^2\hat{\boldsymbol{t}}\cdot\delta\boldsymbol{\epsilon}\cdot\hat{\boldsymbol{t}}E_e + ik_0n_e\left\{\hat{\boldsymbol{z}}\times\left[\nabla_1\times\mathbf{F}_e\right]+\nabla_1\times\left[\hat{\boldsymbol{z}}\times\mathbf{F}_e\right]\right\}\cdot\hat{\boldsymbol{t}}+ \\ \nabla_1\times\left[\nabla_1\times\left(\hat{\boldsymbol{t}}E_e\right)\right]\cdot\hat{\boldsymbol{t}}++ik_0n_e\left\{\nabla_2\times\left[\hat{\boldsymbol{z}}\times\left(\hat{\boldsymbol{t}}E_e\right)\right]+\hat{\boldsymbol{z}}\times\left[\nabla_2\times\left(\hat{\boldsymbol{t}}E_e\right)\right]\right\}\cdot\hat{\boldsymbol{t}}=0 \tag{A.15}$$

I want to transform eq. (A.15) so that only the component E_e appears, i.e., I need F_e expressed as function of E_e and its derivatives. Setting the solvability condition eq. (A.11) into (A.10) I get

$$k_0^2\mathbf{L}(n_e)\cdot\mathbf{F_e} = ik_0n_e\left[\sin\delta\frac{\partial E_e}{\partial x_1}\hat{\boldsymbol{x}}+\cos\delta\frac{\partial E_e}{\partial t_1}\hat{\boldsymbol{s}}\right] \tag{A.16}$$

Since components along the t direction are lacking, the problem of finding F_e from (A.16) is bidimensional. Defining a new tensorial operator $\mathbf{T}$ in the plane xs as

$$\mathbf{T}=\begin{pmatrix}-n_e^2+\epsilon_\perp & 0\\ 0 & -n_e^2\sin^2\delta+\epsilon_\perp+\epsilon_a\cos^2(\theta-\delta)\end{pmatrix}=\begin{pmatrix}\lambda_x & 0\\ 0 & \lambda_s\end{pmatrix} \tag{A.17}$$

and using (A.5), eq. (A.16) modifies into

$$\mathbf{F}_e=\frac{in_e}{k_0}\mathbf{T}^{-1}(n_e)\cdot\left[\sin\delta\frac{\partial E_e}{\partial x_1}\hat{\boldsymbol{x}}+\cos\delta\frac{\partial E_e}{\partial t_1}\hat{\boldsymbol{s}}\right] \tag{A.18}$$

Substitution of eq. (A.18) into (A.15) yields

$$-k_0^2\delta\epsilon_{tt}E_e-\frac{n_e^2\sin^2\delta}{\lambda_x}\frac{\partial^2E_e}{\partial x_1^2}-\frac{n_e^2\cos^2\delta}{\lambda_s}\frac{\partial^2E_e}{\partial t_1^2}-\frac{\partial^2E_e}{\partial x_1^2}-2ik_0n_e\cos\delta\frac{\partial E_e}{\partial s_1}=0 \tag{A.19}$$

Finally, performing the limit $\eta \to 1$ and defining $D_x = 1 + \frac{n_e^2 \sin^2\delta}{\lambda_x}$, $D_t = \frac{n_e^2 \cos^2\delta}{\lambda_s}$ and $\delta\epsilon_{tt} = \hat{\boldsymbol{t}} \cdot \boldsymbol{\epsilon} \cdot \hat{\boldsymbol{t}}$ I can write (47; 52)

$$2ik_0 n_e \cos\delta \frac{\partial E_e}{\partial s} + D_t \frac{\partial^2 E_e}{\partial t^2} + D_x \frac{\partial^2 E_e}{\partial x^2} + k_0^2 \delta\epsilon_{tt} E_e = 0 \qquad \text{(A.20)}$$

Equation (A.20) is the sought equation which governs extraordinary wave propagation in NLC, in the limit of low optical powers.

Appendix B

Numerical Algorithm

B.1 Simulations of Nonlinear Optical Propagation in NLC

My purpose is to numerically simulate the PDE system given by (2.18), here rewritten

$$2ik_0 n_e \cos\delta \frac{\partial E_e}{\partial s} + D_t \frac{\partial^2 E_e}{\partial t^2} + D_x \frac{\partial^2 E_e}{\partial x^2} + k_0^2 \epsilon_a \left[\sin^2(\theta - \delta) - \sin^2(\theta_0 - \delta)\right] E_e = 0 \tag{B.1}$$

$$K \nabla_{xt}^2 \theta + \frac{\epsilon_0 \epsilon_a}{4} \sin\left[2(\theta - \delta)\right] |E_e|^2 = 0 \tag{B.2}$$

Eqs. (B.1) and (B.2) rule optical nonlinear propagation and director reorientation in NLC, respectively. My integration scheme works as follows: I compute the θ distribution at the input plane through eq. (B.2), with $E_e(x, t, s = 0)$ known because its profile is determined by the specific input beam. From the knowledge of $\theta(x, t, s = 0)$, I can easily compute the nonlinear refractive index, given by $\epsilon_a \left[\sin^2(\theta - \delta) - \sin^2(\theta_0 - \delta)\right]$, in the same plane. Afterwards, I can use eq. (B.1) to find how the optical field E_e propagates until $s = \Delta s$, being Δs the integration step along s (in this way I neglect reflections along s, see sections B.1.1 for further details.). I can repeat the same set of operations for the plane $s = \Delta s$ and, iterating the procedure, it is straightforward to find the beam profile in a zone as long as I wish. Now I discuss the single algorithm implemented in C++ to solve the single equations.

B.1.1 Optical Equation

To solve the optical equation I implemented a beam propagation method (BPM) that allows to compute the field distribution from an input field, neglecting reflections in propagation[1]. A splitting method (113) was applied to solve the initial value problem of equation (B.1). Rewriting eq. (B.1) in order to isolate the operator governing the evolution along s, I get

$$\frac{\partial E_e}{\partial s} = L_t E_e + L_x E_e + L_{\Delta n} E_e = L E_e \tag{B.3}$$

where I defined the operators $L_t = i\frac{D_t}{2k_0 n_e \cos\delta}\frac{\partial^2}{\partial t^2}$ (diffraction along t), $L_x = i\frac{D_x}{2k_0 n_e \cos\delta}\frac{\partial^2}{\partial x^2}$ (diffraction along x), $L_{\Delta n} = i\frac{k_0}{2n_e \cos\delta}\delta\epsilon_{tt}$ (index-well action) and $L = L_t + L_x + L_{\Delta n}$. Formally, the solutions of (B.3) in the interval $[s\ s+\Delta s]$ can be written as $E_e(s+\Delta s) = e^{i\Delta s L}E_e(s) = e^{i\Delta s L_t}e^{i\Delta s L_x}e^{i\Delta s L_{\Delta n}}E_e(s)$. Let me consider the three equations

$$\frac{\partial E_e}{\partial s} = L_t E_e \tag{B.4}$$
$$\frac{\partial E_e}{\partial s} = L_x E_e \tag{B.5}$$
$$\frac{\partial E_e}{\partial s} = L_{\Delta n} E_e \tag{B.6}$$

and assume that an exact or approximated method is available to solve each equation in the interval $[s\ s+\Delta s]$, i.e., there are three discretized operators U_j $(j = t, s, \Delta n)$ such that

$$E_e(s+\Delta s) = U_j(s+\Delta s, s)E_e(s) \tag{B.7}$$

For a small enough propagation step[2] I get that a correct numerical solutions of eq. (B.3) in the interval $[s\ s+\Delta s]$ is (113)

$$E_e(s+\Delta s) = U_{\Delta n}(s+\Delta s, s)U_x(s+\Delta s, s)U_t(s+\Delta s, s)E_e(s) \tag{B.8}$$

[1] The nonlinear index variations I study are small, thereby this condition is satisfied.

[2] The step must be chosen empirically; in particular, I have run numerical simulations for several Δs: the accuracy is sufficient when the solutions become independent from the employed propagation step.

In my case, $L_{\Delta n}$ is exactly solvable, and I easily get $U_{\Delta n}(s+\Delta s, s) = e^{i\Delta s \frac{k_0}{2n_e \cos\delta}\delta\epsilon_{tt}}$. Instead, to solve diffraction operators L_x and L_t I use a finite difference (FD) method, the Crank-Nicolson, which is always stable (113).
Let me take as an example L_x, being the solution procedure for L_t absolutely similar. I have to solve the tridiagonal linear system composed by

$$E_{e_{n,l}}^{m+1} - E_{e_{n,l}}^{m} = i\frac{D_t}{2k_0 n_e \cos\delta}\frac{\Delta s}{2\Delta t^2}\left[E_{e_{n+1,l}}^{m} + E_{e_{n-1,l}}^{m} - 2E_{e_{n,l}}^{m} + E_{e_{n+1,l}}^{m+1} + E_{e_{n-1,l}}^{m+1} - 2E_{e_{n,l}}^{m+1}\right] \tag{B.9}$$

being $E_{e_{n,l}}^{m} = E_e(t = n\Delta t, x = l\Delta x, s = m\Delta s)$, and Δt and Δx the numerical steps along t and x, respectively. At the edges of the numerical grid, I must define the appropriate boundary conditions: in particular, I neglect reflections at the interfaces between glass and NLC, therefore I have to simulate an infinitely extended medium. Two different kinds of boundary conditions were applied to this extent: absorbing boundary condition (ABC) (114) and transparent boundary conditions (TBC) (115). In the ABC case I multiply the beam at every step for a physical absorber, sufficiently lossy to adsorb the outgoing waves but with a sufficiently smooth profile to prevent spurious reflections. In the TBC case, the field values at the grid boundaries are chosen so that they match the diffractive outgoing waves.
TBC have the advantage of being independent from the specific excitation, thereby the results are the same when light is self-localized, being the radiated power very low. Some slight differences appear when I simulate the linear behavior, with the TBC algorithm providing a better performance. In the numerical simulations shown in this thesis both methods were employed.

B.1.2 Reorientational Equation

To solve eq. (B.2) I use a nonlinear Gauss-Seidel relaxation method (113). First of all, I transform eq. (B.2) in a set of FD equations, setting $\theta = \theta_0$ at the cell edges: the found set is nonlinear owing to the presence of the term $\sin[2(\theta-\delta)]$. Such equation system is linearized by a step of the Newton iteration. Guessing an initial solution for θ (similar to the expected solution), I recursively solve the equations via the Gauss-Seidel algorithm, which requires the substitution of the obtained values as soon as they are computed. The iterations are stopped when the difference, defined by a well-suited functional, between new and old solutions is below an established threshold, which depends on the desired accuracy.

Let me focus on the boundary conditions. In the numerical code only finite boundary conditions can be implemented: such hypothesys agrees with actual situation along the x direction, whereas along t actual geometry has an infinite thickness. In order to get a good approximation of infinite case, I enlarge the grid across t until I obtain stabilization of θ profile in the zone where the beam is placed. Furthermore, accuracy of the numerical code was tested by comparing the numerical findings with those derived by a perturbative approach coupled with the Green function technique. All details are reported in section 3.2.4.2.

Appendix C

Analysis of the Index Perturbation Profile

C.1 FWHM Computation for the Nonlinear Index Perturbation

Assuming that the nonlinear index perturbation Δn is bell-shaped and symmetric with respect to beam axis (for homogeneous nonlinear media excited by a Gaussian beam, this hypothesis is certainly verified.) I can take the $FWHM_{x_i}^{\Delta n}$ proportional to $\langle x_i^2 \rangle_{\Delta n} = \iint x_i^2 \Delta n dx dt / \iint \Delta n dx dt$ ($i = 1, 2; x_1 = x, x_2 = t$), with a coefficient dependent on the specific Δn shape. Being $\Delta n = \sum_{m=1}^{\infty} (\Delta n_m / m!) \Delta\rho^m$, I get

$$\begin{aligned} \langle x_i^2 \rangle_{\Delta n} &= \frac{\left(\iint \sum_{m=1}^{\infty} (\Delta n_m/m!) \Delta\rho^m\right) x_i^2 dx dt}{\iint \Delta n dx dt} \\ &= \frac{\sum_{m=1}^{\infty} (\Delta n_m/m!) \langle x_i^2 \rangle_{\Delta\rho^m} I_{\Delta\rho^m}}{\iint \Delta n dx dt} \end{aligned} \tag{C.1}$$

where $I_{\Delta\rho^m} = \iint \Delta\rho^m dx dt$. Equation (C.1) tells me that the width of Δn is an average of all the $\Delta\rho^m$ widths, with weight $\frac{(\Delta n_m/m!) I_{\Delta\rho^m}}{\sum_{l=1}^{\infty} (\Delta n_l/l!) I_{\Delta\rho^l}}$. Moreover, if $\langle x_i^2 \rangle_{\Delta\rho^m}$ does not change with m, I can easily derive $\langle x_i^2 \rangle_{\Delta n} = \langle x_i^2 \rangle_{\Delta\rho}$.
Keeping only the first two terms in (C.1) I obtain

$$\langle x_i^2 \rangle_{\Delta n} = \langle x_i^2 \rangle_{\Delta\rho^1} \frac{\Delta n_1 I_{\Delta\rho}}{\Delta n_1 I_{\Delta\rho} + \Delta n_2 I_{\Delta\rho^2}} + \frac{1}{2} \langle x_i^2 \rangle_{\Delta\rho^2} \frac{\Delta n_2 I_{\Delta\rho^2}}{\Delta n_1 I_{\Delta\rho} + \Delta n_2 I_{\Delta\rho^2}} \tag{C.2}$$

Now, let me consider $\Delta n = \Delta n_1 \Delta\rho$, but $\Delta\rho = \sum_{m=0}^{\infty} \Delta\rho_m P^m$ where P is the beam power; that is, I am considering a nonlinear relationship between $\Delta\rho$ and field intensity I. The former results keep their validity if I perform the substitutions $\Delta n \rightarrow \Delta\rho, \Delta\rho^m \rightarrow \Delta\rho_m, (\Delta n_m/m!) \rightarrow P^m$. I obtain

$$\left\langle x_i^2 \right\rangle_{\Delta\rho} = \frac{\sum_{m=1}^{\infty} P^m \left\langle x_i^2 \right\rangle_{\Delta\rho_m} I_{\Delta\rho_m}}{\iint \Delta\rho dx dt} \tag{C.3}$$

Finally, I treat the asymmetric case. The results found above are valid also for $\sigma_{x/t}^{g/s}$, if appropriate symmetric functions are constructed and used instead of Δn (or $\Delta\rho$). For example, if I compute σ_x^g, I have to take into account Δn only for x larger than the x coordinate of the perturbation peak; the function values in the remaining part of x axes are chosen so that the total function is even with respect to its maximum.

C.2 Computation of $V_m^\upsilon(\upsilon)$ in the Gaussian Case

From eq. (3.24) I know that

$$V_m^\upsilon(\upsilon) = \int_{-\infty}^{\infty} f_\upsilon(\eta) e^{-\pi m|\upsilon-\eta|} d\eta \tag{C.4}$$

Assuming a Gaussian shape for the beam along υ, i.e. $f_\upsilon(\upsilon) = e^{-\frac{\upsilon^2}{\omega_t^2}}$, I have

$$V_m^\upsilon(\upsilon) = \int_{-\infty}^{\infty} e^{-\frac{\eta^2}{\omega_t^2}} e^{-\pi m|\upsilon-\eta|} d\eta \tag{C.5}$$

Eq. (C.5) is equivalent to

$$V_m^\upsilon(\upsilon) = \int_{\upsilon}^{\infty} e^{-\frac{\eta^2}{\omega_t^2}} e^{\pi m(\upsilon-\eta)} d\eta + \int_{-\infty}^{\upsilon} e^{-\frac{\eta^2}{\omega_t^2}} e^{-\pi m(\upsilon-\eta)} d\eta \tag{C.6}$$

Completing the squares in the exponents (C.6) provides

$$V_m^\upsilon(\upsilon) = e^{\pi m\upsilon} e^{\left(\frac{\pi m}{2}\right)^2 \omega_t^2} \int_{\upsilon}^{\infty} e^{-\frac{1}{\omega_t^2}\left(\eta+\frac{\pi m}{2}\omega_t^2\right)^2} d\eta + e^{-\pi m\upsilon} e^{\left(\frac{\pi m}{2}\right)^2 \omega_t^2} \int_{-\infty}^{\upsilon} e^{-\frac{1}{\omega_t^2}\left(\eta-\frac{\pi m}{2}\omega_t^2\right)^2} d\eta \tag{C.7}$$

Eq. (C.7) can be expressed as

$$V_m^{\upsilon}(\upsilon) = \frac{\sqrt{\pi}}{2}\omega_t e^{\left(\frac{\pi m}{2}\right)^2 \omega_t^2}\left[e^{\pi m \upsilon}\mathrm{erfc}\left(\frac{\upsilon}{\omega_t} + \frac{m\pi}{2}\omega_t\right) + e^{-\pi m \upsilon}\mathrm{erfc}\left(-\frac{\upsilon}{\omega_t} + \frac{m\pi}{2}\omega_t\right)\right] \tag{C.8}$$

being $\mathrm{erfc}(x) \equiv \frac{2}{\sqrt{\pi}}\int_x^{\infty} e^{-y^2}dy$. Eq. (C.8) is the searched result. Fig. C.1 shows the found profile of $V_m^{\upsilon}(\upsilon)$.

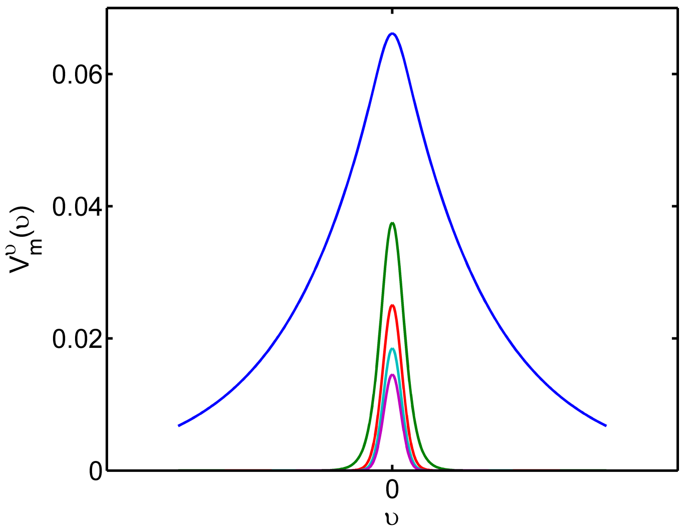

Figure C.1: Plot of $V_m^{\upsilon}(\upsilon)$ versus υ for $m = 1, 10, 20, 30, 40, 50$. Smaller values for m correspond to higher peaks.

C.3 Computation of V_m^{ξ}

From eq. (3.23)

$$V_m^{\xi} = \int_0^1 f_{\xi}(\zeta)\sin(\pi m \zeta)d\zeta \tag{C.9}$$

Eq. (C.9) can be written as

$$V_m^{\xi} = \frac{1}{2i}\int_{-\infty}^{\infty}\left[e^{i\pi m\zeta} - e^{-i\pi m\zeta}\right] f_{\xi}(\zeta)\mathrm{rect}_1(\zeta - 0.5)d\zeta \tag{C.10}$$

where $\mathrm{rect}_b(x)$ is 1 for $x \in (-b/2\ b/2)$, 0 elsewhere. Using the Fourier transform properties I obtain

$$V_m^\xi = -\Im\left\{\mathcal{F}\left[\mathrm{rect}_1(\zeta - 0.5) f_\xi(\zeta)\right]\left(\nu = \frac{m}{2}\right)\right\} \tag{C.11}$$

where operators $\mathcal{F}$ and $\Im$ stand for Fourier transformation and imaginary part, respectively. Convolution theorem provides $\mathcal{F}\left[\mathrm{rect}_1(\xi - 0.5) f_\xi(\xi)\right] = \mathcal{F}\left[\mathrm{rect}_1(\xi - 0.5)\right] * \mathcal{F}\left[f_\xi(\xi)\right]$, being $*$ the convolution operator. Defining $f_\xi(\xi) = g(\xi - \langle\xi\rangle)$ and $\mathcal{F}[g](\nu) = \tilde{g}(\nu)$, knowing that $\mathcal{F}\left[\mathrm{rect}_1(\xi - 0.5)\right](\nu) = e^{-i\pi\nu}\mathrm{Ca}(\pi\nu)$ and $\mathcal{F}\left[f_\xi(\xi)\right](\nu) = e^{-2\pi i\langle\xi\rangle\nu}\tilde{g}(\nu)$, eq. (C.11) becomes

$$V_m^\xi = -\Im\left\{\int_{-\infty}^{\infty} e^{-i\pi\nu}\mathrm{Ca}(\pi\nu) e^{-2\pi i\langle\xi\rangle\left(\frac{m}{2}-\nu\right)}\tilde{g}\left(\frac{m}{2} - \nu\right) d\nu\right\} \tag{C.12}$$

If $\mathrm{Ca}(\pi\nu)$ is very narrow with respect to $\tilde{g}(\nu)$, i.e., the beam is much smaller than the cell width a, if $\langle\xi\rangle$ is not too close to the cell edges, eq. (C.12) yields

$$\begin{aligned} V_m^\xi \cong & -\Im\left\{e^{-i\pi m\langle\xi\rangle}\tilde{g}\left(\frac{m}{2}\right)\int_{-\infty}^{\infty}\mathrm{Ca}(\pi\nu)d\nu\right\} \\ = & \sin\left(\pi m\langle\xi\rangle\right)\tilde{g}\left(\frac{m}{2}\right) \end{aligned} \tag{C.13}$$

For a Gaussian beam along ξ, i.e. $f_\xi(\xi) = e^{-\frac{\xi^2}{\omega_x^2}}$, I can easily derive $\tilde{g}(\nu) = \sqrt{\pi}\omega_x e^{-\pi^2\omega_x^2\nu^2}$. Therefore, eq. (C.13) becomes

$$V_m^\xi(\langle\xi\rangle) \cong \sqrt{\pi}\omega_x \sin\left(\pi m\langle\xi\rangle\right) e^{-\pi^2\omega_x^2\left(\frac{m}{2}\right)^2} \tag{C.14}$$

Eq. (C.14) is the result I looked for.

C.4 Computation of V_m^υ

In the Gaussian case $f_\upsilon(\upsilon) = e^{-\frac{\upsilon^2}{\omega_t^2}}$, recalling eq. (3.24), V_m^υ is written as:

$$V_m^\upsilon = \frac{\int_{-\infty}^{\infty} V_m^\upsilon(\upsilon) e^{-\frac{\upsilon^2}{\omega_t^2}} d\upsilon}{\pi \omega_t^2} = \\ = \frac{1}{2\sqrt{\pi}\omega_t} e^{\left(\frac{\Theta_m \omega_t}{2}\right)^2} \int_{-\infty}^{\infty} \left[\operatorname{erfc}\left(\frac{\upsilon}{\omega_t} + \frac{\Theta_m \omega_t}{2}\right) e^{\Theta_m \upsilon - \frac{\upsilon^2}{\omega_t^2}} + \operatorname{erfc}\left(-\frac{\upsilon}{\omega_t} + \frac{\Theta_m \omega_t}{2}\right) e^{-\Theta_m \upsilon - \frac{\upsilon^2}{\omega_t^2}} \right] d\upsilon \tag{C.15}$$

Substituting $y = \frac{\upsilon}{\omega_t} \pm \frac{\Theta_m \omega_t}{2}$ in the first and second integral, respectively, I get:

$$V_m^\upsilon = \frac{1}{\sqrt{\pi}} e^{\left(\frac{\Theta_m}{\sqrt{2}}\omega_t\right)^2} \int_{-\infty}^{\infty} \operatorname{erfc}(y) e^{-(y-\Theta_m \omega_t)^2} dy \tag{C.16}$$

Defining the new function $F(x) = \int_{-\infty}^{\infty} \operatorname{erfc}(x') e^{-(x'-x)^2} dx'$ I finally have:

$$V_m^\upsilon = \frac{1}{\sqrt{\pi}} e^{\left(\frac{\Theta_m}{\sqrt{2}}\omega_t\right)^2} F(\Theta_m \omega_t) \tag{C.17}$$

The results are shown in fig. C.2.

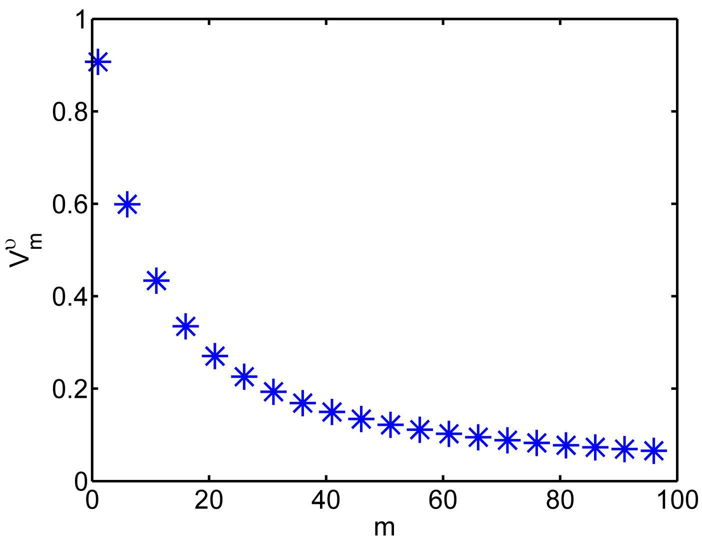

Figure C.2: Plot of V_m^υ versus integer index m.

C.5 Force in the Poisson 2D for Small Displacements

In 2D Poisson and screened Poisson case the force acting on the beam is given by [eq. (3.71)]:

$$W_0(\langle x\rangle) = C\sum_{m=1}^{\infty} V_m^{\xi} V_m^{v}\cos(\pi m\langle\xi\rangle) \tag{C.18}$$

For small displacements, from eq. (3.63):

$$F_X^m(\langle\xi\rangle) \cong c_0^1\left(\langle\xi\rangle - \xi_0\right) \tag{C.19}$$

being

$$c_0^1 = \left.\frac{\partial W_0(\langle\xi\rangle)}{\partial\langle\xi\rangle}\right|_{\langle\xi\rangle=\xi_0} \tag{C.20}$$

The first derivative of W_0 is:

$$\begin{aligned}
\frac{\partial W_0}{\partial\langle\xi\rangle} &= C\sum_{m=1}^{\infty}\frac{\pi m}{\Theta_m}V_m^{v}\frac{\partial\left[V_m^{\langle\xi\rangle}\cos(\pi m\xi)\right]}{\partial\langle\xi\rangle}\\
&= C\sum_{m=1}^{\infty}\frac{\pi m}{\Theta_m}V_m^{v}\left[\frac{\partial V_m^{\langle\xi\rangle}}{\partial\langle\xi\rangle}\cos(\pi m\xi) - \pi m\sin(\pi m\langle\xi\rangle)V_m^{\xi}\right]\\
&= C\sum_{m=1}^{\infty}\frac{\pi m}{\Theta_m}V_m^{v}\cos(\pi m\langle\xi\rangle)\frac{\partial V_m^{\xi}}{\partial\langle\xi\rangle} - \sum_{m=1}^{\infty}\frac{(\pi m)^2}{\Theta_m}V_m^{v}V_m^{\xi}\sin(\pi m\langle\xi\rangle)\\
&= S_1 + S_2
\end{aligned} \tag{C.21}$$

Recalling eq. (3.23), taking $\xi_0 = 0.5$ and guessing $f_\xi(\xi) = e^{-\frac{\xi^2}{w^2}}$, S_1 and S_3 computed in $\langle\xi\rangle = 0.5$ are:

$$S_1|_{\langle\xi\rangle=0.5} = \frac{4C}{w^2}\sum_{m=1}^{\infty}V_{2m}^{v}\int_0^{0.5} t\sin(2\pi mt)e^{-\frac{t^2}{w^2}}dt \tag{C.22}$$

$$S_2|_{\langle\xi\rangle=0.5} = -4C\sum_{m=0}^{\infty}\frac{\pi(2m+1)}{2}V_{2m+1}^{v}\int_0^{0.5}\cos[\pi(2m+1)t]e^{-\frac{t^2}{w^2}}dt \tag{C.23}$$

Finally, substituting eqs. (C.22)-(C.23) into (C.20) I get:

$$c_0^1 = 2C\sum_{m=1}^{\infty}\pi m V_m^{v}(-1)^m\int_0^{0.5}e^{-\frac{t^2}{w^2}}\cos(\pi mt)dt \tag{C.24}$$

Appendix D

List of Publications

D.1 Journal Papers

A. Alberucci, M. Peccianti, G. Assanto, G. Coschignano, A. De Luca, and C. Umeton, **Self-healing generation of spatial solitons in liquid crystal**, Opt. Lett. **30**, 1381-1383 (2005)

A. Pasquazi, A. Alberucci, M. Peccianti, and G. Assanto, **Signal processing by opto-optical interactions between self-localized and free propagating beams in liquid crystals**, Appl. Phys. Lett. **87**, 261104 (2005)

G. Assanto, C. Umeton, M. Peccianti, and A. Alberucci, **Nematicons and their angular steering**, J. Nonl. Opt. Phys. Mat. **15**, 33-42 (2006)

A. Alberucci, M. Peccianti, G. Assanto, A. Dyadyusha, M. Kaczmarek, **Two-color vector solitons in nonlocal media**, Phys. Rev. Lett. **97**, 153903 (2006)

A. Alberucci, M. Peccianti, and G. Assanto, **Nonlinear bouncing of nonlocal spatial solitons at the boundaries**, Opt. Lett. **32**, 2795-2797 (2007)

A. Alberucci and G. Assanto, **Propagation of optical spatial solitons in finite size media: interplay between non locality and boundary conditions**, J. Opt. Soc. Am. B **24**, 2314-2320 (2007)

A. Alberucci and G. Assanto, **Dissipative Self-Confined Optical Beams in Nematic Liquid Crystals**, J. Nonl. Opt. Phys. Mat. **16**, 295-305 (2007)

D.2 Conference Papers

M.Peccianti, C. Conti, G. Assanto, A. Alberucci, C. Umeton, A. de Luca, and G. Coschignano; Walking Nematicons; 7th Mediterranean Workshop and Topical Meeting on Novel Optical Materials and Applications, Cetraro (Italy), May 29 - June 04, 2005

M. Peccianti, G. Assanto, A. Alberucci, C. Conti, G. Coschignano, A. de Luca, C. Umeton; Anisotropic spatial solitons and their routing in nematic liquid crystals; Proc. CLEO EUROPE2005/IQEC 2005, Munich (Germany), June 12-17, 2005, Europhysics Conference Abstracts 14A CD6-1-THU (2005)

G. Assanto, M. Peccianti, C. Conti, A. Alberucci, C. Umeton, A. de Luca, and G. Coschignano; Anisotropic nematicons and their routing in liquid crystals (Invited Paper); SPIE Int. Congress on Optics an Optoelectronics [5947-28], Warsaw (Poland) Aug 28- Sept 2 , 2005

M. Peccianti, A. Alberucci, G. Assanto, A. De Luca, G. Coschignano and C. Umeton; Walking Anisotropic Spatial Solitons and Their Steering in Nematic Liquid Crystals; Dresden (Germany), Sept 6-9 FA1 (2005)

C. Umeton, A.De Luca, G. Coschignano, L. Pezzi, A. Veltri, A. Alberucci, C. Conti, M. Peccianti and G. Assanto; Liquid Crystal Cells for Generation and Propagation of Optical Spatial Solitons; 21st International Liquid Crystal Conf., July 2-7 (2006)

A. Alberucci, M. Peccianti, G. Assanto, A. Dyadyusha, and M. Kaczmarek, Nonlocal bi-color vector solitons in liquid crystals; IQEC 2007, pap. IE7-2-THU

M. Peccianti, A. Alberucci, and G. Assanto; Nonlinear bouncing of nematicons at the boundaries; LEOS Winter Top. 2008 Nonlinear Photonics, Sorrento (Italy), Jan. 14-16, 2008

References

[1] E. Fermi, J. Pasta, and S. Ulam, "Studies of non linear problems," Los Alamos National Laboratory, Technical Report, 1955. 1

[2] E. Segré, *Collected Papers of Enrico Fermi*. Chicago: University of Chicago Press, 1965. 1

[3] E. N. Lorenz, "Deterministic nonperiodic flow," *J. Atmos. Sci.*, vol. 20, pp. 130–141, 1963. 1

[4] C. S. Gardner, J. M. Greene, M. D. Kruskal, and R. M. Miura, "Method for solving the korteweg-devries equation," *Phys. Rev. Lett.*, vol. 19, no. 19, pp. 1095–1097, Nov 1967. 1

[5] S. Trillo and W. E. Torruellas, *Spatial Solitons*. Berlin: Springer-Verlag, 2001. 2, 3

[6] Y. S. Kivshar and G. P. Agrawal, *Optical Solitons*. San Diego, CA: Academic, 2003. 2, 3, 5, 72

[7] J. S. Russell, "Report on waves," in *Report of the fourteenth meeting of the British Association for the Advancement of Science*, York, September 1844 (London 1845), 1844, pp. 311–390. 2

[8] D. J. Korteweg and F. D. Vries, "On the change of form of long waves advancing in a rectangular canal, and on a new type of long stationary waves," *Philosophical Magazine*, vol. 39, pp. 422–443, 1895. 2

[9] N. J. Zabusky and M. D. Kruskal, "Interaction of "solitons" in a collisionless plasma and the recurrence of initial states," *Phys. Rev. Lett.*, vol. 15, no. 6, pp. 240–243, Aug 1965. 2

[10] Y. Nakamura and I. Tsukabayashi, "Observation of modified korteweg-de vries solitons in a multicomponent plasma with negative ions," *Phys. Rev. Lett.*, vol. 52, no. 26, pp. 2356–2359, Jun 1984. 2

[11] L. Khaykovich, F. Schreck, G. Ferrari, T. Bourdel, J. Cubizolles, L. D. Carr, Y. Castin, and C. Salomon, "Formation of a Matter-Wave Bright Soliton," *Science*, vol. 296, no. 5571, pp. 1290–1293, 2002. [Online]. Available: http://www.sciencemag.org/cgi/content/abstract/296/5571/1290 2

[12] A. J. Heeger, S. Kivelson, J. R. Schrieffer, and W. P. Su, "Solitons in conducting polymers," *Rev. Mod. Phys.*, vol. 60, no. 3, pp. 781–850, Jul 1988. 2

[13] V. Belinski and E. Verdaguer, *Gravitational solitons.* Cambridge: Cambridge University Press, 2001. 2

[14] D. S. Ricketts, X. Li, and D. Ham, "A self-sustained electrical soliton oscillator," *IEEE Trans. Microwave Theor. Tech.*, vol. 54, pp. 373–382, 2006. 2

[15] R. W. Boyd, *Nonlinear Optics.* Boston: Academic Press, 1992. 2, 4, 13

[16] T. H. Maiman, "Stimulated optical radiation in ruby," *Nature*, vol. 187, pp. 493–494, 1960. 2

[17] P. A. Franken, A. E. Hill, C. W. Peters, and G. Weinreich, "Generation of optical harmonics," *Phys. Rev. Lett.*, vol. 7, no. 4, pp. 118–119, Aug 1961. 2

[18] R. Y. Chiao, E. Garmire, and C. H. Townes, "Self-trapping of optical beams," *Phys. Rev. Lett.*, vol. 13, no. 15, pp. 479–482, Oct 1964. 2, 13

[19] P. L. Kelley, "Self-focusing of optical beams," *Phys. Rev. Lett.*, vol. 15, no. 26, pp. 1005–1008, Dec 1965. 2

[20] A. Yariv, Ed., *Optical Electronics in Modern Communications.* Oxford: Oxford University Press, 1997. 2

[21] Y. S. Kivshar and B. Luther-Davies, "Dark optical solitons: physics and applications," *Physics Reports*, vol. 298, pp. 81–197, 1998. 3

[22] H. A. Haus and W. S. Wong, "Solitons in optical communications," *Rev. Mod. Phys.*, vol. 68, no. 2, pp. 423–444, Apr 1996. 3

[23] G. I. Stegeman and M. Segev, "Optical Spatial Solitons and Their Interactions: Universality and Diversity," *Science*, vol. 286, no. 5444, pp. 1518–1523, 1999. [Online]. Available: http://www.sciencemag.org/cgi/content/abstract/286/5444/1518 3

[24] G. Stegeman, D. Christodoulides, and M. Segev, "Optical spatial solitons: historical perspectives," *Selected Topics in Quantum Electronics, IEEE Journal of*, vol. 6, no. 6, pp. 1419–1427, Nov/Dec 2000. 3

[25] H. L. Pecseli and J. J. Rasmussen, "Nonlinear electron waves in strongly magnetized plasma," *Plasma Phys.*, vol. 22, p. 421, 1980. 4

[26] A. Parola, L. Salasnich, and L. Reatto, "Structure and stability of bosonic clouds: Alkali-metal atoms with negative scattering length," *Phys. Rev. A*, vol. 57, no. 5, pp. R3180–R3183, May 1998. 4

[27] P. Pedri and L. Santos, "Two-dimensional bright solitons in dipolar bose-einstein condensates," *Phys. Rev. Lett.*, vol. 95, p. 200404, 2005. 4

[28] P. Van and T. Fulop, "Weakly nonlocal fluid mechanics - the schrodinger equation," *LONDON A*, vol. 462, p. 541, 2006. [Online]. Available: http://www.citebase.org/abstract?id=oai:arXiv.org:quant-ph/0304062 4

[29] C. Conti and G. Assanto, *Encyclopedia of Modern Optics*. Oxford: Elsevier, 2004, vol. 5, ch. Nonlinear optics applications: Bright spatial solitons, pp. 43–55. 4

[30] C. Conti, M. Peccianti, and G. Assanto, "Route to nonlocality and observation of accessible solitons," *Phys. Rev. Lett.*, vol. 91, p. 073901, 2003. 4, 6, 14, 37, 47

[31] A. W. Snyder and D. J. Mitchell, "Accessible solitons," *Science*, vol. 276, p. 1538, 1997. 4, 5, 6, 27, 28, 29, 34, 58, 89, 91, 98

[32] W. Krolikowski and O. Bang, "Solitons in nonlocal nonlinear media: exact solutions," *Phys. Rev. E*, vol. 63, p. 016610, 2000. 4, 5, 7, 37

[33] N. I. Nikolov, D. Neshev, W. Królikowski, O. Bang, J. J. Rasmussen, and P. L. Christiansen, "Attraction of nonlocal dark optical solitons," *Opt. Lett.*, vol. 29, no. 3, pp. 286–288, 2004. [Online]. Available: http://ol.osa.org/abstract.cfm?URI=ol-29-3-286 4

[34] Z. Xu, Y. V. Kartashov, and L. Torner, "Stabilization of vector soliton complexes in nonlocal nonlinear media," *Phys. Rev. E*, vol. 49, p. 055601, 2006. 4, 32, 47

[35] V. M. Pérez-García and V. Vekslerchik, "Soliton molecules in trapped vector nonlinear schrödinger systems," *Phys. Rev. E*, vol. 67, no. 6, p. 061804, Jun 2003. 4, 72

[36] Y. V. Kartashov, L. Torner, V. A. Vysloukh, and D. Mihalache, "Multipole vector solitons in nonlocal nonlinear media," *Opt. Lett.*, vol. 31, no. 10, pp. 1483–1485, 2006. [Online]. Available: http://ol.osa.org/abstract.cfm?URI=ol-31-10-1483 4

[37] A. S. Desyatnikov, D. Neshev, E. A. Ostrovskaya, Y. S. Kivshar, G. McCarthy, W. Krolikowski, and B. Luther-Davies, "Multipole composite spatial solitons: theory and experiment," *J. Opt. Soc. Am. B*, vol. 19, no. 3, pp. 586–595, 2002. [Online]. Available: http://josab.osa.org/abstract.cfm?URI=josab-19-3-586 4

[38] A. G. Litvak, "Self-focusing of powerful light beams by thermal effects," *JETP Letters-USSR*, vol. 4, p. 230, 1966. 4

[39] C. Rotschild, O. Cohen, O. Manela, M. Segev, and T. Carmon, "Solitons in nonlinear media with an infinite range of nonlocality: first observation of coherent elliptic solitons and of vortex-ring solitons," *Phys. Rev. Lett.*, vol. 95, p. 213904, 2005. 4, 5, 6, 37

[40] A. Dreischuh, D. N. Neshev, D. E. Petersen, O. Bang, and W. Krolikowski, "Observation of attraction between dark solitons," *Phys. Rev. Lett.*, vol. 96, p. 043901, 2006. 4

[41] M. Segev, B. Crosignani, A. Yariv, and B. Fischer, "Spatial solitons in photorefractive media," *Phys. Rev. Lett.*, vol. 68, p. 923, 1992. 4

[42] W. Krolikowski, B. Luther-Davies, and C. Denz, "Photorefractive solitons," *J. Quantum Electron.*, vol. 39, p. 3, 2003. 4, 37

[43] C. Conti, G. Ruocco, and S. Trillo, "Optical spatial solitons in soft matter," *Phys. Rev. Lett.*, vol. 95, p. 183902, 2005. 4

[44] E. A. Ultanir, G. Stegeman, C. H. Lange, and F. Lederer, "Coherent interactions of dissipative spatial solitons," *Opt. Lett.*, vol. 29, no. 3, pp. 283–285, 2004. [Online]. Available: http://ol.osa.org/abstract.cfm?URI=ol-29-3-283 4

[45] D. Suter and T. Blasberg, "Stabilization of transverse solitary waves by a nonlocal response of the nonlinear medium," *Phys. Rev. A*, vol. 48, no. 6, pp. 4583–4587, Dec 1993. 4

[46] M. Peccianti, A. D. Rossi, G. Assanto, A. D. Luca, C. Umeton, and I. C. Khoo, "Electrically assisted self-confinement and waveguiding in planar nematic liquid crystal cells," *Applied Physics Letters*, vol. 77, no. 1, pp. 7–9, 2000. [Online]. Available: http://link.aip.org/link/?APL/77/7/1 4, 13

[47] M. Peccianti, C. Conti, G. Assanto, A. D. Luca, and C. Umeton, "Routing of anisotropic spatial solitons and modulational instability in nematic liquid crystals," *Nature*, vol. 432, p. 733, 2004. 4, 6, 14, 22, 25, 89, 107

[48] W. E. Torruellas, Z. Wang, D. J. Hagan, E. W. VanStryland, G. I. Stegeman, L. Torner, and C. R. Menyuk, "Observation of two-dimensional spatial solitary waves in a quadratic medium," *Phys. Rev. Lett.*, vol. 74, no. 25, pp. 5036–5039, Jun 1995. 4, 72

[49] J. J. Sakurai, *Modern Quantum Mechanics.* Reading, MA: Addison-Wesley, 1994. 4, 6, 27, 49, 58, 77

[50] S. Abe and A. Ogura, "Solitary waves and their critical behavior in a nonlinear nonlocal medium with power-law response," *Phys. Rev. E*, vol. 57, p. 6066, 1998. 5

[51] C. Conti, M. Peccianti, and G. Assanto, "Observation of optical spatial solitons in a highly nonlocal medium," *Phys. Rev. Lett.*, vol. 92, p. 113902, 2004. 5, 6, 14, 27, 28, 29, 34, 63, 91

[52] ——, "Spatial solitons and modulational instability in the presence of large birefringence: the case of highly non-local liquid crystals," *Phys. Rev. E*, vol. 72, p. 066614, 2005. 5, 25, 28, 34, 107

[53] Q. Guo, B. Luo, F. Yi, S. Chi, and Y. Xie, "Large phase shift of nonlocal optical spatial solitons," *Phys. Rev. E*, vol. 69, no. 1, p. 016602, Jan 2004. 5, 6

[54] S. Ouyang, Q. Guo, and W. Hu, "Perturbative analysis of generally nonlocal spatial optical solitons," *Physical Review E (Statistical, Nonlinear, and Soft Matter Physics)*, vol. 74, no. 3, p. 036622, 2006. [Online]. Available: http://link.aps.org/abstract/PRE/v74/e036622 5

[55] N. I. Nikolov, D. Neshev, O. Bang, and W. Z. Królikowski, "Quadratic solitons as nonlocal solitons," *Phys. Rev. E*, vol. 68, no. 3, p. 036614, Sep 2003. 5

[56] D. Buccoliero, A. S. Desyatnikov, W. Krolikowski, and Y. S. Kivshar, "Laguerre and hermite soliton clusters in nonlocal nonlinear media," *Physical Review Letters*, vol. 98, no. 5, p. 053901, 2007. [Online]. Available: http://link.aps.org/abstract/PRL/v98/e053901 6

[57] C. Rotschild, M. Segev, Z. Xu, Y. V. Kartashov, L. Torner, and O. Cohen, "Two-dimensional multipole solitons in nonlocal nonlinear media," *Opt. Lett.*, vol. 31, no. 22, pp. 3312–3314, 2006. [Online]. Available: http://ol.osa.org/abstract.cfm?URI=ol-31-22-3312 6

[58] P. G. D. Gennes and J. Prost, *The Physics of Liquid Crystals*. New York: Oxford Science, 1993. 7, 9, 10, 11, 12, 15, 19, 73, 88, 104

[59] F. Simoni, *Nonlinear Optical Properties of Liquid Crystals*. Singapore: World Scientific, 1997. 10, 12

[60] I. C. Khoo, *Liquid Crystals: Physical Properties and Nonlinear Optical Phenomena*. New York: Wiley, 1995. 10, 11, 13, 73, 88, 104

[61] M. Born and E. Wolf, *Principles of Optics*. New York: Pergamon Press, 1975. 10

[62] B. Zeldovich, N. Pilipetskii, A. Sukhov, and N. Tabiryan, "Giant optical nonlinearity in the mesophase of a nematic liquid crystals (ncl)," *JETP Letters*, vol. 31, pp. 263–269, 1980. 13

[63] N. Tabiryan and B. Zeldovich, "The orientational optical nonlinearity of liquid-crystals," *Molecular Crystals and Liquid Crystals*, vol. 62, pp. 237–250, 1980. 13

[64] M. Assanto, G.; Peccianti, "Spatial solitons in nematic liquid crystals," *Quantum Electronics, IEEE Journal of*, vol. 39, no. 1, pp. 13–21, Jan 2003. 13

[65] E. Braun, L. P. Faucheux, and A. Libchaber, "Strong self-focusing in nematic liquid crystals," *Phys. Rev. A*, vol. 48, no. 1, pp. 611–622, Jul 1993. 13

[66] M. Warenghem, J. F. Henninot, and G. Abbate, "Bulk optical fredericksz effect: Non linear optics of nematics liquid crystals in capillaries," *Molecular Crystals and Liquid Crystals*, vol. 320, pp. 207–230, 1998. 13

[67] I. Janossy and B. Lloyd, A.D. nd Wherrett, "Anomalous optical freedericksz transition in an absorbing liquid crystal," *Molecular Crystals and Liquid Crystals*, vol. 179, pp. 1–12, 1990. 13

[68] X. Hutsebaut, C. Cambournac, M. Haelterman, A. Adamski, and K. Neyts, "Single-component higher-order mode solitons in liquid crystals," *Optics Communications*, vol. 233, pp. 211–217, 2004. 13

[69] F. Derrien, J. F. Henninot, M. Warenghem, and G. Abbate, "A thermal (2d+1) spatial optical soliton in a dye doped liquid crystal," *J. Opt. A: Pure Appl. Opt.*, vol. 2, p. 332, 2000. 13, 90

[70] J. Henninot, M. Debailleul, and M. Warenghem, "Tunable non-locality of thermal non-linearity in dye doped nematic liquid crystal," *Molecular Crystals and Liquid Crystals*, vol. 375, pp. 631–640, 2002. 13

[71] M. Karpierz, M. Sierakowski, M. Swillo, and T. Wolinski, "Self focusing in liquid crystalline waveguides," *Molecular Crystals and Liquid Crystals*, vol. 320, pp. 157–163, 1998. 13

[72] M. A. Karpierz, "Solitary waves in liquid crystalline waveguides," *Phys. Rev. E*, vol. 66, no. 3, p. 036603, Sep 2002. 13

[73] M. Peccianti, C. Conti, and G. Assanto, "The interplay between non locality and nonlinearity in nematic liquid crystals," *Opt. Lett.*, vol. 30, p. 415, 2005. 14

[74] M. Peccianti, K. Brzadkiewicz, and G. Assanto, "Nonlocal spatial soliton interactions in nematic liquid crystals," *Opt. Lett.*, vol. 27, p. 1460, 2002. 14

[75] M. Peccianti and G. Assanto, "Incoherent spatial solitary waves in nematic liquid crystals," *Opt. Lett.*, vol. 26, p. 1791, 2001. 14

[76] M. Peccianti, C. Conti, G. Assanto, A. D. Luca, and C. Umeton, "All optical switching and logic gating with spatial solitons in liquid crystals," *Appl. Phys. Lett.*, vol. 81, p. 3335, 2002. 14

[77] W. Hu, T. Zhang, Q. Guo, L. Xuan, and S. Lan, "Nonlocality-controlled interaction of spatial solitons in nematic liquid crystals," *Applied Physics Letters*, vol. 89, no. 7, p. 071111, 2006. [Online]. Available: http://link.aip.org/link/?APL/89/071111/1 14

[78] D. Berreman, "Optics in stratified and anisotropic media - 4x4-matrix formulation," *Journal of the Optical Society of America*, vol. 62, p. 502, 1972. 17

[79] A. Alberucci, "Elaborazione ottica di segnali con dispositivi in cristalli liquidi nematici," Master's thesis, Università degli Studi Roma Tre, 2004. 18, 22, 24, 28

[80] A. Alberucci, M. Peccianti, G. Assanto, G. Coschignano, A. D. Luca, and C. Umeton, "Self-healing generation of spatial solitons in liquid crystals," *Opt. Lett.*, vol. 30, no. 11, pp. 1381–1383, 2005. [Online]. Available: http://ol.osa.org/abstract.cfm?URI=ol-30-11-1381 18

[81] M. Peccianti, A. Fratalocchi, and G. Assanto, "Transverse dynamics of nematicons," *Opt. Express*, vol. 12, p. 6524, 2004. 24, 89

[82] M. J. Weber, Ed., *CRC Handbook of Laser Science and Technology, Optical Materials.* New York: CRC, 1995. 28

[83] Z. Xu, Y. V. Kartashov, and L. Torner, "Soliton mobility in nonlocal optical lattices," *Physical Review Letters*, vol. 95, no. 11, p. 113901, 2005. [Online]. Available: http://link.aps.org/abstract/PRL/v95/e113901 32, 47

[84] G. B. Arfken and H. J. Weber, *Mathematical Methods for Physicists*. New York: Academic, 2001. 39

[85] B. Alfassi, C. Rotschild, O. Manela, M. Segev, and D. N. Christodoulides, "Boundary force effects exerted on solitons in highly nonlocal nonlinear media," *Opt. Lett.*, vol. 32, p. 154, 2006. 39, 63

[86] I. Kaminer, C. Rotschild, O. Manela, and M. Segev, "Periodic solitons in nonlocal nonlinear media," *Opt. Lett.*, vol. 32, no. 21, pp. 3209–3211, 2007. [Online]. Available: http://ol.osa.org/abstract.cfm?URI=ol-32-21-3209 39

[87] C. Rothschild, B. Alfassi, O. Cohen, and M. Segev, "Long-range interactions between optical solitons," *Nature Phys.*, vol. 2, p. 769, 2006. 41

[88] S. V. Manakov, "On the theory of two-dimensional stationary self-focusing of electromagnetic waves," *Soviet Phys. JETP*, vol. 38, pp. 248–253, 1974. 72

[89] J. U. Kang, G. I. Stegeman, J. S. Aitchison, and N. Akhmediev, "Observation of manakov spatial solitons in algaas planar waveguides," *Phys. Rev. Lett.*, vol. 76, no. 20, pp. 3699–3702, May 1996. 72

[90] R. D. L. Fuente and A. Barthelemy, "Spatial solitons pairing by cross phase modulation," *Opt. Commun.*, vol. 88, p. 419, 1992. 72

[91] M. Shalaby and A. J. Barthelemy, "Observation of the self-guided propagation of a dark and bright spatial soliton pair in a focusing nonlinear medium," *IEEE J. Quantum Electron.*, vol. 28, p. 2736, 1992. 72

[92] W. E. Torruellas, G. Assanto, B. L. Lawrence, R. A. Fuerst, and G. I. Stegeman, "All-optical switching by spatial walkoff compensation and solitary-wave locking," *Applied Physics Letters*, vol. 68, no. 11, pp. 1449–1451, 1996. [Online]. Available: http://link.aip.org/link/?APL/68/1449/1 72

[93] G. Assanto and G. Stegeman, "Simple physics of quadratic spatial solitons," *Opt. Express*, vol. 10, no. 9, pp. 388–396, 2002. [Online]. Available: http://www.opticsexpress.org/abstract.cfm?URI=oe-10-9-388 72

[94] M. Mitchell, M. Segev, and D. N. Christodoulides, "Observation of multihump multimode solitons," *Phys. Rev. Lett.*, vol. 80, no. 21, pp. 4657–4660, May 1998. 72

[95] D. N. Christodoulides, S. R. Singh, M. I. Carvalho, and M. Segev, "Incoherently coupled soliton pairs in biased photorefractive crystals," *Applied Physics Letters*, vol. 68, no. 13, pp. 1763–1765, 1996. [Online]. Available: http://link.aip.org/link/?APL/68/1763/1 72

[96] W. Krolikowski, E. A. Ostrovskaya, C. Weilnau, M. Geisser, G. McCarthy, Y. S. Kivshar, C. Denz, and B. Luther-Davies, "Observation of dipole-mode vector solitons," *Phys. Rev. Lett.*, vol. 85, p. 1424, 2000. 72

[97] T. Carmon, C. Anastassiou, S. Lan, D. Kip, Z. H. Musslimani, M. Segev, and D. Christodoulides, "Observation of two-dimensional multimode solitons," *Opt. Lett.*, vol. 25, p. 1113, 2000. 72

[98] A. Alberucci, M. Peccianti, G. Assanto, A. Dyadyusha, and M. Kaczmarek, "Two-color vector solitons in nonlocal media," *Phys. Rev. Lett.*, vol. 97, p. 153903, 2006. 72

[99] N. N. Akhmediev and V. V. Afanasjev, "Novel arbitrary-amplitude soliton solutions of the cubic-quintic complex ginzburg-landau equation," *Phys. Rev. Lett.*, vol. 75, p. 2320, 1995. 88

[100] N. N. Akhmediev, V. V. Afanasjev, and J. M. Soto-Crespo, "Singularities, special soliton solutions of the cubic-quintic ginzburg-landau equation," *Phys. Rev. E*, vol. 53, pp. 1190–1198, 1996. 88

[101] A. M. Dunlop, E. M. Wright, and W. J. Firth, "Spatial soliton laser," *Opt. Commun.*, vol. 147, p. 393, 1998. 88

[102] L. M. Blinov, G. Cipparrone, P. Pagliusi, V. V. Lazarev, and S. P. Palto, "Mirrorless lasing from nematic liquid crystals in the plane waveguide geometry without refractive index or gain modulation," *Appl. Phys. Lett.*, vol. 89, p. 031114, 2006. 89, 97

[103] L. M. Blinov, G. Cipparrone, A. Mazzulla, P. Pagliusi, V. V. Lazarev, and S. P. Palto, "Simple voltage tunable liquid crystal laser," *Appl. Phys. Lett.*, vol. 90, p. 131103, 2007. 89, 97

[104] S. Ferjani, V. Barna, A. D. Luca, C. Versace, N. Scaramuzza, R. Bartolino, and G. Strangi, "Thermal behavior of random lasing in dye-doped nematic liquid crystals," *Appl. Phys. Lett.*, vol. 89, p. 121109, 2006. 89, 97

[105] G. Strangi, V. Barna, R. Caputo, A. D. Luca, C. Versace, N. Scaramazza, C. Umeton, and R. Bartolino, "Color-tunable organic microcavity laser array using distributed feedback," *Phys. Rev. Lett.*, vol. 94, p. 063903, 2005. 89

[106] M. F. Moreira, I. C. S. Carvalho, W. Cao, C. Bailey, B. Taheri, and P. Palffy-Muhoray, "Cholesteric liquid-crystals laser as an optic fiber-based temperature sensor," *App. Phys. Lett.*, vol. 85, p. 2691, 2004. 89

[107] V. Barna, S. Ferjani, A. D. Luca, R. Caputo, N. Scaramuzza, C. Versace, and G. Strangi, "Band edge and defect modes lasing due to confinement of helixed liquid crystals in cylindrical microcavities," *App. Phys. Lett.*, vol. 87, p. 221108, 2005. 89

[108] L. M. Blinov, G. Cipparrone, A. Mazzulla, P. Pagliusi, and V. V. Lazarev, "Lasing in cholesteric liquid crystal cells: competition of bragg and leaky modes," *J. Appl. Phys.*, vol. 101, p. 053104, 2007. 89

[109] W. Cao, A. Munoz, P. Palffy-Muhoray, and B. Taheri, "Lasing in a three-dimensional photonic crystal of the liquid crystal blue phase ii," *Nat. Mater.*, vol. 1, p. 11, 2002. 89

[110] S. V. Serak, N. V. Tabiryan, M. Peccianti, and G. Assanto, "Spatial soliton all-optical logic gates," *IEEE Photon. Techn. Lett.*, vol. 18, p. 1287, 2006. 90

[111] E. Rosencher and B. Vinter, *Optoelectronics*. New York: Cambridge University Press, 2002. 92, 95

[112] D. J. Mitchell and A. W. Snyder, "Soliton dynamics in a nonlocal medium," *J. Opt. Soc. Am. B*, vol. 16, p. 236, 1999. 98

[113] W. H. Press, B. P. Flannery, S. A. Teukolsky, and W. T. Vetterling, *Numerical Recipes in C, the art of scientific computing*. Cambridge: Cambridge University Press, 1992. 109, 110

[114] F. Vassallo, C.; Collino, "Highly efficient absorbing boundary conditions for the beam propagation method," *Lightwave Technology, Journal of*, vol. 14, no. 6, pp. 1570–1577, 1996. 110

[115] G. R. Hadley, "Transparent boundary condition for beam propagation," *Opt. Lett.*, vol. 16, no. 9, p. 624, 1991. [Online]. Available: http://ol.osa.org/abstract.cfm?URI=ol-16-9-624 110